N° d'ordre NNT : 2026ISAL0011

THESE de DOCTORAT DE L'INSA LYON,
membre de l'Université de Lyon

Ecole Doctorale N° 512
InfoMaths

Spécialité/ discipline de doctorat: Informatique

Soutenue publiquement le 25/02/2026, par :

Diego Antonio MALDONADO MUÑOZ

Estimation, Scalability, Robustness, and Coordination Methods for Direct-to-Satellite IoT

Devant le jury composé de :

BEYLOT	André-Luc	Prof.	ENSEEIHT	Président
CAILLOUET	Christelle	Prof.	Université Côte d'Azur	Rapporteure
GUTIÉRREZ GAITÁN	Miguel	Prof.	UC Chile	Rapporteur
KARABULUT KURT	Güneş	Prof.	Polytechnique Montréal	Rapporteure
RIVANO	Hervé	Prof.	INSA Lyon, Inria	Directeur de thèse
FRAIRE	Juan A.	CR HDR	INSA Lyon, Inria	Co-directeur de thèse

Thèse accessible à l'adresse : https://theses.insa-lyon.fr/publication/2026ISAL0011/these.pdf © [D. Maldonado Muñoz], [2026], INSA Lyon, tous droits réservés

Département FEDORA – INSA Lyon - Ecoles Doctorales

SIGLE	ECOLE DOCTORALE	NOM ET COORDONNEES DU RESPONSABLE
ED 206 CHIMIE	**CHIMIE DE LYON** https://www.edchimie-lyon.fr Sec. : Renée EL MELHEM Bât. Blaise PASCAL 7, Avenue Jean Capelle 69621 Villeurbanne CEDEX secretariat@edchimie-lyon.fr	**M. Stéphane DANIELE** C2P2-CPE LYON-UMR 5265 Bâtiment F308, BP 2077 43 Boulevard du 11 novembre 1918 69616 Villeurbanne CEDEX directeur@edchimie-lyon.fr
ED 341 E2M2	**ÉVOLUTION, ÉCOSYSTÈME, MICROBIOLOGIE, MODÉLISATION** http://e2m2.universite-lyon.fr Sec. : Bénédicte LANZA Bâtiment Atrium, 43, Boulevard du 11 Novembre 1918 69622 Villeurbanne CEDEX Tél : 04.72.44.83.62 secretariat.e2m2@univ-lyon1.fr	**Mme Sandrine CHARLES** Université Claude Bernard Lyon 1 UFR Biosciences, Bâtiment Mendel 43, boulevard du 11 Novembre 1918 69622 Villeurbanne CEDEX e2m2.codir@listes.univ-lyon1.fr
ED 205 EDISS	**INTERDISCIPLINAIRE SCIENCES-SANTÉ** http://ediss.universite-lyon.fr Sec. : Bénédicte LANZA Bâtiment Atrium, 43, Boulevard du 11 Novembre 1918 69622 Villeurbanne CEDEX Tél : 04.72.44.83.62 secretariat.ediss@univ-lyon1.fr	**M. Jérôme LAMARTINE** Université Claude Bernard Lyon 1 Equipe Intégrité Fonctionnelle du Tissu Cutané LBTI - UMR5305 CNRS IBCP - 7 passage du Vercors, 69367 Lyon CEDEX 07 Tel : 04.72.72.26.66 jerome.lamartine@univ-lyon1.fr
ED 34 EDML	**MATÉRIAUX DE LYON** http://ed34.universite-lyon.fr Sec. : Yann DE ORDENANA Tél : 04.72.18.62.44 yann.de-ordenana@ec-lyon.fr	**M. Stéphane BENAYOUN** Ecole Centrale de Lyon Laboratoire LTDS 36 avenue Guy de Collongue 69134 Ecully CEDEX Tél : 04.72.18.64.37 stephane.benayoun@ec-lyon.fr
ED 160 EEA	**ÉLECTRONIQUE, ÉLECTROTECHNIQUE, AUTOMATIQUE** https://edeea.universite-lyon.fr Sec. : Philomène TRECOURT Bâtiment Charlotte PERRIAND 69621 Villeurbanne CEDEX Tél : 04.72.43.71.70 secretariat.edeea@insa-lyon.fr	**M. Philippe DELACHARTRE** INSA LYON Laboratoire CREATIS Bâtiment Blaise Pascal, 7 avenue Jean Capelle 69621 Villeurbanne CEDEX Tél : 04.72.43.88.63 philippe.delachartre@insa-lyon.fr
ED 512 INFOMATHS	**INFORMATIQUE ET MATHÉMATIQUES** http://edinfomaths.universite-lyon.fr Sec. : Renée EL MELHEM Bât. Blaise PASCAL 7, Avenue Jean Capelle 69621 Villeurbanne CEDEX infomaths@univ-lyon1.fr	**M. Dragos IFTIMIE** Université Claude Bernard Lyon 1 Bâtiment Braconnier 21 Avenue Claude BERNARD 69 622 Villeurbanne CEDEX Tél : 04.72.44.79.58 direction.infomaths@listes.univ-lyon1.fr
ED 162 MEGA	**MÉCANIQUE, ÉNERGÉTIQUE, GÉNIE CIVIL, ACOUSTIQUE** http://edmega.universite-lyon.fr Sec. : Philomène TRECOURT Bâtiment Charlotte PERRIAND 69621 Villeurbanne CEDEX Tél : 04.72.43.71.70 mega@insa-lyon.fr	**M. Etienne PARIZET** INSA Lyon Laboratoire LVA Bâtiment St. Exupéry 25 bis av. Jean Capelle 69621 Villeurbanne CEDEX etienne.parizet@insa-lyon.fr
ED 483 ScSo	**ScSo**[1] https://edsciencessociales.universite-lyon.fr Sec. : Mélina FAVETON Tél : 04.78.69.72.76 Université Lyon 2 Campus Berges du Rhône, Bureau BEL 309 18, Quai Claude BERNARD 69365 LYON CEDEX 07 melina.faveton@univ-lyon2.fr	**M. Bruno MILLY** Univ. Lyon 2 Campus Berges du Rhône 18, quai Claude Bernard 69365 LYON CEDEX 07 Bureau BEL 319 bruno.milly@univ-lyon2.fr

[1] ScSo : Histoire, Géographie, Aménagement, Urbanisme, Archéologie, Science politique, Sociologie, Anthropologie

Thèse accessible à l'adresse : https://theses.insa-lyon.fr/publication/2026ISAL0011/these.pdf © [D. Maldonado Muñoz], [2026], INSA Lyon, tous droits réservés

Abstract

Direct-to-Satellite Internet of Things (DtS-IoT) has emerged as a promising paradigm for connecting massive numbers of low-power terrestrial devices directly to Low Earth Orbit (LEO) satellites. While recent advances, such as Long Range - Frequency Hopping Spread Spectrum (LR-FHSS) modulation, have improved the link budget and spectral efficiency compared to the classic LoRa modulation, the fundamental challenges of network size estimation, uplink scalability, and robustness under congestion remain largely unresolved.

This thesis advances the reliability and efficiency of DtS-IoT systems by addressing these three foundational challenges. First, we introduce new network-size estimation mechanisms for LoRa-based DtS-IoT, including the enhanced LoRa-Optimistic Collision Information (L-OCI) and constellation-aware OCI (CL-OCI) models. These estimators operate under highly collision-prone conditions and provide accurate a priori load information for MAC-level adaptation. Second, we propose a unified framework to improve LR-FHSS scalability, combining novel insights into frequency-hopping sequence (FHS) design with demodulator allocation strategies such as *Early-Drop* and *Early-Decode*. Our results show significant improvements in extractable data volume under high device densities and limited gateway resources. Third, we design an enhanced LR-FHSS receiver that enables robust headerless frame decoding under high Doppler shifts and rates, as well as high congestion. By incorporating Doppler-aware greedy reconstruction and an improved fragment alignment logic, the receiver recovers frames that would otherwise be lost due to header corruption, increasing overall decoding success without additional energy expenditure at the device side. Fourth, we address the choice between LoRa and LR-FHSS for device-to-satellite communications by proposing distributed access methods that leverage lightweight satellite orbit determination techniques and periodic beacons. We demonstrate that joint LoRa/LR-FHSS access methods can improve energy efficiency while maintaining the same performance as an LR-FHSS-only approach.

Across all contributions, we combine analytical models with large-scale simulations using extended FLoRaSat and a dedicated FHS simulator. The resulting methodologies and architectures provide practical pathways to scalable, reliable, and energy-efficient DtS-IoT deployments.

Thèse accessible à l'adresse : https://theses.insa-lyon.fr/publication/2026ISAL0011/these.pdf © [D. Maldonado Muñoz], [2026], INSA Lyon, tous droits réservés

Thèse accessible à l'adresse : https://theses.insa-lyon.fr/publication/2026ISAL0011/these.pdf © [D. Maldonado Muñoz], [2026], INSA Lyon, tous droits réservés

Résumé

L'Internet des objets direct vers satellite (Direct-to-Satellite Internet of Things, DtS-IoT) est apparu comme un paradigme prometteur pour connecter directement un grand nombre d'appareils terrestres à faible consommation d'énergie à des satellites en orbite terrestre basse (Low Earth Orbit, LEO). Si des avancées récentes, telles que la modulation Long Range - Frequency Hopping Spread Spectrum (LR-FHSS), ont amélioré le budget de liaison et l'efficacité spectrale par rapport à la modulation LoRa classique, les défis fondamentaux que sont l'estimation de la taille du réseau, l'évolutivité de la liaison montante et la robustesse en cas de congestion restent largement non résolus.

Cette thèse améliore la fiabilité et l'efficacité des systèmes DtS-IoT en relevant ces trois défis fondamentaux. Tout d'abord, nous introduisons de nouveaux mécanismes d'estimation de la taille du réseau pour les systèmes DtS-IoT basés sur LoRa, notamment les modèles améliorés LoRa-Optimistic Collision Information (L-OCI) et OCI tenant compte de la constellation (CL-OCI). Ces estimateurs fonctionnent dans des conditions fortement sujettes aux collisions et fournissent des informations précises sur la charge a priori du réseau, utiles à l'adaptation des mécanismes d'accès au medium (MAC). Deuxièmement, nous proposons un cadre unifié pour améliorer l'évolutivité de LR-FHSS, combinant de nouvelles perspectives sur la conception des séquences de saut de fréquence (Frequency Hopping Sequences, FHS) avec des stratégies d'allocation de démodulateurs telles que *Early-Drop* et *Early-Decode*. Nos résultats montrent des améliorations significatives du volume de données extractibles dans des conditions de forte densité d'objets connectés et de ressources limitées dans les passerelles. Troisièmement, nous concevons un récepteur LR-FHSS amélioré qui permet un décodage robuste des trames dont l'en-tête a été perdu à cause d'un effet Doppler important, en décalage et taux, et d'une forte congestion. En intégrant une reconstruction gloutonne sensible au Doppler et une logique d'alignement des fragments améliorée, le récepteur récupère les trames qui seraient autrement perdues en raison de la corruption de l'en-tête. Cela augmente le taux de réussite global du décodage sans que l'objet connecte ne dépense d'énergie supplémentaire. Quatrièmement, nous abordons la choix entre LoRa et LR-FHSS, pour les communications entre les objets et les satellites, en proposant des méthodes d'accès distribuées tirant parti de techniques légères de détermination de l'orbite des satellites et de balises périodiques. Nous démontrons que les méthodes d'accès conjointes LoRa/LR-FHSS peuvent améliorer l'efficacité énergétique tout en conservant les mêmes performances qu'une approche LR-FHSS-seule.

Dans toutes nos contributions, nous combinons des modèles analytiques avec des simulations à grande échelle utilisant le simulateur FLoRaSat étendu et un simulateur FHS dédié. Les méthodologies et architectures qui en résultent fournissent des voies pratiques vers des déploiements DtS-IoT évolutifs, fiables et économes en énergie.

Thèse accessible à l'adresse : https://theses.insa-lyon.fr/publication/2026ISAL0011/these.pdf © [D. Maldonado Muñoz], [2026], INSA Lyon, tous droits réservés

Thèse accessible à l'adresse : https://theses.insa-lyon.fr/publication/2026ISAL0011/these.pdf © [D. Maldonado Muñoz], [2026], INSA Lyon, tous droits réservés

Contents

Abstract i

Résumé iii

List of Figures ix

List of Tables xi

List of Algorithms xiii

1 Introduction 1
- 1.1 Motivation . . . 1
- 1.2 Contributions . . . 3
- 1.3 Thesis Organization . . . 4

2 Background 5
- 2.1 Satellite technologies . . . 5
  - 2.1.1 Satellite orbits . . . 5
  - 2.1.2 New Space Era and CubeSats . . . 6
  - 2.1.3 Doppler effect . . . 6
- 2.2 LPWAN technologies . . . 7
  - 2.2.1 NB-IoT . . . 7
  - 2.2.2 mioty . . . 7
  - 2.2.3 LoRa . . . 8
  - 2.2.4 LR-FHSS . . . 9
  - 2.2.5 LoRaWAN . . . 11
  - 2.2.6 Doppler constrains for LoRa and LR-FHSS . . . 12

3 Estimation 13
- 3.1 OCI . . . 13
- 3.2 FLoRaSat . . . 15
- 3.3 LoRa-based-OCI . . . 15
  - 3.3.1 L-OCI description . . . 15
  - 3.3.2 Scenario and Parameters . . . 18
  - 3.3.3 Experiments and Results Analysis . . . 18
  - 3.3.4 Conlusion . . . 21
- 3.4 Constellation L-OCI . . . 21
  - 3.4.1 Scenario Model . . . 22
  - 3.4.2 Grouping Approach . . . 23
  - 3.4.3 Ground Track Shift . . . 23
  - 3.4.4 Performance Metrics . . . 24
  - 3.4.5 Evaluation . . . 25

Thèse accessible à l'adresse : https://theses.insa-lyon.fr/publication/2026ISAL0011/these.pdf © [D. Maldonado Muñoz], [2026], INSA Lyon, tous droits réservés

3.4.6 Conlusion 26

4 Scalability **27**
4.1 Introduction to Frequency Hopping Sequences 27
4.1.1 Wide-gap FHS 28
4.2 Construction Method of LR-FHSS Sequences with Semtech's Driver 28
4.3 Proposed general framework 29
4.3.1 FHS Families for LR-FHSS 29
4.3.2 Early Drop and Early Decode Mechanisms for LR-FHSS 31
4.4 Results and Analysis 33
4.4.1 Simulation Settings and Parameters 33
4.4.2 Preliminary Frequency Hopping Sequence Analysis 36
4.4.3 Early Drop and Early Decode Analysis 38
4.4.4 Packet versus Payload Analysis 41
4.4.5 Header Drop Analysis 43
4.4.6 Header Tolerance Analysis 44
4.5 Conclusion 46

5 Robustness **49**
5.1 Background on LR-FHSS Scalability 49
5.2 System Model 50
5.2.1 Signal and Channel Model for LEO Orbits 50
5.2.2 Interference, Collision, and Capture Effect 51
5.2.3 Doppler Effect Model 51
5.2.4 Practical Perspective of System Model Assumptions 53
5.3 Enhanced LR-FHSS Receiver Architecture 54
5.3.1 Headerless Frame Decoding 54
5.3.2 Enhanced LR-FHSS Receiver Architecture 54
5.4 Evaluation 58
5.4.1 Environment 58
5.4.2 Metrics 59
5.5 Results Analysis 61
5.5.1 Transmission Outcome 61
5.5.2 FHS Locator 61
5.5.3 F1 Score 64
5.5.4 Channel Occupancy 65
5.6 Conclusion 66

6 Coordination **69**
6.1 Transmission Control Models 70
6.1.1 LoRa success probability based control 70
6.1.2 ALOHA maximum throughput based control 70
6.1.3 Coding Rate allocation for LR-FHSS 70
6.2 Optimal LoRa Allocation Models 71
6.2.1 On the δ variable calculation 71
6.2.2 2D Strip packing Model 71
6.2.3 1D Packing Model with Sequential Channel Allocation 73
6.3 Distributed Joint LoRa/LR-FHSS Protocols 74
6.3.1 Extending LoRaWAN Class A 74
6.3.2 Proposed Satellite-Aware MAC 74
6.3.3 Proposed Satellite & Interference Aware MAC 75
6.3.4 Summary of methods 78

Thèse accessible à l'adresse : https://theses.insa-lyon.fr/publication/2026ISAL0011/these.pdf © [D. Maldonado Muñoz], [2026], INSA Lyon, tous droits réservés

6.4 Results and Analysis 78
6.4.1 Simulation Scenario and Parameters 78
6.4.2 Performance of Joint LoRa/LR-FHSS MAC Protocols 80
6.4.3 Tuning the Success-Probability Threshold 82
6.4.4 Time-Evolving Performance Across Multiple UL Windows 82
6.5 Conclusion 85

7 Conclusions **87**
7.1 Summary of main contributions 87
7.2 Global discussion 88
7.3 Future work 88

Publications by the Author **91**

References **93**

Thèse accessible à l'adresse : https://theses.insa-lyon.fr/publication/2026ISAL0011/these.pdf © [D. Maldonado Muñoz], [2026], INSA Lyon, tous droits réservés

Thèse accessible à l'adresse : https://theses.insa-lyon.fr/publication/2026ISAL0011/these.pdf © [D. Maldonado Muñoz], [2026], INSA Lyon, tous droits réservés

List of Figures

1.1 Market Snapshot of the satellite IoT Market in 2025 by IoT Analytics [8](original source). 1
1.2 Terrestrial and Non-terrestrial IoT Scenarios. Figure from [10] 2

2.1 Comparison of satellite orbits 5
2.2 Doppler effect observed for different maximum elevation angles θ^*. The satellite orbit at 550 km of altitude and the carrier frequency is 868 MHz. 6
2.3 Time on Air for LoRa CSS and LR-FHSS packets 10
2.4 Division into OCWs, OBWs, and grids for 1 OCW in the European 868 MHz frequency (simplification from [35]) 11

3.1 Naive estimations for frames with different number of slots w 14
3.2 LoRaSync beacon period and slot structure (adapted from [57]) 16
3.3 DtS-IoT simulation scenario (FLoRaSat UI) 18
3.4 Comparison of different L-OCI estimators 19
3.5 Throughput comparison using estimations from Fig. 3.4 20
3.6 Pareto curves for different network sizes obtained from MOP 21
3.7 FLoRaSat UI of a simulated scenario with 50 nodes 24
3.8 RMSE vs. Energy cost of estimates for different values of G, N, and overlapping threshold 25

4.1 Early Drop mechanism illustration for a 13-fragment payload configuration 29
4.2 Unified framework architecture for enhancing LR-FHSS scalability 30
4.3 Early Drop mechanism illustration for a 13-fragment payload configuration 32
4.4 Early Decode mechanism representation for a 13-fragment payload configuration . . 33
4.5 Maximum Hamming Correlation for different LR-FHSS FHS families (*li-fan* and *driver*) 36
4.6 Average Hamming Correlation for different LR-FHSS FHS families (*li-fan* and *driver*) . 37
4.7 Relative collision rate comparison for different LR-FHSS FHS families against the reference Driver family, under conditions of no granularity, no headers, and unlimited decoding capacity 38
4.8 Total decoded payload comparison with 100 demodulators for CR1/3. 39
4.9 Total decoded payload comparison with 100 demodulators for CR2/3. 39
4.10 Total decoded payload comparison with 1000 demodulators for CR1/3. 40
4.11 Total decoded payload comparison with 1000 demodulators for CR2/3. 41
4.12 Total decoded data volume with 100 demodulators, CR1/3, employing Early-Drop and Early-Decode mechanisms. 42
4.13 Total decoded data volume with 1000 demodulators, CR1/3, employing Early-Drop and Early-Decode mechanisms. 42
4.14 Total decoded data volume with 100 demodulators, CR2/3, employing Early-Drop and Early-Decode mechanisms. 44
4.15 Total decoded data volume with 1000 demodulators, CR2/3, employing Early-Drop and Early-Decode mechanisms. 45
4.16 Total decoded data volume with 100 demodulators employing Early-Drop, Early-Decode, Header Drop, and Header Tolerance of 4 time slots. 45

Thèse accessible à l'adresse : https://theses.insa-lyon.fr/publication/2026ISAL0011/these.pdf © [D. Maldonado Muñoz], [2026], INSA Lyon, tous droits réservés

4.17 Total decoded data volume with 1000 demodulators employing Early-Drop, Early-Decode, Header Drop, and Header Tolerance of 4 time slots. 46

5.1 Spectrogram of 100 received LR-FHSS transmissions. 52
5.2 Comparison of received LR-FHSS frames, terrestrial vs. DtS-IoT scenarios. 53
5.3 LR-FHSS gateway architecture incorporating the Enhanced receiver model. 55
5.4 LR-FHSS Decoder transmission outcome statistics for satellite (top) and terrestrial (bottom) deployment scenarios. 62
5.5 FHS Locator classification performance for satellite (top) and terrestrial (bottom) deployment scenarios. 63
5.6 FHS Locator F1 score classification performance for satellite (top) and terrestrial (bottom) deployment scenarios. 64
5.7 Channel occupancy characteristics for satellite (top) and terrestrial (bottom) deployment scenarios. 65

6.1 System model for the DtS-IoT scenario. LEO satellites broadcast LoRa downlink beacons at the beginning of each UL window, providing per-SF interference indicators. End-devices (ED1–ED5) at different elevation angles select either LoRa CSS or LR-FHSS for uplink transmission based on feasibility and load estimates. While a global optimum exists, each device must make a local, suboptimal decision compatible with practical DtS-IoT constraints. 69
6.2 Lowest admissible SF vs time across a 15-min pass (6 satellites). Vertical dashed lines mark a 1-minute UL window. Vertical solid line at $t = 480$ marks the 9th UL window. 80
6.3 Absolute PDR vs. traffic load. Joint LoRa+LR-FHSS vs. pure LR-FHSS. 81
6.4 Relative energy (to pure LR-FHSS) vs. traffic load. Values < 1 favor joint access. . . 81
6.5 Cumulative TX/RX across the pass. *Success Seq-SF* with $P_{\min} \in \{0.2, 0.4, 0.6, 0.8\}$ and *Opt1D*. Solid-circle: unique RX; Dashed-square: total RX; Dash-dot-triangle: unique RX 83
6.6 Running global normalized PDR across windows. *Success Seq-SF* with varying $P_{\min} \in \{0.2, 0.4, 0.6, 0.8\}$ and *Opt1D*. 83
6.7 Per-window throughput (unique payload bytes). Joint methods vs *Opt1D*. 84
6.8 Per-window PDR (over sent packets). Joint methods vs *Opt1D*. 84

Thèse accessible à l'adresse : https://theses.insa-lyon.fr/publication/2026ISAL0011/these.pdf © [D. Maldonado Muñoz], [2026], INSA Lyon, tous droits réservés

List of Tables

2.1 LoRa and LR-FHSS Data Rate Configurations and Parameters 9
2.2 Doppler Shift and Rate resistance for LR1120 device [39] 12

3.1 Study Parameters and Error (Training parameters: w=167, $SF = 10, BW = 125, BCN = 91$) 19

4.1 LR-FHSS FHS Construction Parameters 28
4.2 Simulation configuration parameters 35
4.3 Experimental study parameters 35
4.4 FHS family size and correlation characteristics comparison 36
4.5 Optimal FHS family selection for different LR-FHSS configurations 47

5.1 Simulation Parameters 59

6.1 Comparison of resource allocation methods. 78
6.2 Simulation Parameters 79

Thèse accessible à l'adresse : https://theses.insa-lyon.fr/publication/2026ISAL0011/these.pdf © [D. Maldonado Muñoz], [2026], INSA Lyon, tous droits réservés

Thèse accessible à l'adresse : https://theses.insa-lyon.fr/publication/2026ISAL0011/these.pdf © [D. Maldonado Muñoz], [2026], INSA Lyon, tous droits réservés

List of Algorithms

1 Early Drop Algorithm 32
2 Early Decode Algorithm 33

3 Greedy Headerless Decoding Heuristic (adapted from [35]). 55
4 Proposed Doppler-compensated Greedy Headerless Decoding Heuristic. 57

5 Joint Class A Valid-SF 75
6 ALOHA Best-SF 76
7 Success Seq-SF 77

Thèse accessible à l'adresse : https://theses.insa-lyon.fr/publication/2026ISAL0011/these.pdf © [D. Maldonado Muñoz], [2026], INSA Lyon, tous droits réservés

Thèse accessible à l'adresse : https://theses.insa-lyon.fr/publication/2026ISAL0011/these.pdf © [D. Maldonado Muñoz], [2026], INSA Lyon, tous droits réservés

Chapter 1

Introduction

1.1 Motivation

Low-Earth Orbit (LEO) satellites have become instrumental in extending the coverage of various Internet of Things (IoT) applications, where terrestrial infrastructures are unsuitable due to the challenging geographical locations [6]. These include the environmental and ecological observation of oceans, poles, expansive forests, and extensive natural parks [7]. A recent study conducted by IoT Analytics estimated the number of satellite IoT connections to have reached 7.5 million in 2024, while the satellite IoT market size is expected to surpass $4.7 billion USD by the year 2030 [8]. Figure 1.1 shows a market snapshot of the Satellite IoT market, highlighting some of the key market players.

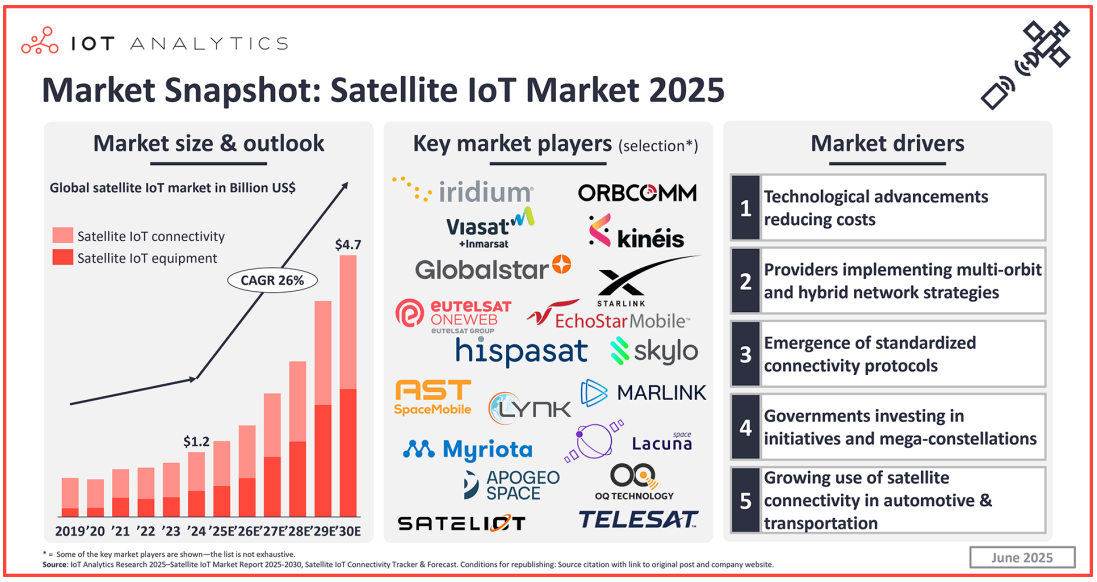


Figure 1.1: Market Snapshot of the satellite IoT Market in 2025 by IoT Analytics [8](original source).

Figure 1.2 depicts both terrestrial and Non-terrestrial scenarios. In a classical terrestrial scenario IoT devices almost always have direct access to an IoT gateway with sufficient computational and energy resources and access to the application serer through the internet. In contrast, a constrained scenario is when gateways don't have direct access to the server but they can still relay information to a Geostationary satellite (GEO) which will forward the data back to a ground station. This approach is called Indirect-to-Satellite scenario.

Thèse accessible à l'adresse : https://theses.insa-lyon.fr/publication/2026ISAL0011/these.pdf © [D. Maldonado Muñoz], [2026], INSA Lyon, tous droits réservés

In an even more constrained scenario, Direct-to-Satellite IoT (DtS-IoT) is a novel approach where IoT devices directly communicate with a LEO satellite [9]. In these cases, LEO satellites are more cost-effective than GEO satellites mainly because of their closer proximity to Earth, reducing transmission delays and power requirements. Small satellites, including affordable CubeSats, enable the establishment of dependable and cost-effective networks by relaying packets to ground stations, possibly through other satellites forming a constellation [10].

DtS-IoT is inherently more sustainable, relying on a small number of nano-satellites and low-power, battery-operated ground terminals, typically consuming power in the milliwatt range. This contrasts broadband mega-constellations such as Starlink, which require thousands of large spacecraft and power-hungry end-user terminals that are significantly more power-hungry, consuming tens of watts [11]. However, this sustainability comes with trade-offs, including lower data rates, higher latencies, and reduced data volumes, characteristic of IoT applications.

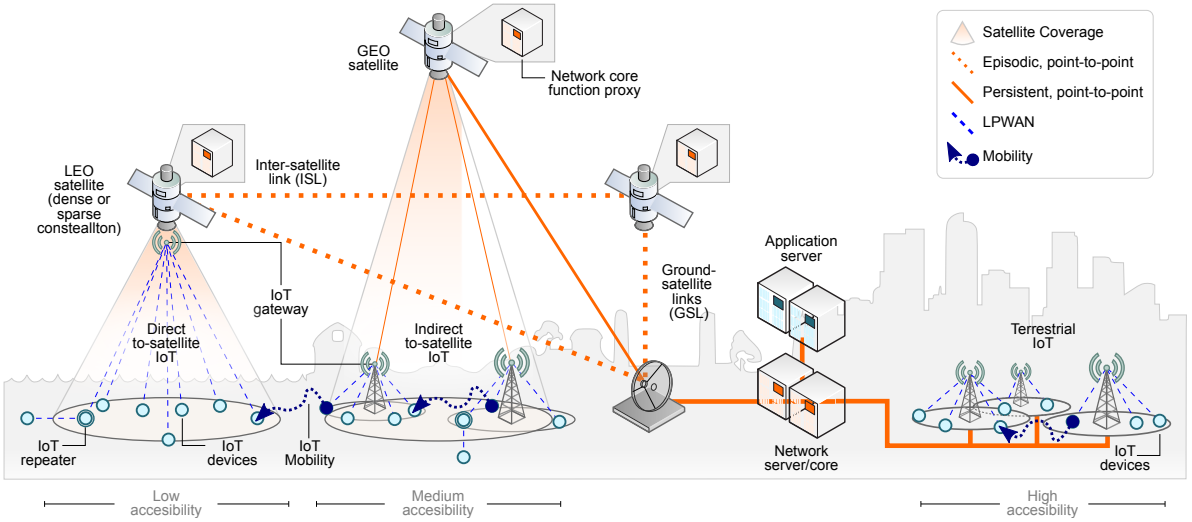


Figure 1.2: Terrestrial and Non-terrestrial IoT Scenarios. Figure from [10]

Conventional Low-Power Wide Area Network (LPWAN) technologies [12], such as LoRa and LoRaWAN, typically employed in terrestrial scenarios, have been recently updated to support DtS-IoT networks [6]. Furthermore, adopting open standards like LoRaWAN facilitates the unrestricted deployment of LoRa networks, as they comply with regional regulations. When coupled with CubeSats, this approach offers an economical alternative for building satellite networks that is competitive with available low-power, low-data rate satellite solutions (e.g., Argos [13], APRS [14], S-AIS [15], and ADS-B [16]).

Moreover, since it is inherently integrated with terrestrial networks, it offers a seamless transition for mobile low-energy devices in applications such as asset tracking. The primary challenge in extending LPWANs to the DtS-IoT domain lies in effectively scaling the medium access schemes to manage the expansive coverage footprint of LEO satellites.

To address the scalability issue while maintaining the high link budget required for direct-to-space communications, Semtech introduced a new modulation technique called Long-Range Frequency Hopping Spread Spectrum (LR-FHSS) [17]. The main advantage of LR-FHSS is that it can evade self-interference by using many narrow-band channels and a frequency hopping technique based on the Frequency Hopping Spread Spectrum (FHSS) method. This is done while maintaining a link budget similar to LoRa's most robust settings. Moreover, most recent LoRa devices are compatible with the LR-FHSS modulation, streamlining LR-FHSS adoption and integration with terrestrial IoT

Thèse accessible à l'adresse : https://theses.insa-lyon.fr/publication/2026ISAL0011/these.pdf © [D. Maldonado Muñoz], [2026], INSA Lyon, tous droits réservés

infrastructures.

Despite these technological advancements, the primary challenge in DtS-IoT networks remains scalability. Managing potentially thousands of end devices under the extensive coverage footprint of a single LEO satellite requires intelligent Medium Access Control (MAC) protocols to address unavoidable packet collisions and enhance overall performance. Specifically:

- MAC Scalability in LoRa: Enhancing throughput requires intelligent MAC schemes that incorporate a priori knowledge of the number of nodes under satellite coverage. Developing technically viable, precise, and accurate network size estimation solutions remains an open research challenge.
- LR-FHSS Resource Bottlenecks: While LR-FHSS boosts scalability, resource allocation at the gateway, particularly the efficient use of demodulators, must be optimized to push performance limits. Additionally, the frequency hopping sequence (FHS) design must be refined to minimize self-interference in dense environments.
- Physical Layer Robustness in LR-FHSS: A leading cause of frame loss in congested LR-FHSS channels is header loss. Furthermore, existing headerless recovery methods often fail to account for the specific characteristics of LEO satellite communications, such most critically, the significant Doppler effects (Doppler shift and Doppler rate) introduced by high orbital velocities.

This thesis addresses these challenges by developing and validating adaptive protocols and advanced receiver architectures across the network stack—from MAC estimation protocols to physical layer demodulation techniques—to achieve robust and scalable DtS-IoT connectivity.

1.2 Contributions

This thesis advances the state-of-the-art in Direct-to-Satellite Internet of Things (DtS-IoT) by addressing four key challenges: network size estimation, scalability, robustness, and multi-modulation coordination in LoRa- and LR-FHSS-based systems. The contributions are organized according to the four main chapters of the manuscript.

Estimation This chapter focuses on network size estimation for LoRa-based DtS-IoT and builds on the works presented in [5, 1]. We first propose L-OCI, the inaugural LoRa/LoRaWAN-compatible realization of the Optimistic Collision Information estimator, and show in realistic FLoRaSat scenarios that it can maintain accurate and energy-efficient network size estimates while operating within the constraints of standard LoRa parameters. Then, we extend this mechanism to multi-satellite constellations through Constellation L-OCI (CL-OCI), which accounts for ground-track shifts and grouped access to significantly increase the range of estimable network sizes while reducing the energy wasted in collisions, thus providing a practical estimation backbone for advanced DtS-IoT MAC protocols.

Scalability The second chapter addresses LR-FHSS scalability and is based on the work in [2]. We first unveil the actual construction of the frequency hopping sequences implemented in commercial LR-FHSS devices, showing that they rely on m-sequences rather than purely random or hash-based designs assumed in prior studies, and then introduce new Wide-Gap FHS families tailored

Thèse accessible à l'adresse : https://theses.insa-lyon.fr/publication/2026ISAL0011/these.pdf © [D. Maldonado Muñoz], [2026], INSA Lyon, tous droits réservés

to LR-FHSS regulatory and structural constraints that exhibit more favorable collision properties in dense deployments. On the receiver side, we propose Early-Decode and Early-Drop demodulator strategies that exploit payload redundancy to free gateway resources as soon as decoding becomes either sufficient or hopeless, and simulations demonstrate that this joint design of sequences and demodulator allocation yields substantially higher decoding capacity and scalability in DtS-IoT scenarios.

Robustness The third chapter targets robustness against Doppler effects and header loss in LR-FHSS, relying on the work presented in [3]. We develop an Enhanced LR-FHSS Receiver architecture that explicitly models the space–terrestrial channel, including Doppler shift and Doppler rate, and integrates a header pre-decoder, a Doppler-compensated FHS locator, and a payload decoder capable of recovering frames even when all header replicas are lost. Extensive simulations in both terrestrial and LEO satellite settings show that this architecture can recover a substantial fraction of frames that legacy receivers lose, thereby improving overall reliability and effectively extending LR-FHSS scalability under realistic DtS-IoT conditions.

Coordination The fourth chapter investigates joint resource allocation for LoRa and LR-FHSS in DtS-IoT, and is based on a work in progress about to be submitted for publication. We first formulate centralized optimal scheduling models for LoRa uplink as time–frequency packing problems that incorporate spreading-factor orthogonality, Doppler feasibility and link budget constraints, and gateway demodulator limits, providing theoretical upper bounds on attainable throughput. Building on these baselines, we then design fully distributed MAC schemes that use lightweight satellite beacons and local orbit- or visibility-aware decisions to select modulation, spreading factor, and access probability per device, and numerical evaluations in realistic multi-satellite scenarios show that this joint LoRa/LR-FHSS operation can achieve noticeably higher throughput and reliability than pure LR-FHSS under moderate to high traffic loads, while exposing a tunable trade-off between efficiency and robustness.

The list of publications by the author is presented at the end of this theses in a separate section from the rest of the references.

1.3 Thesis Organization

The remainder chapters are organized as follows.

Chapter 2 provides the background for this thesis, covering the essentials of satellite and LPWAN technologies. The core contributions are presented in the self-contained Chapters 3, 4, 5 and 6. In Chapter 3 we provide two network size estimation techniques based on the LoRA modulation for DtS-IoT networks. Chapter 4 moves the attention to the LR-FHSS modulation. This chapter contains two approaches tailored to further enhance LR-FHSS scalability. Then, Chapter 5 follows up by presenting a novel technique aiming to recover the payload data from seemingly lost LR-FHSS packets. Finally, in Chapter 6, we aim to solve the problem of choosing the appropriate modulation, either LoRa or LR-FHSS, along with the optimal parameters for each in order to obtain the best possible performance for massive DtS-Iot uplink communications.

Chapter 7 the thesis and discusses future and open research topics.

Thèse accessible à l'adresse : https://theses.insa-lyon.fr/publication/2026ISAL0011/these.pdf © [D. Maldonado Muñoz], [2026], INSA Lyon, tous droits réservés

Chapter 2

Background

2.1 Satellite technologies

2.1.1 Satellite orbits

Figure 2.1 provides an overview of some relevant satellite around the Earth, comparing altitudes, orbital periods and orbital speeds.

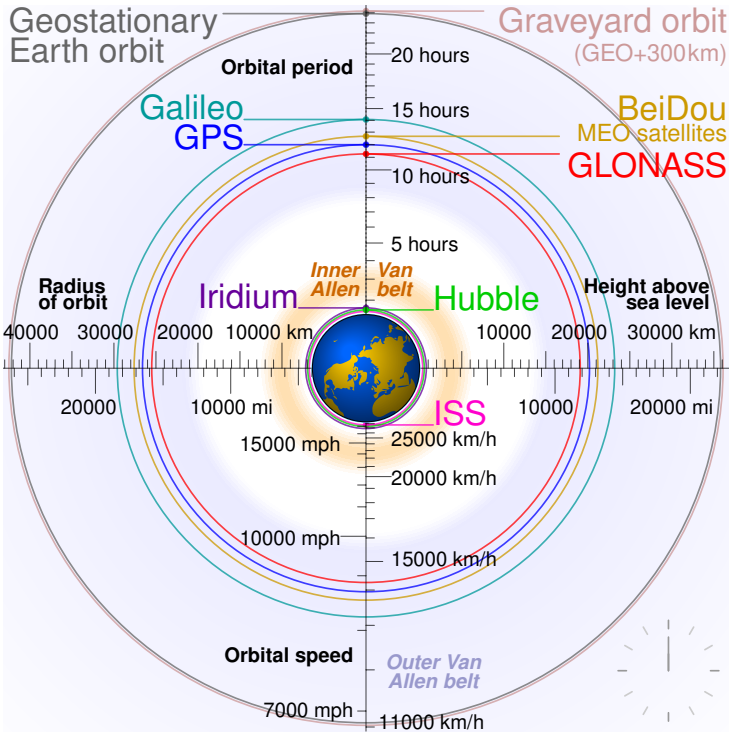


Figure 2.1: Comparison of satellite navigation orbits. *Source:* Adapted from “Comparison satellite navigation orbits.svg” by cmglee, used under CC BY-SA 3.0.

LEO satellites orbiting the Earth at altitudes ranging from 400 to up to 3000 kilometers, though the upper limit is not a consensus. Most of LEO satellites are deployed in orbits below 1000km. Satellite below the 400 km of altitute are called Very Low Earth Orbit (VLEO) satellites. Compared to navigation satellites in the Medium Earth Orbit (MEO), such as GPS, or telecommunication satellites

Thèse accessible à l'adresse : https://theses.insa-lyon.fr/publication/2026ISAL0011/these.pdf © [D. Maldonado Muñoz], [2026], INSA Lyon, tous droits réservés

located at the Geostationary Orbit at altitudes around 35700 km, LEO satellites have a much reduced view of the Earth and thus range. The distance to the horizon for a LEO satellite at 600 kilometers is of around 2800 kilometers. However, the proximity to Earth comes with reduced launching costs so deploying a constellation of LEO satellites can help solve the problem of coverage. In LEO we can find the International Space Station (ISS), the Hubble telescope and the Iridium satellite constellation.

2.1.2 New Space Era and CubeSats

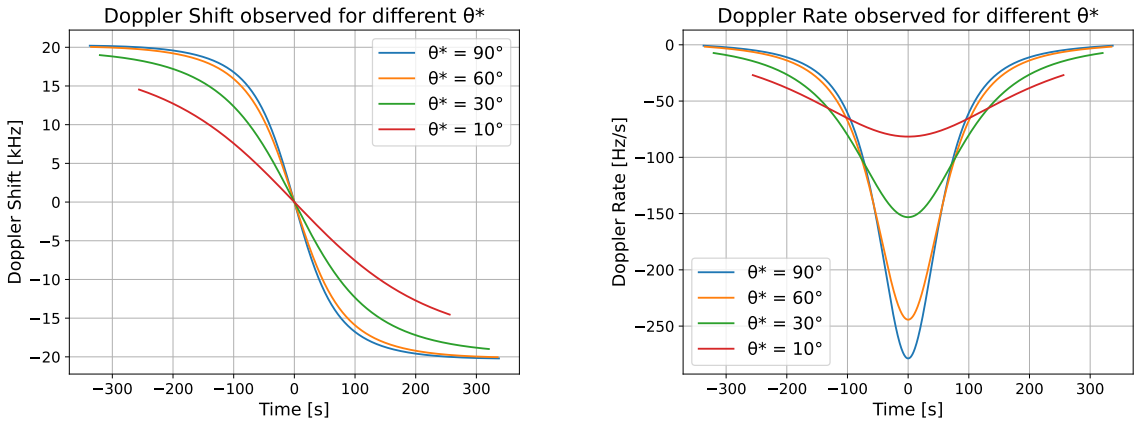
The space sector has been revolutionized in the new millennium due to the development and rapid adoption of the so called CubeSat [18], a standardized nano satellite originally designed for LEO orbits. The CubeSat is composed by one or more basic so-called units (U), a cube measuring 10x10x10 centimeters weighting around 1.33 kilograms. The reduced size and standard design were key factors enabling the considerable decrease the costs and times of all the satellite development phases, from design, manufacture, and testing until launch in orbit. Its use as spatial vehicle for new technologies and space science has been adopted by all actors in both public and private sectors and prompted the inclusion of new actors such as universities and developing countries [19]. The CubeSat is regarded an ideal candidate for the deployment of low-cost DtS-IoT networks [20].

2.1.3 Doppler effect

The Doppler effect is the change in the frequency to an observer who is moving relative to the source of the wave. The change in frequency, also called Doppler shift, is significant in DtS-IoT as orbit the Earth with a speed of around 7 km/h for altitudes around 500 to 600 km. The Doppler shift $f_d(t)$ is given by

$$f_d(t) = -\frac{v(t)}{c} f_c \tag{2.1}$$

, where $v(t)$ is the relative velocity, c is the speed of light and f_c is the carrier frequency.



(a) Doppler shift

(b) Doppler Rate

Figure 2.2: Doppler effect observed for different maximum elevation angles θ^*. The satellite orbit at 550 km of altitude and the carrier frequency is 868 MHz.

Thèse accessible à l'adresse : https://theses.insa-lyon.fr/publication/2026ISAL0011/these.pdf © [D. Maldonado Muñoz], [2026], INSA Lyon, tous droits réservés

As the satellites approaches to a device on ground, the relative distance decreases and the shift will be positive. When the satellite passes the device and moves further away the shift will be negative. Moreover, the Doppler shift also varies over time. The Doppler rate is defined as the rate of change of the Doppler shift. Figure 2.2 depict both the shift and rate for an scenario where the satellite approaches a device on ground with different maximum elevation angles θ^*. An elevation angle of θ equal to 90° is when the satellite is directly over the device. The time 0 corresponds to the instant when the satellite is the closest to the device. The absolute maximum Doppler shift observed for a satellite at 550 km of altitude in the 868 MHz frequency band is 20 kHz, while the maximum Doppler rate experienced is around -280 Hz/s.

2.2 LPWAN technologies

LPWAN is a type of wireless wide-area network designed for long-range communication at low data rates, typically used by IoT devices and other battery-powered sensors. This section focuses on the most relevant LPWANs in the context of DtS-IoT. A more detailed description of LoRa and LR-FHSS is presented as they are the main focus of this thesis.

2.2.1 NB-IoT

Narrow Band IoT (NB-IoT) is a 3GPP-standardized cellular LPWAN profile of Long Term Evolution (LTE) standard that operates on a single 180–200 kHz carrier while reusing the LTE numerology, frame structure, and core network, offering deep coverage, large connection density, and tight Quality-of-Service (QoS) and security integration for massive IoT services [21].

NB-IoT inherits orthogonal frequency-division multiplexing (OFDM) modulation and Single-carrier frequency-division multiple access (SC-FDMA) scheme, a rich set of control and data channels, and stateful radio resource control and core-network procedures, which significantly increases protocol and implementation complexity at both the radio and system levels [22]. This cellular heritage enables flexible in-band, guard-band, and standalone deployment modes and seamless integration into existing LTE/5G infrastructure.

NB-IoT is a key candidate for non-terrestrial networks, where it has been investigated for extending IoT coverage via LEO constellations and for supporting delay- and Doppler-impaired random access in DtS-IoT scenarios[23, 24].

2.2.2 mioty

mioty is a low power wide area network (LPWAN) protocol based on the Telegram-Splitting Ultra narrowband (TS-UNB) radio protocol specified in the standard ETSI TS 103 357 [25]. mioty operates by dividing a data packet into multiple short sub-packets that are transmitted over varying time and frequency patterns while utilizing ultra-narrowband carriers, offering deep coverage, massive connection density, and high interference resilience for massive IoT services in crowded spectrum [25].

mioty is based on the Gaussian Minimum Shift Keying (GMSK) modulation and the Telegram Splitting Multiple Access (TSMA) scheme, a robust Forward Error Correction (FEC) channel coding, and a split-transmission architecture, which significantly reduces implementation complexity at the device while shifting processing load to the software-defined base station [**?**]. This software-centric

Thèse accessible à l'adresse : https://theses.insa-lyon.fr/publication/2026ISAL0011/these.pdf © [D. Maldonado Muñoz], [2026], INSA Lyon, tous droits réservés

design enables flexible deployment in private or public networks and seamless integration into existing license-exempt sub-GHz infrastructure.

mioty shares many similarities with LR-FHSS, and while being a good candidate for DtS-IoT [26], it hasn't caught the same attention as NB-IoT or even LR-FHSS, despite the mioty Alliance [27] being formed before Semtech introduced LR-FHSS [28].

2.2.3 LoRa

Long Range (LoRa) is a proprietary radio communication technique based on Chirp Spread Spectrum (CSS) modulation [29]. The adaptability of LoRa to different scenarios makes it a promising candidate for the DtS-IoT paradigm. LoRa can be operated on the industrial, scientific and medical (ISM) bands. This band are available for use by communication equipment without license and are regulated by governmental agencies for each region, such as the Federal Communications Commission (FCC) in the United States or the European Telecommunications Standards Institute (ETSI) in Europe. This thesis focuses on the European region.

A typical LoRa radio comes with 5 configuration parameters

- Transmission Power (TP): output power of the transmitter. It impacts link budget, coverage range, and energy consumption.
- Carrier Frequency (CF): center frequency of the LoRa channel within the allowed ISM band. It affects regulatory compliance and interference.
- Spreading Factor (SF): signal spreading in time. Trade-off between data rate and range (higher SF = lower rate, longer range).
- Bandwidth (BW): width of the chirp spectrum. Defines data rate and receiver sensitivity.
- Coding Rate (CR): forward error correction redundancy. It allows to improve robustness to errors at the cost of additional airtime.

An appropriate selection of these parameters is required for the proper operation of a LoRa-based network, specific for each use case scenario. Table 2.1 shows the configurations available and the encoding used for Data Rate (DR) in the European regional band EU863-870 as described in Table 10 from [30]. Table 2.1 also shows the bit rate, the sensitivity levels and the maximum payload size for each DR. DR12 and DR13 were recently allowed support and their sensitivity is not reported yet. As Semtech reports [31], LR-FHSS modulation has similar link budget as SF12.

The transmission time (or Time on Air) is of great relevance in LoRa-based DtS-IoT scenarios. It is calculated according to the following set of equations:

$$T_{\text{sym}} = \frac{2^{SF}}{BW} \tag{2.2}$$

$$T_{\text{preamble}} = (n_{\text{preamble}} + 4.25)T_{\text{sym}} \tag{2.3}$$

Thèse accessible à l'adresse : https://theses.insa-lyon.fr/publication/2026ISAL0011/these.pdf © [D. Maldonado Muñoz], [2026], INSA Lyon, tous droits réservés

Data Rate	Configuration	Bit rate [bit/s]	Sensitivity [dB]	Max. payload [bytes]
DR0	LoRa: SF12 / 125kHz	250	-137	59
DR1	LoRa: SF11 / 125kHz	440	-134.5	59
DR2	LoRa: SF10 / 125kHz	980	-132	59
DR3	LoRa: SF9 / 125kHz	1760	-129.5	123
DR4	LoRa: SF8 / 125kHz	3125	-127	230
DR5	LoRa: SF7 / 125kHz	5470	-124.5	230
DR6	LoRa: SF7 / 250kHz	11000	-121	230
DR7	FSK: 50 kbps	50000	-	230
DR8	LR-FHSS CR1/3: 137kHz	162	-137	58
DR9	LR-FHSS CR2/3: 137kHz	325	-137	123
DR10	LR-FHSS CR1/3: 336kHz	162	-137	58
DR11	LR-FHSS CR2/3: 336kHz	325	-137	123
DR12	LoRa: SF6 / 125kHz	9375	x	230
DR13	LoRa: SF5 / 125kHz	15625	x	230

Table 2.1: LoRa and LR-FHSS Data Rate Configurations and Parameters

$$n_{\text{payload}} = 8 + \max\left(\left\lceil \frac{8PL - 4SF + 28 + 16CRC - 20H}{4(SF - 2DE)} \right\rceil (CR + 4),\ 0\right) \tag{2.4}$$

$$T_{\text{payload}} = n_{\text{payload}} \cdot T_{\text{sym}} \tag{2.5}$$

$$T_{\text{packet}} = T_{\text{preamble}} + T_{\text{payload}} \tag{2.6}$$

Eq. (2.6) corresponds to the total Time on Air of a LoRa transmission, considering both the preamble and payload time (refer to the LoRAWAN specification [17] for a detail description of packets). Eqs. (2.2), (2.3), (2.4) and (2.5) depend on the following extra parameters (on top of the aforementioned configuration parameters):

- PL: payload size in byte
- H: header status, 0 is enabled and 1 is disabled
- DE: Low Data Rate Optimize, 0 is disabled and 1 is enabled
- CRC: Cyclic Redundancy Check, 0 is disabled and 1 is enabled
- n_{preamble}: number of symbols in preamble

Figure 2.3 shows the time on air (ToA) as a function of the payload data for different SFs for LoRa with BW = 125 kWh, comapared with ToA for LR-FHSS.

2.2.4 LR-FHSS

LR-FHSS is a modulation technique that leverages many narrow-band channels to perform rapid frequency hopping within a single frame. Primarily tailored for uplink communications, LR-FHSS

Thèse accessible à l'adresse : https://theses.insa-lyon.fr/publication/2026ISAL0011/these.pdf © [D. Maldonado Muñoz], [2026], INSA Lyon, tous droits réservés

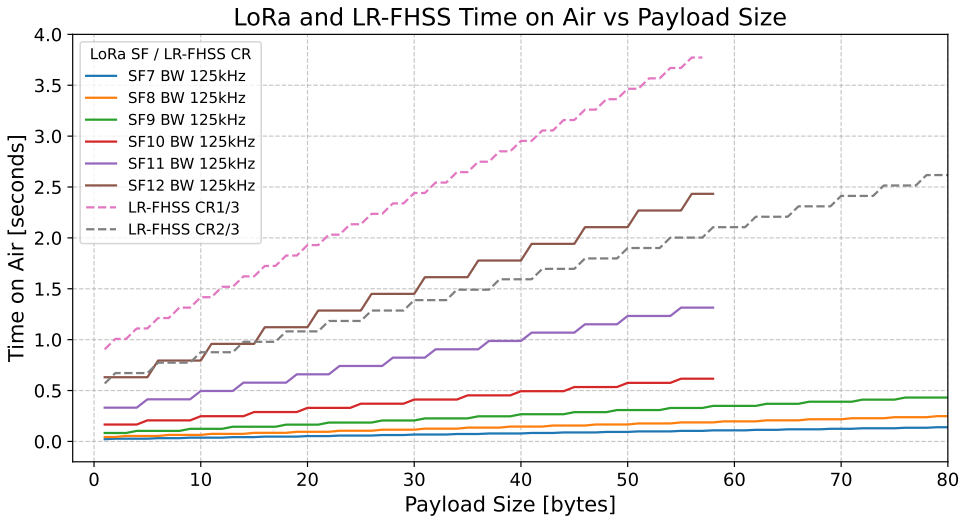


Figure 2.3: Time on Air for LoRa CSS and LR-FHSS packets

proves particularly efficient when many energy-limited devices transmit simultaneously to LEO satellites, thanks to the large number of narrow-band channels LR-FHSS uses.

LR-FHSS segments the frequency band into Occupied Channel Width (OCW) channels. Each OCW is further partitioned into multiple narrow-band channels called Occupied Bandwidth (OBW) [32]. As illustrated in Fig. 2.4, an individual OBW acts as a physical subcarrier with a bandwidth set at 488 Hz. Within each OBW, LR-FHSS utilizes a Gaussian Minimum-Shift Keying (GMSK) modulation, prized for its exceptional spectral and energy efficiency [33]. To align with regional regulations stipulating the minimum spacing between subcarriers in the FHS, OBWs are systematically arranged into grids. Grids comprise non-sequential OBWs spaced apart by a mandated minimum distance, whose value depends on regional regulatory standards (e.g., 3.9 kHz in the EU). For instance, in the EU, Grid 1 contains OBWs 1, 9, 17, . . ., while Grid 2 contains OBWs 2, 10, 18, ... These grids play a pivotal role in LR-FHSS: a hopping sequence within any given frame is restricted to using OBWs within the same grid. A summary of the LR-FHSS parameters for chosen channels, including Data Rate (DR) modes and Frequency Hopping (FH) channels, together with details on the OCW channel bandwidth, OBW channel count, and the number of grids specified for LR-FHSS, are provided in [34]. Note that the large number of OBW channels (between 280 and 3120) is the core of the scalability of LR-FHSS.

Frame transmission initiates with multiple header copies, called replicas, each lasting 233 ms in airtime. Depending on the chosen data rate scheme, the header is replicated two or three times to ensure reliable reception. Note that the reception of a single replica is needed to retrieve the header. Then, replicas are followed by the segmented payload, where each segment, called a fragment, lasts 102.4 ms in airtime. These replicas and fragments are relayed over varying OBWs within a single grid, according to the FHS. Every header replica conveys the index of the chosen FHS. The diversity of sequences, typically 512, combined with the large number of OBWs, reduces the possibility of multiple frames adopting an identical hopping sequence. Payload encoding is designed to keep data integrity intact even with substantial fragment loss [32]. The LoRaWAN standard prescribes two LR-FHSS configurations:

- Robust Configuration: Headers are transmitted three times, and the payload is encoded at CR = 1/3, meaning that successful frame recovery demands a minimum of 33% fragment decoding.
- Fast Configuration: Headers are transmitted twice, and the payload is encoded at CR = 2/3,

Thèse accessible à l'adresse : https://theses.insa-lyon.fr/publication/2026ISAL0011/these.pdf © [D. Maldonado Muñoz], [2026], INSA Lyon, tous droits réservés

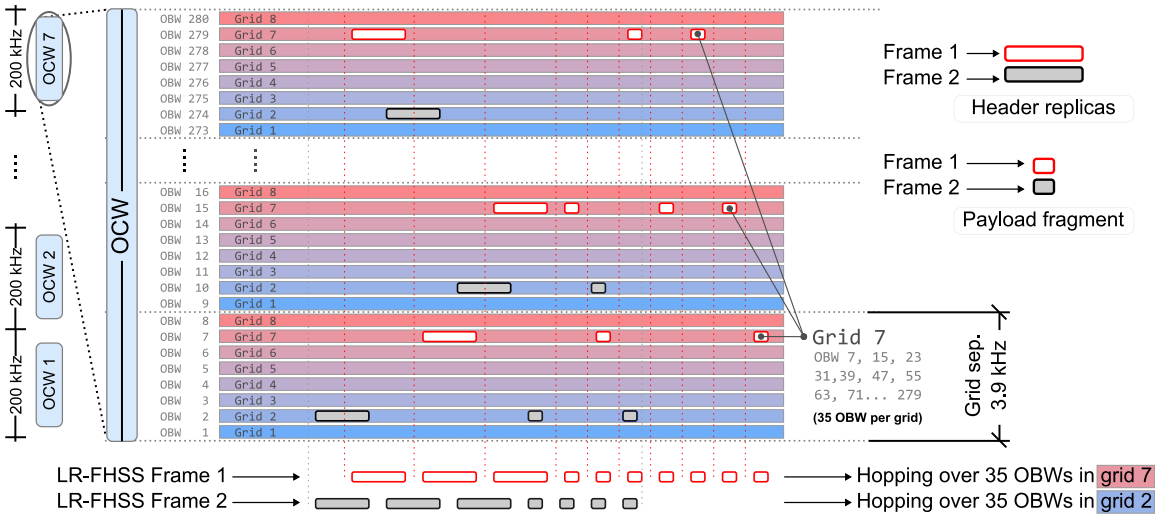


Figure 2.4: Division into OCWs, OBWs, and grids for 1 OCW in the European 868 MHz frequency (simplification from [35])

meaning that successful frame recovery demands a minimum of 67% fragment decoding.

A crucial element impacting the scalability of LR-FHSS is the FHS, which fundamentally determines how LR-FHSS frames with different sequences overlap and, subsequently, the extraction rate of colliding LR-FHSS frames. This relationship encompasses the intricate interplay between LR-FHSS's error correction mechanisms and the mandatory frequency shifts dictated by grid definitions. However, to our knowledge, there is a lack of studies on the design of appropriate FHS techniques for LR-FHSS, such as those in the Wide-Gap FHS (WGFHS) family.

2.2.5 LoRaWAN

LoRaWAN is the data link layer built on top of the LoRa modulation. The LoRaWAN specification [17] is developed and maintained by the LoRa Alliance [36], an open non-profit organization whose goal is to promote the use of LoRaWAN for IoT applications. The LoRaWAN specification defines three operation modes, Class A, Class B, and Class C, to enhance the adaptability of the network to different use scenarios.

All three operations modes follow the ALOHA protocol [37] for Medium Access Control (MAC), meaning a device can initiate an uplink transmission at any time but always respecting the duty cycle restriction imposed by the specific regional parameters [30].

After a transmission, the IoT device opens two reception windows (in green) in order to receive a downlink transmission sent by the network server through the designated gateway. This base operation mode constitutes the Class A mode, which is the most energy efficient one but restraining the IoT device to receive downlink messages only after it has sent an uplink transmission, impacting negatively the downlink throughput specially when the usage scenario requires the IoT device to constantly receive instructions from the network server.

In order to improve the downlink throughput, Class B operation mode defines periodic reception windows (in blue) allowing the gateway to transmit downlink messages even if the IoT device does not have uplink messages to sent. This requires synchronization between the IoT device and the gateway, achieved through a periodically scheduled beacon message broadcast by the gateway. With

Thèse accessible à l'adresse : https://theses.insa-lyon.fr/publication/2026ISAL0011/these.pdf © [D. Maldonado Muñoz], [2026], INSA Lyon, tous droits réservés

this approach, the downlink throughput can be improved at the expense of energy efficiency due to the opening of extra reception windows.

Lastly, in scenarios where energy constraints are not a problem for IoT devices, Class C allows the IoT device to receive downlink messages whenever it is not transmitting an uplink message (in yellow).

2.2.6 Doppler constrains for LoRa and LR-FHSS

Table 2.2 summarizes the Doppler resistance as reported by Semtech for the LR1120 devices [38] [39]. We are interested in the LR1120 in particular since it is one of the first commercially available devices to support LR-FHSS. For LoRa modulation, the Shift resistance depends only on the bandwidth B. The maximum drift over the duration of a single symbol Δf_{sym} is given by Eq. (2.7), where T_{sym} is the symbol time. Then, the maximum Rate is given by $\frac{\Delta f_{\mathrm{sym}}}{T_{\mathrm{sym}}}$. On the other hand, the LR-FHSS Shift resistance depends on the regional configuration, while the Rate resistance is a fixed value.

$$\Delta f_{\mathrm{sym}} = \frac{0.1 \times B}{2^{\mathrm{SF}}} = \frac{1}{10 T_{\mathrm{sym}}} [\mathrm{Hz/symbol}] \tag{2.7}$$

Table 2.2: Doppler Shift and Rate resistance for LR1120 device [39]

Configuration	Sensitivity	Shift limit	Rate limit
LoRa SF7	-124.5 dB	$\pm 0.25 \times B$	$95367\,\mathrm{Hz/s}$
LoRa SF8	-127 dB	$\pm 0.25 \times B$	$23841\,\mathrm{Hz/s}$
LoRa SF9	-129.5 dB	$\pm 0.25 \times B$	$5960\,\mathrm{Hz/s}$
LoRa SF10	-132 dB	$\pm 0.25 \times B$	$1490\,\mathrm{Hz/s}$
LoRa SF11	-134.5 dB	$\pm 0.25 \times B$	$372\,\mathrm{Hz/s}$
LoRa SF12	-137 dB	$\pm 0.25 \times B$	$93\,\mathrm{Hz/s}$
LR-FHSS EU136	-137 dB	$31.64\,\mathrm{kHz}$	$800\,\mathrm{Hz/s}$
LR-FHSS EU335	-137 dB	$32.03\,\mathrm{kHz}$	$800\,\mathrm{Hz/s}$
LR-FHSS US1523	-137 dB	$38.3\,\mathrm{kHz}$	$800\,\mathrm{Hz/s}$

From the results shown in Figure 2.2 it is concluded that both LoRa and LR-FHSS are resistant to Doppler effect for a LEO satellite and in the 868 MHZ, except for SF12 which can experience impairments in cases when the Doppler rate is considerable.

Thèse accessible à l'adresse : https://theses.insa-lyon.fr/publication/2026ISAL0011/these.pdf © [D. Maldonado Muñoz], [2026], INSA Lyon, tous droits réservés

Chapter 3

Estimation

In this chapter we introduce two network size estimatiors for LoRa-based DtS-IoT network.

We first extend an previous state-of-the-art estimation method, the Optimistic Collision Information-based (OCI) estimator, designer for generic Non-terrestrial networks with focus on IoT networks [40]. OCI optimizes energy efficiency and reduces computational requirements while providing accurate estimations. We extend this estimator to be LoRa compliant and propose the LoRa-based-OCI (L-OCI) estimator [5]. Then, L-OCI is further extended for satellite constellation support, named Constellation L-OCI (CL-OCI) [1].

3.1 OCI

OCI is based on the observation that in a network with a large number of nodes, collisions frequently occur, while in a network with a small number of nodes, collisions occur less frequently. OCI uses the probability of successful transmission to calculate the number of nodes in the network. To this end, nodes transmit (small) dummy frames, and OCI estimates the number of participating nodes on the receiver side[40]. The OCI estimator has been proven to be highly accurate with a low Root Mean Square Error (RMSE) compared to other state-of-the-art estimators. Moreover, the OCI mechanism is computationally efficient, making it feasible to implement on-board resource-constrained nano-satellites. The OCI estimator operates as follows.

Data Collection Phase Participating nodes uplink dummy frames following a Frame Slotted ALOHA (FSA) delimited by a beaconing system. After the transmission of a beacon, the frame starts. During the frame, the satellite determines the status of each uplink slot, which can be categorized as *idle*, *successful*, or *collided* depending on whether there is no received signal (below power sensitivity), a successful signal decode occurs, or two or more nodes attempt to transmit on the same slot, respectively. The resulting tuple i, c, s represents the number of *idle*, *collided*, and *successful* slots, respectively. It should be noted, however, that a slot may be perceived as *idle* by the satellite, even when multiple nodes attempt to transmit on the same slot. Still, low reception power makes successful decoding infeasible.

Naive Estimation Phase Using the collected data, a simple estimate of the number of nodes n_k within the satellite's footprint (or cluster size) during frame k is obtained, assuming that no more

Thèse accessible à l'adresse : https://theses.insa-lyon.fr/publication/2026ISAL0011/these.pdf © [D. Maldonado Muñoz], [2026], INSA Lyon, tous droits réservés

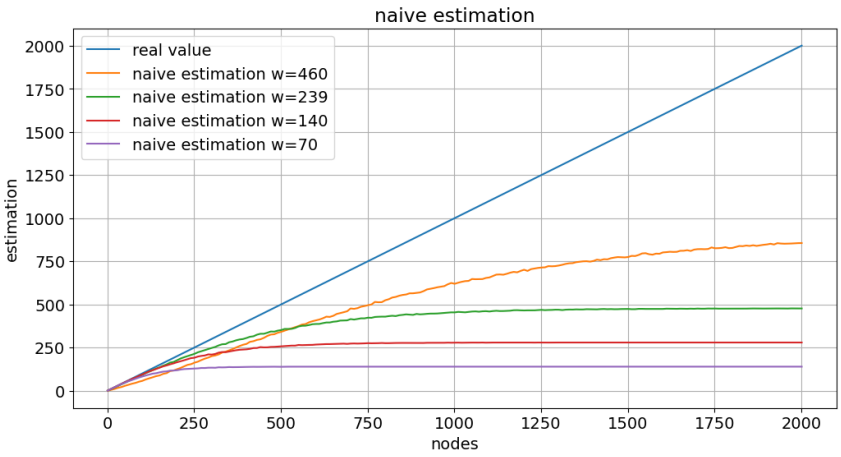


Figure 3.1: Naive estimations for frames with different number of slots w

than two nodes are involved in every collision. This estimate ϕ of n_k is computed as $\phi = s + 2c$. However, it should be noted that the naive estimation may not be accurate in realistic scenarios where high-order collisions are not neglected, and it may underestimate the number of nodes when $n_k > w$. Fig. 3.1 illustrates the naive estimation as a function of the cluster size n_k for various frame lengths in terms of slots w, demonstrating that it always converges to $2w$.

Polynomial Fitting Phase To address the underestimation issue without knowledge of the order of collisions, OCI creates a function that maps the naive estimations curve to the real number of nodes curve. For this method to work, the naive estimations and the real number of nodes must be bijective, and the frame length w must be long enough so that the naive estimation has no repeated values. To create the function, two polynomial fits are utilized. The first fit is applied to smooth the naive estimation curve, while the second fit maps the resulting curve of the first fit to the real number of nodes curve.

Operation Phase After obtaining the polynomial coefficients of the second fit, the OCI mechanism enters the operational phase, where the function is applied to the naive estimation to obtain the OCI estimation of the real value. The value obtained from OCI can be utilized to optimize the performance of MAC schemes by regulating their operation. This value can be stored onboard or delivered to ground operations for future use.

The efficiency of OCI is remarkable and discussed in [40]. However, the OCI estimator was conceived based on a series of assumptions that limit its applicability. The assumption that the beacon is always decoded and all nodes remain synchronized with the satellite neglects the potential for errors in realistic DtS-IoT networks. The model assumes that each frame contains a separate stable cluster of nodes that remain under satellite coverage for the entire time frame. However, in a realistic scenario, the nodes within the satellite's coverage area can experience rapid changes. Some nodes may receive the beacon signal but subsequently move out of coverage, while others may come into coverage but miss the beacon. Moreover, the model only accounts for collisions as the cause of data loss, neglecting the possibility of the capture effect signal strength below the receiver sensitivity level.

In the subsequent section, we present a modification of the OCI estimator tailored to the practical LoRa/LoRaWAN protocols implemented in DtS-IoT, thereby alleviating the aforementioned idealized premises.

Thèse accessible à l'adresse : https://theses.insa-lyon.fr/publication/2026ISAL0011/these.pdf © [D. Maldonado Muñoz], [2026], INSA Lyon, tous droits réservés

3.2 FLoRaSat

FLoRaSat (Framework for LoRa-based Satellite Networks) is a simulation tool built on top of OMNeT++ discrete-event simulator [41] to model end-to-end satellite IoT scenarios using LoRa/LoRaWAN adaptations for space applications [42]. FLoRaSat is free and open-source avelable online [1].

The simulator is a combination of several existing frameworks.

- The INET framework [43] is an open-source OMNeT++ model suite for wired, wireless and mobile networks. It has grown over the years to become one of the essential libraries for building network simulators in OMNeT++.
- The LoRa portion of the simulation software is founded on the FLoRa (Framework for LoRa) [44], initially designed to investigate IoT applications in urban and suburban areas.
- To incorporate satellite mobility, the *OS3* [45] and *leosatellites* [46] frameworks were updated and adapted, resulting in a suitable implementation of the SGP4 orbital propagator model.

The FLoRaSat simulator continues to be under development. New, improved and more complete versions have been developed and made available, facilitating the simulator usability, accessibility and capabilities [47, 48].

FLoRaSat has been used to study different topics on multiple layers concerning NTN scenarios, notably MAC protocols [49, 50, 51, 52] and network size estimators [5, 1], on the Link layer, but also routing algorithms on the Transport layer [4, 53]. Additionally, optimal network server placement, on the Network layer, was studied with FLoRaSat in [54], and an IoT-based deep space scenario was discussed in [55]. Lastly, FLoRaSat was included in a survey on NTN networks simulators [56].

3.3 LoRa-based-OCI

3.3.1 L-OCI description

One cannot directly use the OCI estimator in LoRa-based networks without extending the MAC layer specified by LoRaWAN. Specifically, a protocol based on a TDMA technique with time-slotted frames and a time synchronization system must be added to the MAC layer.

For L-OCI, we leverage LoRaSync [57], which we find is an appropriate Class B variant technique that satisfies the synchronization requirements of OCI and DtS-IoT. LoRaSync extends LoRaWAN Class B by adopting a beaconing mechanism that enables time synchronization and scheduling uplink slots during the beacon window. LoRaSync is itself an extension of the *Class S* mechanism previously proposed by the same authors in [58]. Fig. 3.2 depicts the structure of the beacon period, which is divided into three phases.

Beacon Reserved Phase During this phase, the gateway broadcasts the beacon, and ground nodes decode it. To optimize energy usage, avoiding persistent reception in resource-constrained nodes is important. Therefore, it is necessary to use appropriate techniques such as [59] to estimate

[1] FLoRaSat simulator.

Thèse accessible à l'adresse : https://theses.insa-lyon.fr/publication/2026ISAL0011/these.pdf © [D. Maldonado Muñoz], [2026], INSA Lyon, tous droits réservés

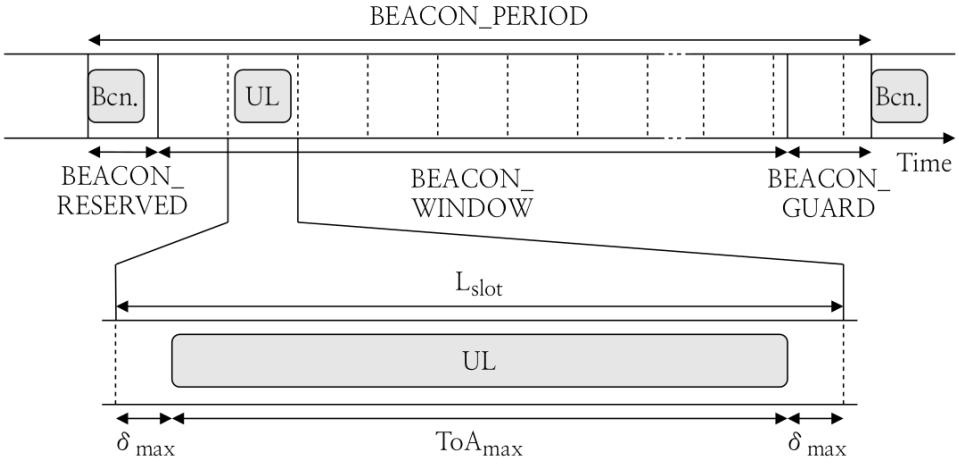


Figure 3.2: LoRaSync beacon period and slot structure (adapted from [57])

the satellite visibility, which can determine the optimal time to open the reception window. Once the beacon is received, the node will be synchronized on a frame level.

Beacon Window Phase Then, uplink slots (UL) are slotted in time during this phase. A UL includes a maximum clock offset threshold time $\delta_{\max}$ at the beginning and end of the slot and a maximum time on air $\mathrm{ToA}_{\max}$ in between, which depends on the LoRa parameters and the payload size. The time on air is given by Eq.(2.6). The parameter $\delta_{\max}$ provides the required time synchronization contention guards for the beacon and clock drifts in DtS-IoT. Note that the downlink mechanism defined by LoRaWAN Class B still exists but is not depicted here since user data downlinks are unnecessary for L-OCI estimation.

Beacon Guard Phase Finally, the beacon period ends with the guard phase, allowing the gateway to decode the last transmissions.

The number of slots w in the frame is a crucial parameter for L-OCI, as illustrated in Fig. 3.1. It is calculated as $w = \lfloor T_{\mathrm{win}}/T_{\mathrm{slot}} \rfloor$, where T_{win} is the beacon window time, and T_{slot} is slot duration. Therefore, w depends on the frame length, the maximum time-on-air ($\mathrm{ToA}_{\max}$), and the underlying LoRa parameters. The choice of SF and BW parameters of LoRa, and the frame length influence this non-trivial trade-off that determines the optimal operation of L-OCI.

A higher SF (e.g., SF12) increases communication range and $\mathrm{ToA}_{\max}$ but reduces the number of slots in the frame, which can limit the number of transmission opportunities. Conversely, a lower SF like (e.g., SF9) reduces both communication range and $\mathrm{ToA}_{\max}$, allowing more slots in the frame but reducing communication range. An optimal L-OCI parameter selection mechanism is provided below.

Parameter Selection Algorithm

The parameters involved in LoRa and LoRaSync are numerous. This study focuses on three specific parameters: Spreading Factor (SF), Bandwidth (BW), and frame length (BCN). A heuristic approach is proposed to determine the optimal combination of parameters $x = (SF, BW, BCN)$ for a given cluster size n_k. To establish an optimal solution, a Multi-objective Optimization Problem (MOP) is defined in this study based on two objectives related to the OCI estimator. The first objective is

Thèse accessible à l'adresse : https://theses.insa-lyon.fr/publication/2026ISAL0011/these.pdf © [D. Maldonado Muñoz], [2026], INSA Lyon, tous droits réservés

minimizing the energy spent to obtain the estimator's polynomial coefficients, while the second is minimizing the estimation error.

The problem is formalized as

$$\text{minimize } F(x) = (f_1(x), f_2(x))^T, \text{ s.t. } x \in \Omega, \tag{3.1}$$

where Ω is the decision space.

The first objective function, $f_1(x)$, is the amount of energy consumed in transmissions that failed to be decoded due to collisions or insufficient received signal power during the OCI estimation phase. The second objective, $f_2(x)$, is the estimation error attained during the OCI test phase. Here, x is only constrained to live in Ω.

Various methods address the MOP presented in equation (3.1). The approach utilized in this study is MOEA/D [60], a genetic programming-based algorithm that facilitates obtaining the Pareto curve of optimal solutions for a given multi-objective optimization problem. It is chosen due to its excellent search performance and high computation efficiency. To adapt the problem to MOEA/D, the parameter vector x was converted into the decision vector $\bar{x} = \{w(SF, BW, BCN), \mathrm{ToA}_{\max}(SF, BW)\}$. The remaining parameters of LoRa and LoRaSync are treated as fixed values. The Pareto curve of the optimal solution to the MOP is obtained by the MOEA/D algorithm, which decomposes the objectives into two scalar optimizations. During each generation, the population of candidates' objective function $F(x)$ is calculated by simulating a smaller version of L-OCI. The model considers the spatial distribution of the network using LoRaSync, making it more accurate than OCI but less than L-OCI as implemented in the FLoRaSat simulator.

Performance Metrics

RMSE To assess the efficacy of the OCI estimations, the evaluation criterion of choice is the Root-Mean-Square Error (RMSE), also used in [40].

The RMSE is derived through the calculation of the formula

$$\epsilon_{\mathrm{rsme}} = \sqrt{\sum_{k=1}^{K} (\phi_k - n_k)^2 / K}, \tag{3.2}$$

where K corresponds to the number of clusters being examined, n_k signifies the actual number of nodes in the kth cluster, and ϕ_k denotes the estimated value of n_k. This approach provides an intuitive measure of the accuracy of the estimator's predictions by quantifying the differences between the predicted and actual values of network size, thereby allowing for comparing the estimator's performance under different network configurations.

Throughput Slotted Aloha Game (SAG) [61] is a MAC protocol proposed for satellite networks using FSA communication, thus suitable for OCI and L-OCI. SAG gives a transmission probability to each node based on the number of slots and the currently active nodes in the network (estimated with OCI or L-OCI). If there are fewer nodes than slots, the probability is set to 1, meaning all nodes will attempt to transmit during the frame. If there are more nodes than slots, the probability is adjusted so that the number of nodes attempting to transmit is close to the number of slots. SAG aims to achieve the maximum theoretical throughput with arbitrarily large node populations. It is calculated as the number of successful transmissions in a frame divided by the time length of the frame in slots.

Thèse accessible à l'adresse : https://theses.insa-lyon.fr/publication/2026ISAL0011/these.pdf © [D. Maldonado Muñoz], [2026], INSA Lyon, tous droits réservés

3.3.2 Scenario and Parameters

This study considers a specific scenario where a Low Earth Orbit (LEO) satellite serves as the DtS-IoT gateway for relaying packets from ground nodes to the network server via a ground station. The satellite is assumed to be in a circular orbit with an altitude of 600 kilometers and an inclination of 98 degrees. Ground nodes are randomly and uniformly deployed over a circular region. The satellite is positioned directly above the deployment center to ensure all nodes receive L-OCI's beacon signal. Consequently, all nodes attempt to transmit during the frame on a randomly selected slot according to a uniform distribution. Fig. 3.3 depicts this scenario using the FLoRaSat GUI, where the red area represents the communication range based on the selected parameters.

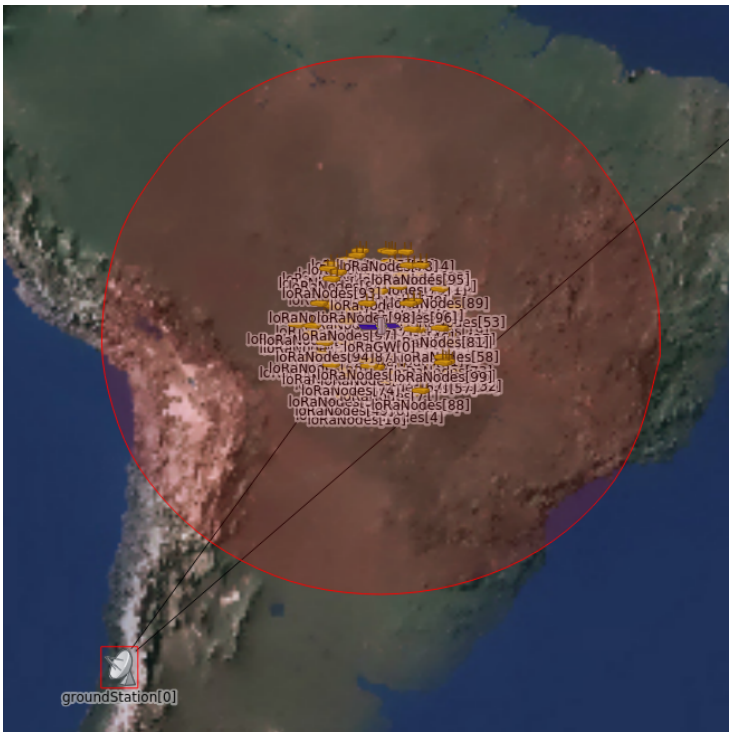


Figure 3.3: DtS-IoT simulation scenario (FLoRaSat UI)

The control variables of our study are the spreading factor (SF), the bandwidth (BW) of LoRa in kHz, and the beacon period (BCN) in seconds. At the same time, the remaining parameters comply with the LoRa Alliance specification for the European region [30]. The payload size is set to 20 bytes. We determine the time on air (*airtime*) and the maximum range of communication (*range*) for a LoRa transmission based on the values of (SF, BW). The channel model assumed is a free space path loss model, and we consider the received sensitivity values from a typical LoRa transceiver, Semtech's SX1272 [62]. We run 30 simulation repetitions with different seeds for each input set (SF, BW, BCN).

3.3.3 Experiments and Results Analysis

Sensitivity to LoRa Parameters

This experiment studies the influence of several L-OCI estimators trained using different sets of parameters listed in Table 3.1 on a simulation with identical settings $(SF = 10, BW = 125, BCN = 91)$. The study employs $w = 167$ slots and varies the number of nodes from 1 to 501 in increments

Thèse accessible à l'adresse : https://theses.insa-lyon.fr/publication/2026ISAL0011/these.pdf © [D. Maldonado Muñoz], [2026], INSA Lyon, tous droits réservés

of 10 nodes. The RSME of the estimators is presented in the last column of Table 3.1, and their estimations are illustrated in Fig. 3.4. At the same time, the nodes' positions are adjusted with respect to the training phase.

Table 3.1: Study Parameters and Error (Training parameters: w=167, $SF = 10, BW = 125, BCN = 91$)

SF	BW	BCN	RSME
9	125	50	29.693
10	125	91	5.556
11	250	80	5.586
11	125	152	5.747
12	125	295	17.909

Although the smallest RSME is achieved when the simulation parameters match the trained L-OCI ($(SF = 10, BW = 125, BCN = 91)$), SF11 yields comparable performance, even when operating in a different BW, unlike SF9 and SF12. Further analysis revealed a considerable number of lost transmissions due to weak signal power in the reception during the L-OCI estimation phase, resulting in an overestimation of the number of nodes by L-OCI. The findings suggest that L-OCI is insensitive to LoRa's SF10 and SF11 and that a single L-OCI estimator can be applied to both.

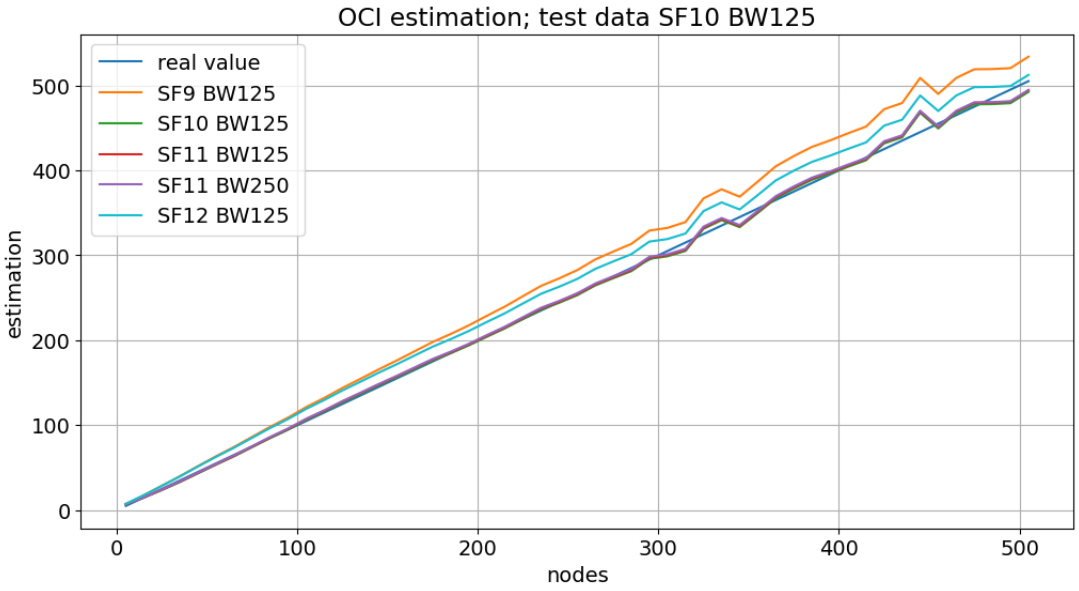


Figure 3.4: Comparison of different L-OCI estimators

Impact on Throughput

In this experiment, we investigate the impact of using L-OCI estimations on the throughput of the SAG protocol, as presented in [61, 40], during the operational phase. We use the OCI estimations with $BW = 125$ obtained from the previous experiment: SF9, SF10, and SF12. The obtained throughput is compared with the FSA pure throughput, where no uplink throttling is applied, serving as a baseline. ALOHA's maximum theoretical throughput is provided in a red horizontal line. The results are presented in Fig. 3.5.

We explain the results above ALOHA's theoretical throughput with the capture effect modeled in

Thèse accessible à l'adresse : https://theses.insa-lyon.fr/publication/2026ISAL0011/these.pdf © [D. Maldonado Muñoz], [2026], INSA Lyon, tous droits réservés

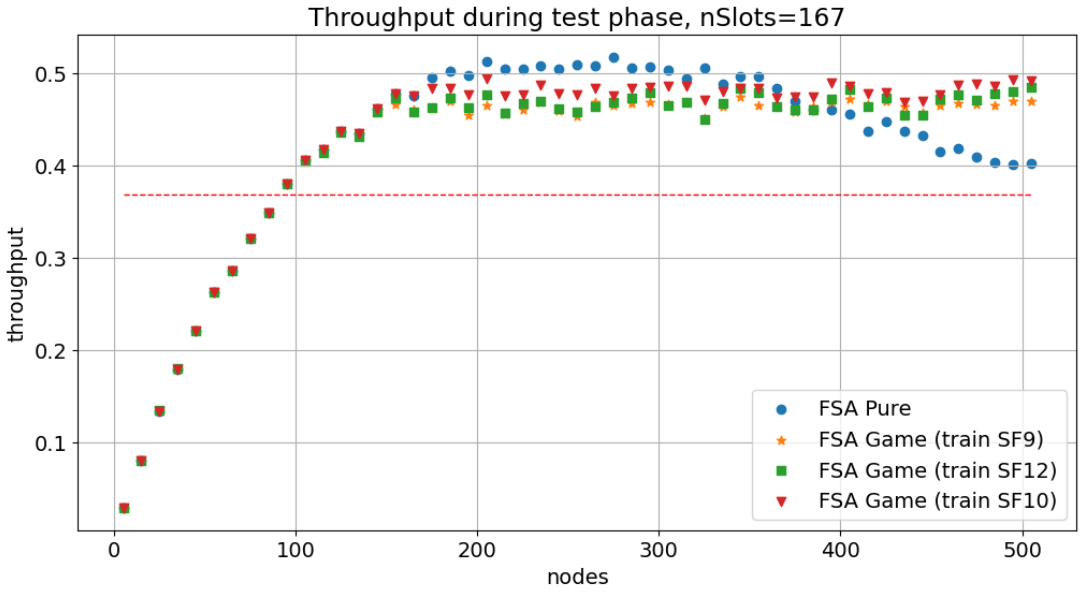


Figure 3.5: Throughput comparison using estimations from Fig. 3.4

FLoRaSat. Indeed, a collision can still result in successful frame decoding. The pure FSA protocol achieves maximum throughput between 200 and 300 nodes, slightly higher than the scenarios employing SAG, but FSA's throughput decreases steadily after that, validating the findings in [40]. Instead, with the SAG access control, the throughput peaks when the number of nodes equals the number of slots, oscillating around these values after that. The highest average throughput is observed when using the OCI estimations obtained with SF10 (48.1%), which also has the lowest RSME, as it was the parameter for which L-OCI was trained. However, the difference in throughput concerning SF9 (46.5%) and SF12 (46.8%) scenarios is minimal. To wrap up, the throughput results suggest using SF10 or SF11 to provide the best performance of the trained L-OCI model.

Error and Energy Trade-off

This experiment evaluates the effectiveness of the MOP heuristic for optimizing energy consumption and estimation error in LoRa networks. The wasted power and RMSE are jointly analyzed in Fig. 3.6, where the former is calculated as the power spent by a node in non-successful transmissions. A parameter selection campaign was conducted for 100, 500, 1000, and 1500-node network sizes. Results show that wasted energy and estimation error increase with the number of nodes in the network. Moreover, the most energy-efficient solutions were obtained using $SF = 9$ and $BW = 125$ for all cases. For instance, the Pareto curve for a network of 500 nodes suggests that a parameter set with $SF = 9$ and $BW = 125$ can achieve an estimation error of $RSME = 5$ and a wasted energy per node of $16mW$. To further reduce the error, switching to $SF = 11$ and $BW = 250$ is required, resulting in a reduced error of $RSME = 2.5$ but increased wasted energy to $27mW$ per node (see red arrow in Fig. 3.6). The results demonstrate the effectiveness of the MOP heuristic for optimizing energy utilization and estimation error in LoRa networks. Furthermore, in light of the observations in the previous experiment, the marginal improvement in error might not be justified in terms of throughput due to the significant increase in energy consumption.

Thèse accessible à l'adresse : https://theses.insa-lyon.fr/publication/2026ISAL0011/these.pdf © [D. Maldonado Muñoz], [2026], INSA Lyon, tous droits réservés

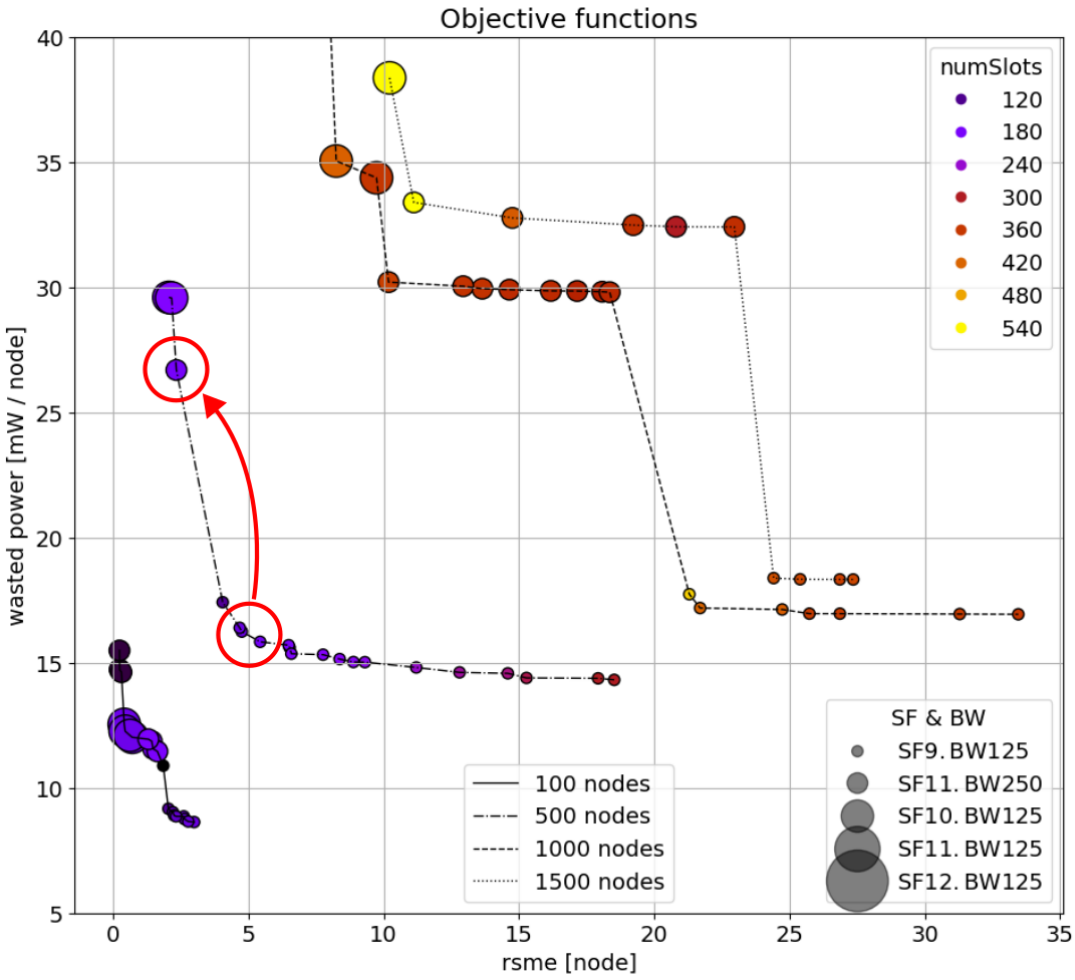


Figure 3.6: Pareto curves for different network sizes obtained from MOP

3.3.4 Conlusion

An extensive simulation campaign showed that L-OCI maintains low error estimations and power efficiency, even in scenarios with a high packet loss rate. Also, L-OCI proved insensitive to $SF = 10$ and $SF = 11$ regarding RSME and throughput, suggesting a single estimator can fit both use cases. However, in resource-full satellites, multiple estimators could co-exist for optimal performance. Furthermore, our analysis showed that $SF = 9$ and $BW = 125kHz$ are appealing candidates for improving energy efficiency if the link budget can be closed under such parameters.

3.4 Constellation L-OCI

Constellation L-OCI (CL-OCI) aims to overcome the limitations of previous OCI techniques and adapt them to a realistic constellation environment, considering ground track shifts. Additionally, this adaptation seeks to extend L-OCI's estimation limit capacity beyond 500 nodes with the implemented set of parameters, while maintaining low hardware and cost requirements.

The general concept of this mechanism is to transmit a G index to the ground nodes via the downlink beacon. Afterward, the nodes compete during the beacon period with a probability of $1/G$. The estimation process is similar to that used in L-OCI: each satellite performs its calculations and

Thèse accessible à l'adresse : https://theses.insa-lyon.fr/publication/2026ISAL0011/these.pdf © [D. Maldonado Muñoz], [2026], INSA Lyon, tous droits réservés

then transmits the results to a ground station located on the Earth's surface.

On the ground station side, the coordinates of the satellites at the moment of transmitting the downlink beacon are known. These coordinates are used to calculate the projection of each satellite's coverage on the ground and the portion of this coverage that overlaps with the reference satellite. The reference satellite is positioned at the center of the node deployment area.

By determining the degree of overlap, estimating the portion of the node cluster covered at any given time is possible. In this manner, each satellite estimates the entire cluster by observing a subset of nodes during the contention process. The size of this subset depends on the known G and the calculated overlap with the reference. The average of these individual satellite estimates provides the constellation-wide estimation.

3.4.1 Scenario Model

Topology The studied scenario involves a Discontinuous LEO satellite constellation [63] (DisLEO) comprising Q CubeSat satellites in a Low Earth Orbit (LEO), serving as gateways to terrestrial nodes under the DtS-IoT scheme at an altitude of approximately 600 kilometers and an orbital inclination of 98 degrees. CubeSats are assumed to possess attitude and orbit control designed for small satellites [64, 65].

All satellites are deployed in the same orbital plane. Most large satellite constellations operate in multiple orbit planes to ensure global coverage. However, smaller constellations may operate in a single orbital plane, depending on their specific mission requirements. Indeed, our estimator is specifically designed for low-cost DtS-IoT CubeSat applications operating in a single orbital plane, simplifying mission design and reducing costs for smaller constellations. For example, both systems, Astrocast [66] and Fossa [67] are small DtS-IoT constellations that initially operate in a single plane and later expand into multiple planes if needed. Future work considers multiple orbit planes and larger satellite constellations.

A cluster of N nodes is deployed uniformly in an arbitrary circular region on the Earth's surface, matching the satellites' coverage area according to the parameters $w = 167$, $SF = 10$, $BW = 125$, $BCN = 91$, which gives a range of approximately 1100 km [5]. The first satellite in the constellation is positioned above the cluster, so its ground projection coincides with the center of the node deployment cluster. The satellites are spaced with a mean anomaly separation of -36 degrees in FLoRaSat. Whether nodes are static or mobile is not essential; nodes are assumed to stay inside the deployment region, and their mobility inside of it doesn't affect CL-OCI's operation.

Operation The Q satellites periodically broadcast a beacon, marking a Beacon Period's beginning. Nodes that successfully decode this beacon randomly choose a slot with uniform probability. Given the DisLEO constellation, satellites only receive transmissions from nodes that received their corresponding beacon. As in [5], it is assumed that the first satellite in the constellation starts with its coverage area centered on the cluster. The terrestrial nodes activate their radios only when a satellite is visible and transmit a single dummy message during each Beacon Window in which they contend.

Thèse accessible à l'adresse : https://theses.insa-lyon.fr/publication/2026ISAL0011/these.pdf © [D. Maldonado Muñoz], [2026], INSA Lyon, tous droits réservés

3.4.2 Grouping Approach

CL-OCI involves dividing the cluster of nodes into G groups, so each satellite in the constellation must estimate at most N/G nodes. The division into groups is achieved by transmitting the index G in the beacon of the first satellite, after which the nodes calculate g_n, an integer between 1 and G, upon receiving the beacon. Once g_n is calculated, node n will contend in the Beacon Window if $g_n = 1$, otherwise in the g_n-th Beacon Window, and then successively in the $g_n + G$-th. It is common in recent literature to assume the IoT devices use a predictor of the satellite orbit [68]. Given techniques for estimating visibility time [59, 69, 70] and the nodes' knowledge of the satellites' trajectory, each node should only turn on its radio when appropriate.

This grouping approach reduces the number of transmissions and, thus, the related energy costs. The energy implications are as follows:

Energy Model The subsystem of the ground nodes that consumes the most energy is the radio [71]. The energy consumed by the radio in the process of a complete pass of the constellation is defined as:

$$E_{\text{pass}} = \sum_{i=1}^{Q} E_i^{\text{sat}} + \sum_{n=1}^{N} E_n^{\text{node}}, \tag{3.3}$$

where E_{pass} is the total energy consumed in the interaction between nodes and the gateway, defined as the sum of the energy consumed by each satellite E_i^{sat} and each node E_n^{node}. The subsequent downlink of the received LoRa frames from each satellite to the ground station is ignored.

The energy consumed by each satellite and node during this estimation phase is defined as follows:

$$\begin{aligned} E_i^{\text{sat}} &= P_{\text{tx}}^{\text{sat}}\, T_{BP} + P_{\text{rx}}^{\text{sat}}\, T_W, \\ E_n^{\text{node}} &= \tfrac{Q}{G}\left(P_{\text{rx}}^{\text{node}}\, T_{\text{BP}} + P_{\text{tx}}^{\text{node}}\, T_M\right), \end{aligned} \tag{3.4}$$

where $P_{\text{tx}}^{\text{sat}}$ ($P_{\text{tx}}^{\text{node}}$) and $P_{\text{rx}}^{\text{sat}}$ ($P_{\text{rx}}^{\text{node}}$) are the power consumed on a satellite (node) during transmission and reception, respectively; T_{BP} is the duration of the LoRa packet the satellite sent to initiate the Beacon Period, T_W is the duration of the Beacon Window contention period and T_M is the duration of a node's transmission message. Finally, $\frac{Q}{G}$ determines the probability of a node receiving the Beacon from one of the Q satellites and consequently sending a message to it. So, the energy consumption decreases with an increase in G for a constant Q. However, G cannot be increased indefinitely. Determining an optimal G value and the trade-off with estimation accuracy is discussed in Section 3.4.5.

3.4.3 Ground Track Shift

To address the ground shift perceived by each satellite, we use the portion of the cluster under its coverage when it transmits a beacon. The first satellite of the constellation is centered over the cluster, as shown in Fig. 3.7, and its coordinates are taken as a reference.

Each satellite passes with its ground track shifted by a certain number of kilometers, covering only a portion of what the reference satellite covered. We define this portion as $O_{i,b}$, the percentage overlap of the satellite coverage projection i when transmitting the beacon b. Given that the Beacon

Thèse accessible à l'adresse : https://theses.insa-lyon.fr/publication/2026ISAL0011/these.pdf © [D. Maldonado Muñoz], [2026], INSA Lyon, tous droits réservés



Figure 3.7: FLoRaSat UI of a simulated scenario with 50 nodes

Periods, during which satellites perform their estimations, are finite and sequential, $O_{i,b}$ is expressed as O_b. Each satellite is responsible for initiating a specific subset of these beacon periods, meaning that the total set of beacon periods during a constellation pass, B, is distributed among all satellites in the constellation. For example, satellite 1 may handle beacon periods 1 through 4, while satellite 2 is responsible for beacon periods 5 through 7, continuing in this manner until beacon B. There is a maximum distance between satellites beyond which the ground track shift is significant enough for the overlap to be zero, which limits the number of satellites Q worth considering during the simulation.

Each satellite performs an estimation Θ_b, corresponding to the OCI estimation of a satellite during the b-th beacon period. Then, considering the overlap proportion, the estimation is weighted as follows:

$$\phi_b = \frac{\Theta_b}{O_b} G. \tag{3.5}$$

Finally, the estimates from different satellites are sent to a ground station, which proceeds to calculate the average to produce the estimate of the whole constellation:

$$\Phi = \sum_{b=1}^{B} \frac{\phi_b}{B}, \tag{3.6}$$

where B indicates the number of estimations made by the constellation.

3.4.4 Performance Metrics

The following performance metrics evaluate CL-OCI performance for a satellite constellation environment.

RMSE: A sufficiently large number of iterations, K, of the experiments executed to achieve a 95% confidence interval. The Root Mean-Squared Error is calculated as given in Eq. 3.2.

Energy cost: The energy cost to obtain the estimate is calculated as the sum of attempted transmissions during Beacon Windows periods and multiplied by the power consumption of a transmission equal to the maximum allowed according to Semtech's specifications: 25.12 mW [62]. Results are normalized and expressed as energy cost in milliwatts per node.

Thèse accessible à l'adresse : https://theses.insa-lyon.fr/publication/2026ISAL0011/these.pdf © [D. Maldonado Muñoz], [2026], INSA Lyon, tous droits réservés

3.4.5 Evaluation

We evaluate CL-OCI's performance by recreating a DtS-IoT scenario where a cluster of nodes is deployed over the Brazil, Bolivia, and Paraguay regions, as shown in Fig. 3.7. A constellation of nanosatellites orbits over this region, transmitting beacons periodically and receiving node transmissions during the uplink period.

The FLoRaSat [6] simulator is used for simulations. This event-driven open-source end-to-end simulation tool leverages OMNeT++ and is specialized in simulating DtS-IoT networks. The experiments contemplate varying values of the network size N and the group division index G. N varies, starting at 500 nodes and growing up to 1000 with steps of 100. The G index starts from G equal to 2 up to 10 with steps of 2. For each configuration, 21 iterations are performed. Given the orbital parameters of the simulations, starting from the sixth satellite, the ground track deviates because it cannot estimate the node cluster. For this reason, $Q = 5$ is considered for all experiments.

As the ground track deviates and the percentage of overlap with the reference satellite coverage area decreases, the estimates' error becomes greater. Given this, the results are shown considering an overlap threshold that filters the estimates of satellites presenting an overlap percentage lower than the threshold when transmitting their beacons.

Fig. 3.8 shows the experiments' average RMSE and energy cost results. Results for $G = 1$ are those from the single-satellite L-OCI, which are shown to contrast the adaptation's contribution to the multi-satellite case in CL-OCI. As seen in the figure, increasing G reduces the energy cost proportionally to G, $G = 10$ having the lowest energy cost in milliwatts per node.

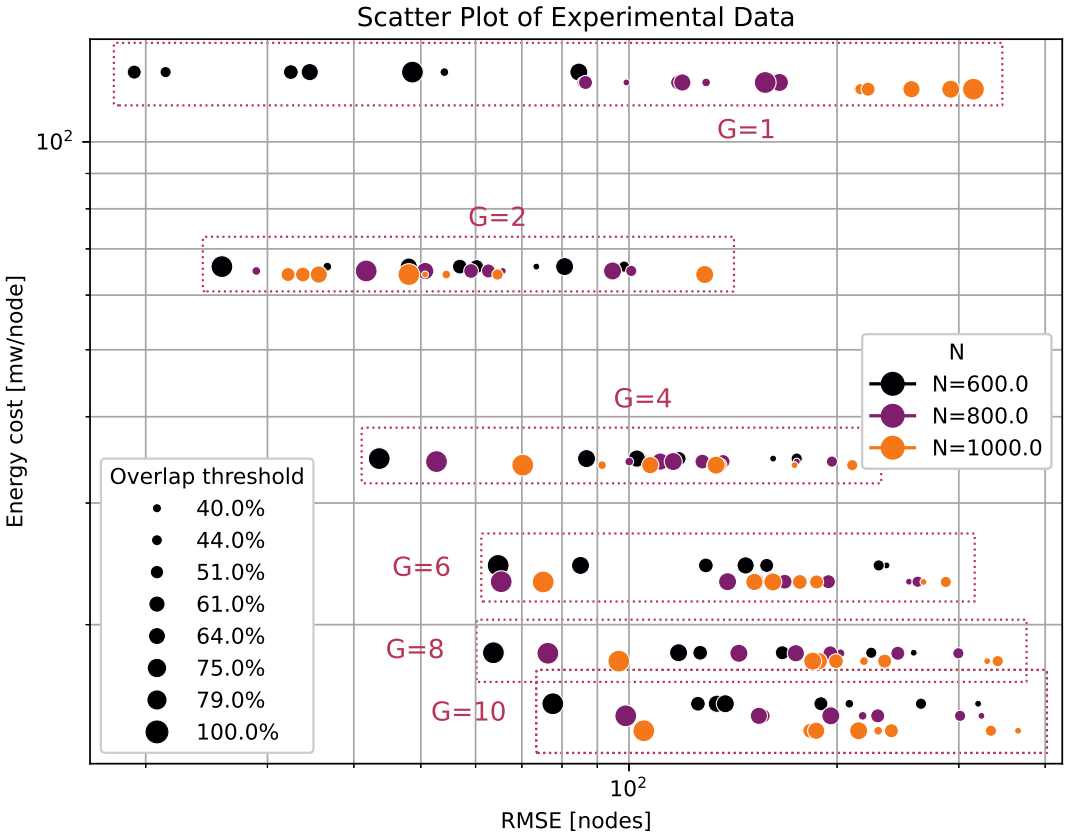


Figure 3.8: RMSE vs. Energy cost of estimates for different values of G, N, and overlapping threshold

This is a direct benefit of requiring lower node participation in terms of transmissions to calculate

Thèse accessible à l'adresse : https://theses.insa-lyon.fr/publication/2026ISAL0011/these.pdf © [D. Maldonado Muñoz], [2026], INSA Lyon, tous droits réservés

an estimate. An increase in cluster size N leads to higher congestion, which, in turn, results in an increased RMSE for the estimation. In general, the RMSE decreases for the different values of G in comparison to $G = 1$ if the threshold is set to 100%, i.e., only the estimate of the reference satellite is integrated into the OCI estimate as done in [5]. This latter witnesses the scalability of CL-OCI with this new mechanism. $G = 6$, $G = 8$, and $G = 10$ show slightly worse RMSE for $N = 600$ in comparison to $G = 1$. Increasing G increases the RMSE progressively. This is because the multiplications to consider the overlap in 3.5 amplify the associated error, which makes larger values of G more sensitive to estimation errors. The overlap threshold shows that considering estimates from more satellites in the global estimate benefits $G = 1$ and $G = 2$ up to a certain point from which the error increases. However, for values of G superior to or equal to 4, the RMSE increases when estimates with a lower overlap percentage are integrated. This is because the estimation error is high and amplified by the multiplication of equation 3.5. Given these results, calculating the OCI estimation from separate satellite estimates provides better accuracy than integrating the estimates from multiple satellites for G values of 4 or higher.

These results show that the more pronounced the energy constraints, the more suitable the utilization of a higher G value. In [40], the MAC protocol Slotted Aloha Game (SA GAME) was tested using OCI estimates as input, demonstrating that errors up to 300 nodes in terms of RMSE did not significantly affect the throughput of SA GAME. This implies that increasing G results in a lower energy cost while maintaining adequate RMSE values.

3.4.6 Conlusion

By addressing the non-uniformity and ground track shifts inherent in satellite constellations, CL-OCI enhanced the scalability and accuracy. Our approach effectively segments terrestrial nodes into G groups, allowing each satellite to estimate a fraction of the total network, thereby reducing energy consumption and maintaining accuracy.

Simulation results demonstrated that increasing the group index, G, leads to proportional energy savings while achieving acceptable RMSE values, which are critical for integration with MAC protocols like SA Game. Specifically, CL-OCI doubles the number of nodes it can accurately estimate and reduces the energy wasted due to collided transmissions by seven-fold compared to single-satellite L-OCI. The results validate the scalability and efficiency of CL-OCI, making it a viable solution for large-scale DtS-IoT deployments using satellite constellations.

Thèse accessible à l'adresse : https://theses.insa-lyon.fr/publication/2026ISAL0011/these.pdf © [D. Maldonado Muñoz], [2026], INSA Lyon, tous droits réservés

Chapter 4

Scalability

This chapter contributes by expanding LR-FHSS scalability in two dimensions.

On the one hand, we propose improving the FHS construction to enhance device-to-gateway extraction rates in view of massive connectivity. In particular, we propose leveraging Wide-Gap sequences' existing properties while making them applicable to LR-FHSS requirements. This property emerges as a superior candidate, outclassing current LR-FHSS driver implementations in specific scenarios. In particular, we investigate the parameter design and settings of Wide-Gap sequences, so as to make them fit practical LR-FHSS requirements.

On the other hand, we introduce two pioneering strategies for demodulator allocation designed to amplify the scalability of LR-FHSS-based networks further. At the heart of these strategies is the efficient use of redundancies inherent in the payload's convolutional encoding and decoding processes. The first, termed "Early-Decode", frees up demodulators once they've gathered sufficient convolutional blocks for frame decoding. The second, "Early-Drop", proactively dismisses a packet if a certain number of its blocks fail, liberating the processor for subsequent demodulation.

4.1 Introduction to Frequency Hopping Sequences

Frequency Hopping Sequences (FHS) defines the sequence and timing of frequency shifts during a transmission. Often, these sequences are generated from mathematical algorithms or pseudo-random number generators. The key feature of these sequences is their unpredictability and non-repetitive nature, ensuring that potential adversaries find it challenging to intercept or jam the transmission [72]. Moreover, FHS-based modulations exhibit significant resilience to intense interference scenarios, typical in satellite communications, due to the expansive areas they cover on the Earth's surface.

In the following, the set of accessible frequency channels in an FHSS system is denoted $\mathcal{F} = \{f_0, f_1, \cdots, f_{\ell-1}\}$. A FHS X is a periodic sequence $\{x_i, i = 0 \dots L\}$ of frequencies within $\mathcal{F}$. In the example of Fig. 2.4, $\ell = 280$, and the period is $L = 35$.

Hamming Correlation is a measure of the similarity or correlation between two FHSs [73]. In our setting, it quantifies the number of collisions between two FHS potentially shifted in time.

Thèse accessible à l'adresse : https://theses.insa-lyon.fr/publication/2026ISAL0011/these.pdf © [D. Maldonado Muñoz], [2026], INSA Lyon, tous droits réservés

Let $X = \{x_i\}$ and $Y = \{y_j\}$ be two FHS, their Hamming Correlation at a time offset τ is:

$$H(X, Y; \tau) = \sum_{i=0}^{L-1} h(x_i, y_{i+\tau \pmod L}), \tag{4.1}$$

where $h = \mathbb{1}_{\{f_i = f_j\}}$, with $f_i, f_j \in \mathcal{F}$.

4.1.1 Wide-gap FHS

The smallest gap or distance e between successive frequencies of X is delineated as:

$$e = \min_{0 \le i \le L-2} \{|x_{i+1} - x_i|, |x_{L-1} - x_0|\}. \tag{4.2}$$

In situations where $e > 0$, there are no two successive frequencies that are similar, and sequence X is classified as a wide-gap FHS (WGFHS) [74, 75]. For LR-FHSS, the concept of grids is a means to achieve such a wide gap property.

4.2 Construction Method of LR-FHSS Sequences with Semtech's Driver

The construction technique for FHS tailored for LR-FHSS devices, as found in an official LoRa repository on Github [76], diverges from the method detailed in [32] or [77]. Rather than relying on a hash function or a pseudo-random function, it harnesses the potential of m-sequences [78].

Table 4.1 provides an exhaustive breakdown of the LR-FHSS sequence generator's configurations assumed in the driver. Five distinct configurations arise based on the number of grids they support. Table 1 from [34] lists the available LR-FHSS Channel Bandwidths, indicating the number of grids each channel supports. Several grids between 10 and 47 fall in case 1 from Table 4.1, 60 and 62 grids correspond to cases 2, 86 and 99 grids to case 3, 185 and 198 grids to case 4, and 390 and 403 grids to case 5. It is worth noting that for cases 1 and 2, a 6-register Linear Feedback Shift Register (LFSR) is employed. Yet, with this configuration, only six primitive polynomials exist, meaning the FHS families produced for LR-FHSS devices in these scenarios are limited to 384 sequences. The details on spreading sequences and, in particular, LFSR and m-sequences fall outisde of the scope of this chapter. The reader is invited to consult Chapter 2 from [72] additional material.

Table 4.1: LR-FHSS FHS Construction Parameters

case	1	2	3	4	5
initial state	6	56	6		
LFSR size	6		7	8	9
polynomial bits	3		2	1	0
polynomial set	{33,45,48, 51,54,57}		{65,68, 71,72}	{142,149}	{264}
seed bits	6		7	8	9
total seeds	64		128	256	512
FHS family size	384		512		

Figure 4.1 depicts the construction mechanisms of LR-FHSS sequences. The m-sequence generator block, positioned at the top of the figure, represents an LFSR comprising m registers.

Thèse accessible à l'adresse : https://theses.insa-lyon.fr/publication/2026ISAL0011/these.pdf © [D. Maldonado Muñoz], [2026], INSA Lyon, tous droits réservés

The primitive polynomial (*p polynomial*), instrumental in the m-sequence's creation, is encoded within the x most significant bits of the 9-bit Hopping Sequence field conveyed in the Header (*hop sequence id*), where x can take values from the set $\{0, 1, 2, 3\}$. The modulation parameters inform the determination of the initial state. At the bottom, a constant *xoring* seed is coded into the remaining $y = 9 - x$ least significant bits of the 9-bit Hopping Sequence field. The LR-FHSS sequence is derived by performing a bit-wise exclusive OR (often referred to as *xoring*, synonymous with modulo two addition) between each component of the generated m-sequence and the xoring seed. The sequence's length is bounded by the necessary hops to encapsulate the payload data and header replicas. Furthermore, if the resulting values after the operation surpass the count of supported grids in a given scenario, they are omitted.

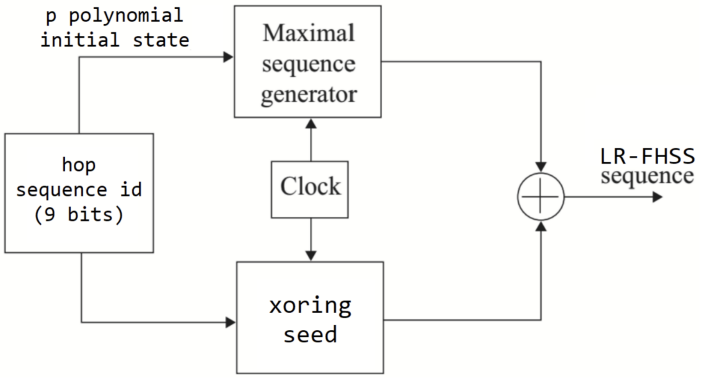


Figure 4.1: Early Drop mechanism illustration for a 13-fragment payload configuration

This selective process trims down the LR-FHSS sequence's length from the original m-sequence length (i.e., $2^m - 1$) to the exact count of the grids. As a result, the *driver* family is composed of the $M = 384$ possible sequences that can be generated by the LR-FHSS Driver method for data rates DR8 and DR9 (case 1 from Table 4.1), all of length $L = 31$.

4.3 Proposed general framework

The proposed framework, illustrated in Fig. 4.2, integrates two key contributions to enhance the scalability of LR-FHSS. The first component, represented by the red block, introduces advanced Frequency Hopping Sequence (FHS) designs leveraging Wide-Gap sequences to optimize collision resilience. The second component, shown in the blue block, incorporates novel demodulator allocation strategies—"Early-Decode" and "Early-Drop"—to maximize decoding efficiency by dynamically managing gateway resources. Together, these innovations form a unified approach to addressing the challenges of massive IoT connectivity in satellite-based LR-FHSS networks.

4.3.1 FHS Families for LR-FHSS

This section delves into constructing FHS families tailored for the LR-FHSS protocol, namely the red block of Fig. 4.2. The families constructed can be categorized based on the design principles derived from Lempel-Greenberger and Li-Fan.

Thèse accessible à l'adresse : https://theses.insa-lyon.fr/publication/2026ISAL0011/these.pdf © [D. Maldonado Muñoz], [2026], INSA Lyon, tous droits réservés

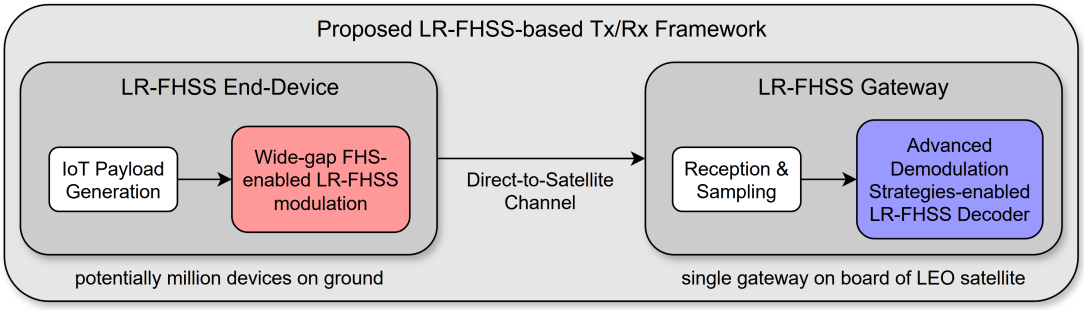


Figure 4.2: Unified framework architecture for enhancing LR-FHSS scalability

Lempel-Greenberger FHS Families

Lempel and Greenberger [79] proposed FHS construction techniques based on m-sequences that optimize the Hamming Correlation for generating optimal FHS families. The Lempel-Greenberger FHS construction involves selecting parameters $\{p, k, n\}$ and a primitive polynomial for an LFSR of a given order, generating an m-sequence that serves as the base sequence to build optimal sequences. This method enables the generation of $M = p^k$ sequences of length $q = p^n - 1$.

Two Lempel-Greenberger FHS families were built. The first one has the construction parameters $\{p = 2, k = 5, n = 5\}$ with the primitive polynomial 0x12 in hexadecimal. The resulting FHS family named **lem-green** has 32 sequences of length 31.

A second family is built with the same previous parameters but using the primitive polynomial 0x12. Then, merging the previous families generates a second Lempel-Greenberger FHS family named **lem-green-2x**. The **lem-green-2x** FHS family has 64 sequences of length 31.

Li-Fan FHS Families

In [74] the authors propose a new type of Wide-gap FHS. The authors then provide a construction method for such sequences in [75], which we name here Li-Fan FHS. The Li-Fan FHS construction provides families based on the methods of period 2ℓ or 3ℓ. Depending on the chosen parameters, families might need further splitting or merging to attain desired frequency values and lengths. For all of the following Li-Fan, the frequency values above 280 are discarded and the minimum gap is adjusted to 8.

The **li-fan-2l** Family is based on 2ℓ-method with parameters $\ell = 281, d = 8$. A single FHS of length $2\ell = 562$, further split into 18 sequences of length 31. We repeat this process with the parameters $\ell = 277$, $\ell = 283$ and $\ell = 287$, all with $d = 8$. Then we merge these 4 families to form the **li-fan-2l-4x** Family.

The **li-fan-3l** Family is similar to the **li-fan-2l** Family but it uses the 3ℓ method. Lastly, **li-fan-3l-4x** Family construction is analogous to the **li-fan-2l-4x** Family.

We tailored FHS families optimized for the LR-FHSS protocol by employing the above design principles and methods. These are crucial as they lay the foundation for enhancing the decoding proficiency of LoRa demodulators, a significant step forward for satellite-based communications.

Thèse accessible à l'adresse : https://theses.insa-lyon.fr/publication/2026ISAL0011/these.pdf © [D. Maldonado Muñoz], [2026], INSA Lyon, tous droits réservés

4.3.2 Early Drop and Early Decode Mechanisms for LR-FHSS

We next describe our second proposed component of our general framework, namely the blue block of Fig. 4.2.

The LR-FHSS satellite gateway's primary functionality can be conceptualized as follows:

- *Frame Reception*: Upon LoRa satellite gateway's reception of a transmission from a ground IoT device, an available demodulator springs into action. Its core responsibilities encompass collision monitoring and the capture of headers and any fragmented data in the transmission.
- *Frame Demodulation*: After completing the reception process of all fragments, the actual demodulation occurs. A packet is successfully decoded if at least one header replica and a minimum number of necessary fragments are free from collisions.
- *Demodulator Availability*: When no demodulators are on standby or accessible, the transmission is sidestepped. As a result, the corresponding packets are discarded.

This structured approach streamlines the gateway's operation, ensuring efficiency and minimal data loss.

Given the payload's encoding structure, it's possible to decode it successfully, even if only a portion of the fragments are available. This suggests an opportunity to utilize each demodulator's capability more efficiently. Towards this end, we propose adopting the subsequent smart LoRa gateway mechanisms.

Early Drop

The Early Drop demodulation strategy is specifically designed to optimize the efficiency of the satellite gateway's demodulation resources. This mechanism comes into play when the demodulator determines that the minimum number of fragments required for successful packet decoding cannot be achieved. Under such circumstances, the demodulator pre-emptively terminates the packet's reception.

To elucidate the concept, consider a payload consisting of 13 fragments. Depending on the encoding scheme:

- CR1/3 (denoted CR1): A minimum of 5 fragments is essential for successful decoding.
- CR2/3 (denoted CR2): 9 fragments are required.

Figure 4.3 delineates these configurations, where each fragment corresponds to a frequency channel (indicated with numbers). Red highlights collisions (unsuccessfully received fragments), while green signifies successfully received fragments.

In a CR1 scenario, after recognizing the 9th collision, it becomes clear that only a maximum of 4 successful fragments can be accumulated, which is inadequate for decoding. Recognizing this, the demodulator can promptly categorize the payload as 'collided' and free itself for other tasks. Analogously, for CR2, the demodulator would adopt a similar course of action after the 5th collision. The steps involved in this process are detailed in Algorithm 1.

Thèse accessible à l'adresse : https://theses.insa-lyon.fr/publication/2026ISAL0011/these.pdf © [D. Maldonado Muñoz], [2026], INSA Lyon, tous droits réservés

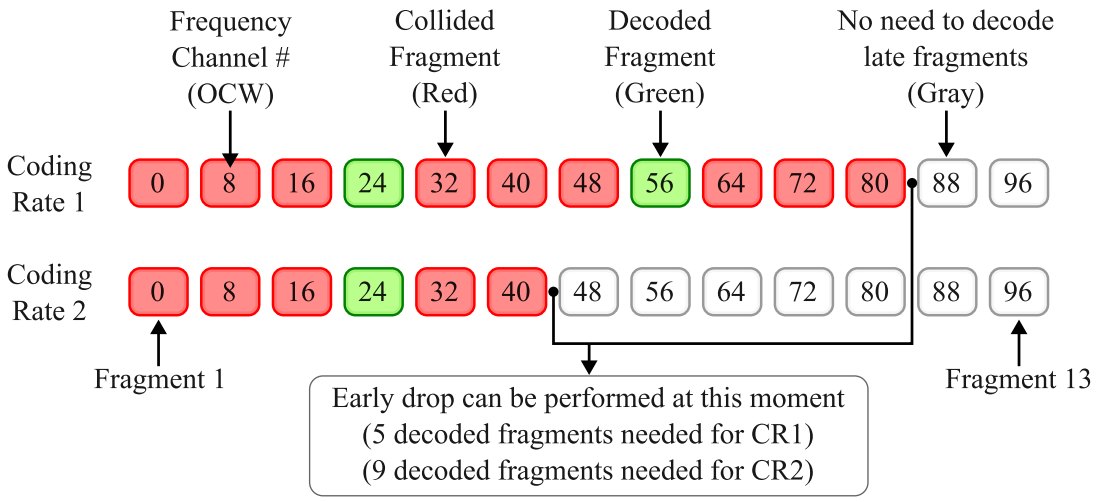


Figure 4.3: Early Drop mechanism illustration for a 13-fragment payload configuration

Algorithm 1: Early Drop Algorithm

```
totalFragments ← 31
threshold ← ceil(totalFragments / 3)
if CR is 2/3 then
    threshold ← ceil(2 · totalFragments / 3)
end
collidedFragments ← 0
for fragment in payload do
    if fragment is collided then
        collidedFragments ← collidedFragments + 1
    end
    if collidedFragments > (totalFragments-threshold) then
        Return
    end
end
```

Early Decode

This mechanism enables the demodulator to commence decoding once it has collected the minimum number of fragments required for successful payload decoding. This strategy lets the demodulator quickly process each packet, reducing its LoRa gateway occupancy and enhancing the overall throughput and efficiency.

Using the same fragment configurations detailed above:

- CR1/3: The decoding process initiates immediately after the successful reception of the 5th fragment.
- CR2/3: Decoding begins after the successful reception of the 9th fragment.

Fig. 4.4 showcases these configurations with various fragment collision statuses. Once the required fragments are received successfully, the demodulator has adequate data to decode the payload. It can then ready itself for the reception of subsequent packets. Algorithm 2 offers an

Thèse accessible à l'adresse : https://theses.insa-lyon.fr/publication/2026ISAL0011/these.pdf © [D. Maldonado Muñoz], [2026], INSA Lyon, tous droits réservés

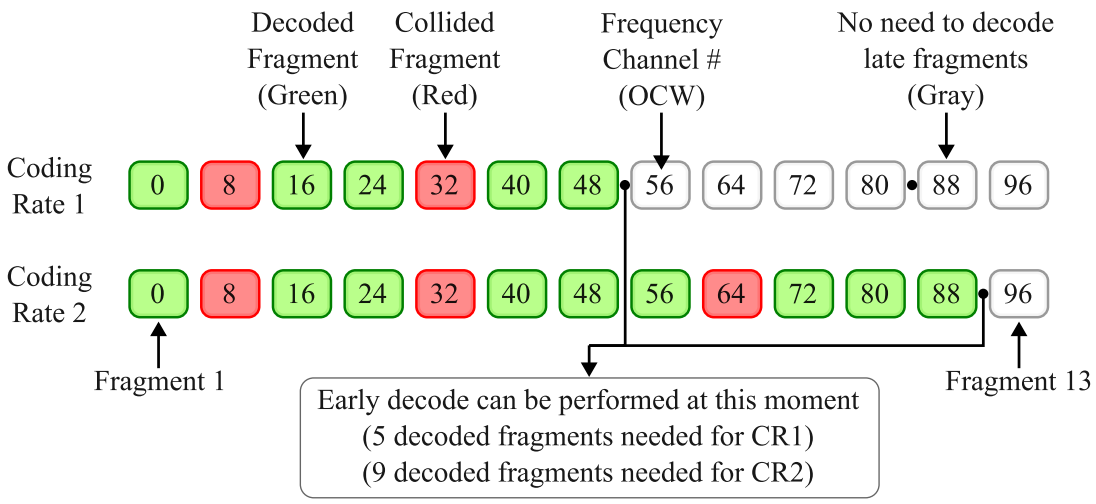


Figure 4.4: Early Decode mechanism representation for a 13-fragment payload configuration

in-depth procedural description of the Early Decode mechanism.

Algorithm 2: Early Decode Algorithm

```
totalFragments ← 31 threshold ← ceil(totalFragments / 3)
if CR is 2/3 then
    threshold ← ceil(2 · totalFragments / 3)
end
successfulFragments ← 0 for fragment in payload do
    if fragment is successful then
        successfulFragments ← successfulFragments + 1
    end
    if successfulFragments ≥ threshold then
        Return
    end
end
```

4.4 Results and Analysis

4.4.1 Simulation Settings and Parameters

We constructed a simplified but representative simulation model to assess the performance implications of various FHS families in an LR-FHSS network. This model encapsulates fragments' and headers' time-slotted communication dynamics within finite frequency channels.

Simulation Model Overview

Each fragment in the simulation persists for g time slots, where g denotes the model's granularity. Correspondingly, headers last for $\lceil 233g/102.4 \rceil$ slots. Throughout the simulation duration, N nodes transmit a packet of fixed length L, broken down into fragments. These transmissions are initiated

Thèse accessible à l'adresse : https://theses.insa-lyon.fr/publication/2026ISAL0011/these.pdf © [D. Maldonado Muñoz], [2026], INSA Lyon, tous droits réservés

at random time slots. The choice of an FHS for each node is randomized from the available FHS family. The gateway employed in the model is equipped with p demodulators, which are essential for decoding the packets.

A collision is deemed to have occurred if two or more fragments or headers share at least one-time slot on an identical frequency channel. Payloads receive a 'collided' designation if their collided fragments breach a certain threshold, contingent on the CR utilized for encoding. Additionally, the *Header Tolerance* parameter determines the header's collision tolerance, defining the maximum collided slots permissible for a successful decode.

Our model leverages the free space channel model, which is especially fitting for LR-FHSS in satellite communications due to outer space's open and unobstructed nature. Contrary to the cluttered terrestrial environments, space provides a clear signal path, validating the model's straightforwardness as an effective means of characterizing signal interactions between satellites and terrestrial stations [80]. Such a channel becomes even more pertinent when factoring in the vast distances involved, which are not typically accounted for in standard urban and suburban IoT [81]. Furthermore, frequency-selective fading is negligible, given the narrow-band channels in LR-FHSS. While physical-layer impairments such as space radiation interference and multipath fading exist in LEO satellite IoT communications, their impact remains significantly lower than the dominant factors studied in this work, including sequence design and demodulator allocator.

Our simulator's codebase comprising the scenario configurations used in this section is publicly accessible on Github [82].

Early Header Drop

In our extended gateway model, we introduce the “Early Header Drop" feature to accurately portray an LR-FHSS gateway's operation. The importance of a header in packet communication cannot be overstated, as it carries the FHS information crucial for decoding the corresponding packet. Thus, if a header is not successfully decoded, the processor remains uninformed about the payload fragment sequence. In such situations, the gateway's logical course of action would be to release the demodulator, enabling it to track subsequent packets. The previous operation mode is how the LR-FHSS works in reality, so the benefit of including this feature in our simulation is to assess the potential of decoding headerless frames. This is the case when, hypothetically, the gateway receives the minimum number of fragments for a successful payload decoding.

While our research primarily focuses on assessing FHS performance within LR-FHSS networks, evaluating the “Early Header Drop" mechanism is largely excluded from most tests in Section 4.4. Still, the study of decoding payloads without their associated headers holds considerable potential and significance in LR-FHSS research, as noted in [35]. The “Early Header Drop" mechanism is executed after the reception of the last header. The “Early Header Drop" mechanism is no more than the decoder behaviour. An LR-FHSS decoder will only attempt to decode the payload data if it recovers at least one of the header replicas.

Simulation Configuration

The simulations were primed using the parameters outlined in Table 4.2, following the parameters for DR8 and DR9. In a gateway containing a single DSP and employing a channel spacing of 200 kHz, end devices can utilize a maximum of 7 OCW channels when employing a 136.70 kHz channel

Thèse accessible à l'adresse : https://theses.insa-lyon.fr/publication/2026ISAL0011/these.pdf © [D. Maldonado Muñoz], [2026], INSA Lyon, tous droits réservés

Table 4.2: Simulation configuration parameters

Parameter	Value
Number of repetitions	10
Simulation time	912 [slots]
OCW channels	7
OBW channels	280
Payload size	31 [fragments]
Fragment size	6 [slots]
Header size	14 [slots]

Table 4.3: Experimental study parameters

Parameter	Possible values
Coding Rate	CR1, CR2
FHS family	li-fan, driver
Number of demodulators	100, 1000
Early Decode	True, False
Early Drop	True, False
Early Header Drop	True, False
Header tolerance in slots	0, 4

bandwidth [32]. The payload size was set to 31 fragments, the maximum allowed for DR8. The fragment granularity is six time slots. Then, the maximum sequence duration arises during CR1/3 encoding (factoring in 3 header repetitions), culminating in a transmission span of 228 time-slots. In contrast, CR2/3-encoded transmissions wrap up in 214 time slots. We chose the simulation time as a fourfold duration of the longest sequence, totaling 912 time-slots.

The ratio of fragment-to-header durations in our simulation, which stands at 14 slots / 6 slots ≈ 2.33, is a close reflection of real-world values approximated at 233 ms / 102.4 ms ≈ 2.27.

Parameters Under Study

Table 4.3 delineates the parameters that underwent scrutiny in our research, each having two feasible values. Both the *Early Decode* and *Early Drop* features can be toggled on or off individually. Nevertheless, both are activated or deactivated simultaneously in our experiments. When *Early Header Drop* is turned on, the demodulator will drop the payload if no header is successfully received. For most experiments, the *Header Tolerance* is set to 0, meaning that a single collided time slot will result in a collided header. The last set of experiments is set to 4 time slots. Given that the payload fragment granularity requires six time-slots, a header will only tolerate collisions at the header reception's start, the end, or both. Our control parameter, the node count, is the transmission tally since each node transmits once within the simulation timeframe. Across different scenarios in the ensuing sections, the node (or transmission) count oscillates between 10 and 10,000. Given the results presented in section 4.4.2, the families of interest are the driver and the Li-Fan.

In their work, Boquet et al. [32] pointed out that the FHS generation method in LR-FHSS pivots around a hash function. Drawing inspiration from this methodology, we formulated a *hash* family for FHS based on the sha256 function. This curated FHS family encompasses $M = 384$ families, each

Thèse accessible à l'adresse : https://theses.insa-lyon.fr/publication/2026ISAL0011/these.pdf © [D. Maldonado Muñoz], [2026], INSA Lyon, tous droits réservés

with a length of $L = 31$.

4.4.2 Preliminary Frequency Hopping Sequence Analysis

Hamming Distance Analysis

The summary of the evaluated FHS families can be found in Table 4.4, where they are distinguished based on their size and the family's maximum Hamming Cross-Correlation $\bar{H}_{\max}(S, S)$.

Table 4.4: FHS family size and correlation characteristics comparison

family	size	$\bar{H}_{\max}(S, S)$
lem-green	32	0.939
lem-green-2x	64	2.108
li-fan-2l	18	0.480
li-fan-2l-4x	71	1.769
li-fan-3l	26	0.704
li-fan-3l-4x	107	1.566
hash	384	0.407
driver	384	0.416

The family maximum Hamming Correlation *(maxHC)* is illustrated in Figure 4.5 for both the *li-fan* and the *driver* families. The *maxHC* is the maximum Hamming Correlation value between any pair of sequences belonging to the FHS family. The correlation is assessed against increasing sequence lengths. For shorter sequences spanning up to 10 hops, the *li-fan* family exhibits a reduced correlation compared to the *driver* family. However, as the sequence length extends beyond this range, the *driver* family takes precedence in terms of lower correlation. It is noteworthy that even though the *li-fan* FHS is designed to yield an optimal sequence, this property is guaranteed only for the singular sequence generated. This explains the observed degradation in correlation performance when this primary sequence is partitioned into more minor sequences to constitute an LR-FHSS-compatible FHS family.

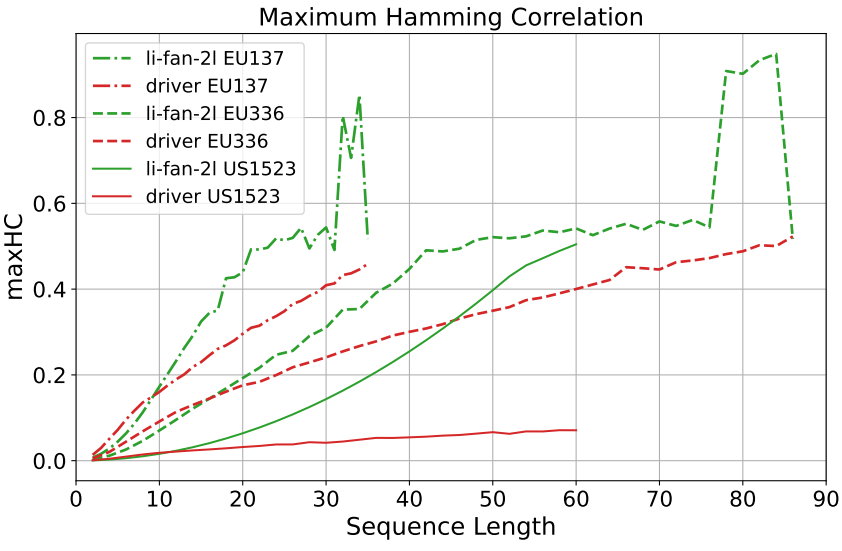


Figure 4.5: Maximum Hamming Correlation for different LR-FHSS FHS families (*li-fan* and *driver*)

Thèse accessible à l'adresse : https://theses.insa-lyon.fr/publication/2026ISAL0011/these.pdf © [D. Maldonado Muñoz], [2026], INSA Lyon, tous droits réservés

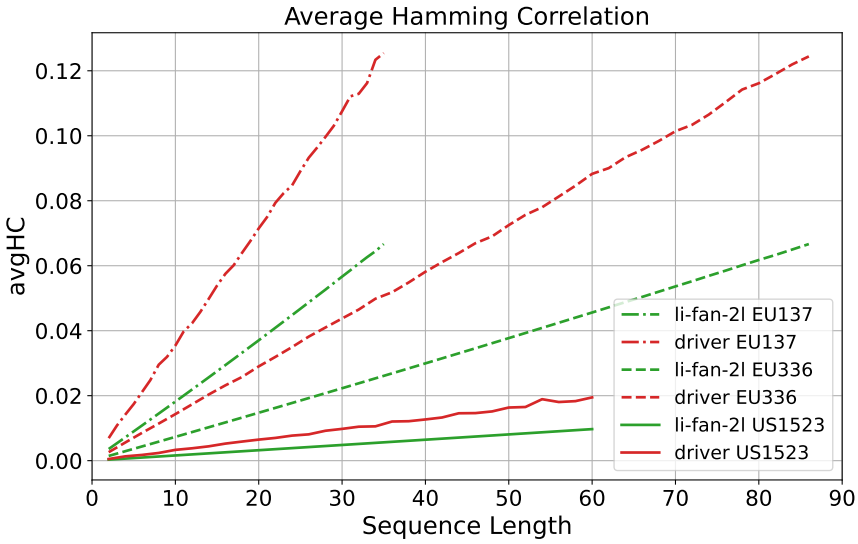


Figure 4.6: Average Hamming Correlation for different LR-FHSS FHS families (*li-fan* and *driver*)

Fig. 4.6 *(avgHC)* presents the family average Hamming Correlation $\bar{H}_{\text{avg}}(S, S)$. The *avgHC* is the mean Hamming Correlation value between all pairs of sequences belonging to the FHS family. This correlation is demonstrated for the families of both *driver* and *li-fan*, each formulated under three distinct configuration parameters. The three configurations are: 1. *EU137* with a maximum FHS length of 35 hops, 2. *EU336* with a maximum of 86 hops, and 3. *US1523* with 60 hops. Interestingly, across all these configurations, the *li-fan* FHS families consistently outperform their *driver* counterparts, showcasing superior correlation metrics.

Collision Rate Analysis

For an initial assessment, we used a preliminary test to study the collision rate at the payload level for different FHS families, as detailed in Table 4.4. This model is more basic than the one discussed above, encompassing fewer parameters. The collision rate is calculated as the number of collided slots from overlapping transmissions, i.e., with more than one fragment, divided by the total number of slots available. This design eliminated granularity, meaning each fragment was equivalent to a single time slot. Throughout the simulation, each node was responsible for transmitting a single payload of 31 fragments devoid of headers. The total time allocated for simulation was fourfold the time required for payload transmission, summing up to 124 time slots. Another distinguishing feature of this model was its lack of a decoding threshold for simultaneous receptions.

The core aim of this basic model was to analyze the FHS's correlation performance under conditions of multiple concurrent transmissions. Fig. 4.7 presents the relative collision rate, which is compared against the baseline established by the *driver* family. Here, the collision rate of each family is relative to the one achieved by the *driver* family for every transmission count. The *lem-green* family initially demonstrated a better performance than the *driver* family up to a certain number of transmissions but later faced a decline, especially for CR2. Observations highlighted that the *li-fan* families exhibited superior performance compared to the reference point after reaching a specific number of nodes. This trend was consistent for both Coding Rates.

Given the insights derived from this preliminary evaluation, we select the *li-fan-2l* family as the most performing in LR-FHSS. The upcoming comprehensive simulation campaigns will further investigate

Thèse accessible à l'adresse : https://theses.insa-lyon.fr/publication/2026ISAL0011/these.pdf © [D. Maldonado Muñoz], [2026], INSA Lyon, tous droits réservés

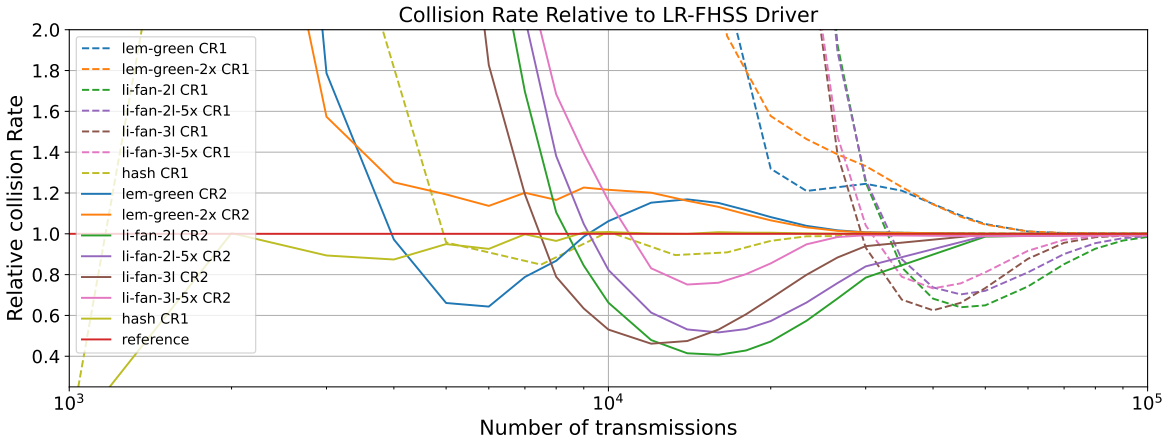


Figure 4.7: Relative collision rate comparison for different LR-FHSS FHS families against the reference Driver family, under conditions of no granularity, no headers, and unlimited decoding capacity

the combined performance of *li-fan-2l* with the proposed demodulation optimization techniques.

4.4.3 Early Drop and Early Decode Analysis

Building on our selection of the *li-fan* family, our analysis proceeds with the comprehensive model detailed in Section 4.2. Under this framework, a packet can experience one of three outcomes:

1. *Discarded*: When no demodulators are available.
2. *Successful*: A demodulator decodes the payload.
3. *Collided*: The payload fails to be decoded as the minimum number of fragments is unmet.

Although headers are not essential for payload decoding in this scenario, their presence still influences collision dynamics. We distinguish between *payload* decoding, when the minimum amount of fragments is received, and the payload can be successfully decoded, and *packet* decoding when at least one header replica is received along with the payload.

Fig. 4.8 plots the cumulative decoded payloads against the total packets transmitted using CR1 and 100 demodulators, while Fig. 4.10 is similar but using 1000 demodulators. The comparison is multifaceted:

- Families Comparison: The solid lines represent the *li-fan* family, while the dashed lines depict the *driver* family.
- Decoding Mechanisms: The results derived from the *Early Drop* and *Early Decode* mechanisms, tagged as *earlydd* and shown in blue and purple shades, are set against the baseline demodulator model, shown in orange and green shades.
- Demodulators Count: The data segregates between setups with 100 demodulators in Fig. 4.8 and 1000 demodulators in Fig. 4.10. For reference, the unlimited decoding capacity scenario is illustrated with the label *infp* in red.

Thèse accessible à l'adresse : https://theses.insa-lyon.fr/publication/2026ISAL0011/these.pdf © [D. Maldonado Muñoz], [2026], INSA Lyon, tous droits réservés

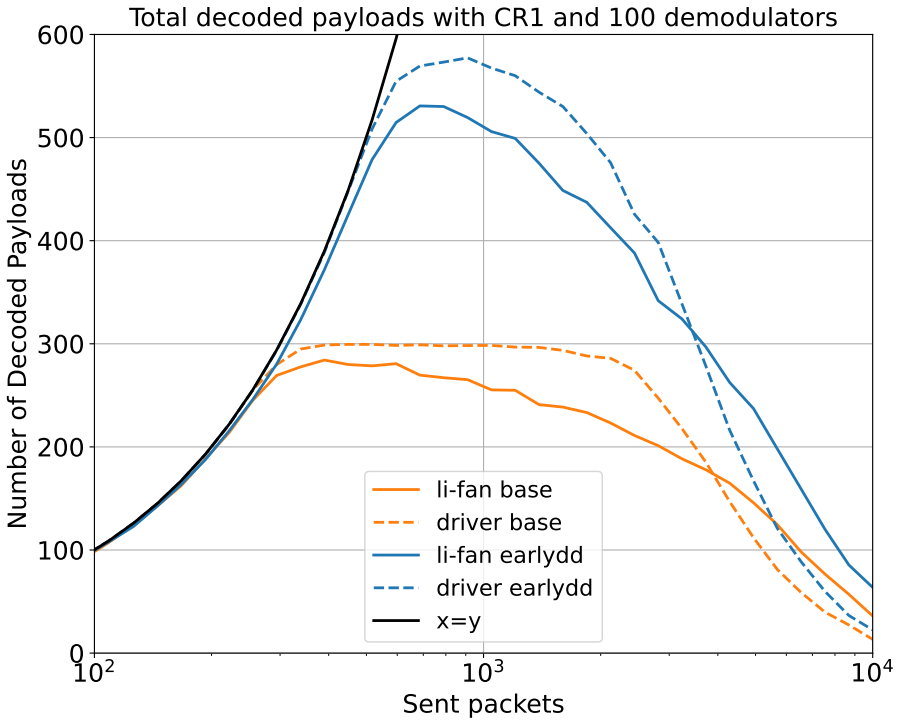


Figure 4.8: Total decoded payload comparison with 100 demodulators for CR1/3.

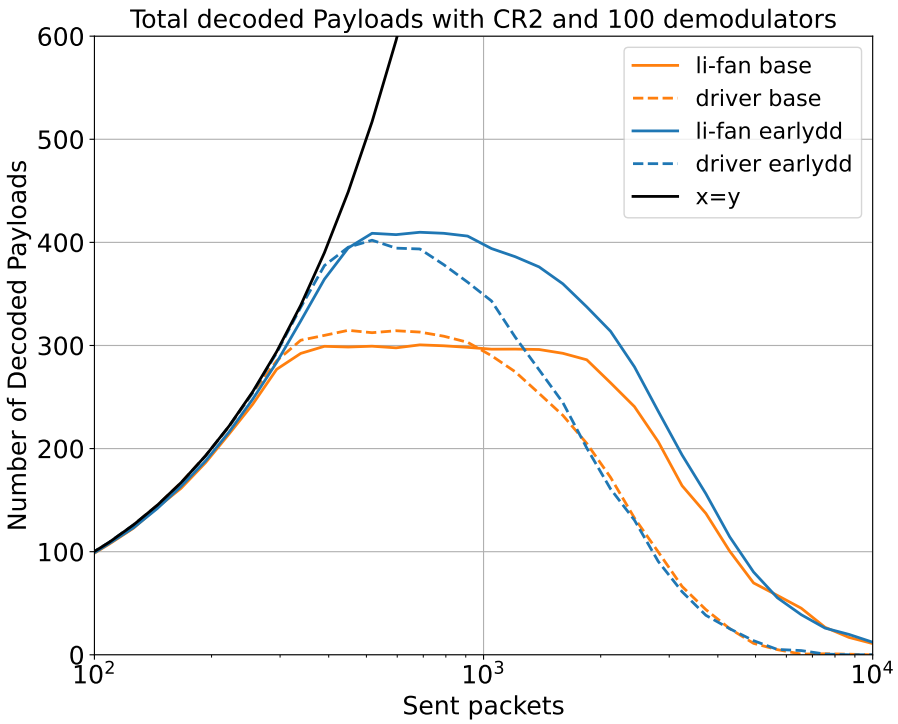


Figure 4.9: Total decoded payload comparison with 100 demodulators for CR2/3.

With the configuration of 100 demodulators (100p), activating the *earlydd* mechanism brings about

Thèse accessible à l'adresse : https://theses.insa-lyon.fr/publication/2026ISAL0011/these.pdf © [D. Maldonado Muñoz], [2026], INSA Lyon, tous droits réservés

a significant enhancement in decoding performance for both the *li-fan* and *driver* families. Specifically, the number of successfully decoded payloads can see an increase of up to 100%, effectively doubling the decoding output. However, when the demodulator count is raised to 1000 (1000p), the benefits of the *earlydd* mechanism become less pronounced. Even so, the decoding capability curve is nudged closer to that of the model with infinite decoding capacity. A notable observation is that, under this configuration, the *li-fan* family witnesses an improvement of up to 50% in successfully decoded payloads when there are around 4000 transmitted packet.

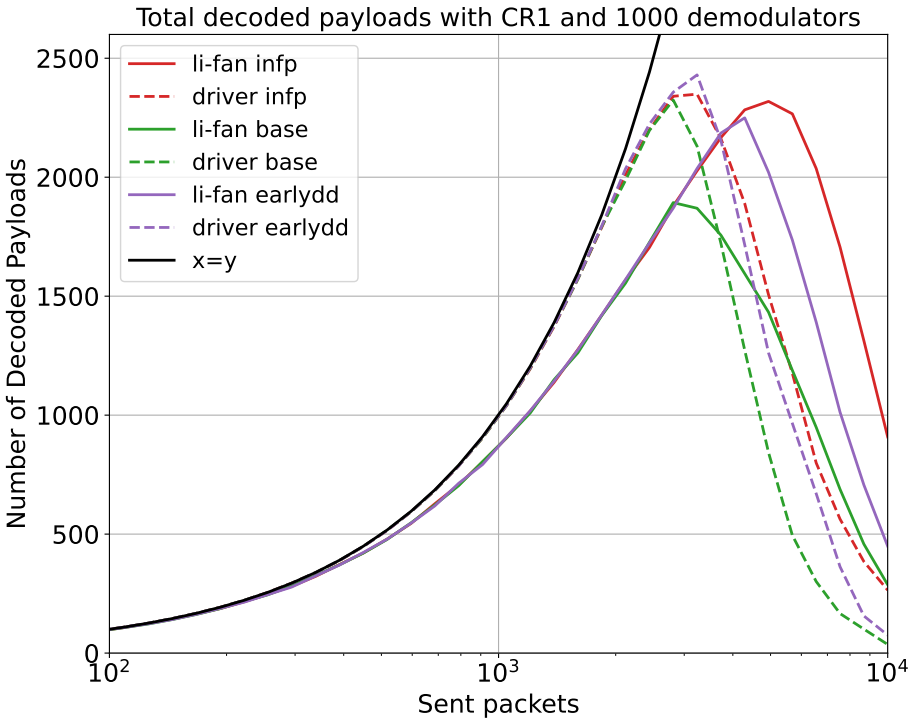


Figure 4.10: Total decoded payload comparison with 1000 demodulators for CR1/3.

When contrasting the performance of the *li-fan* and *driver* FHS families, the *driver* FHS consistently outperforms the *li-fan* up to a specific threshold of transmissions. This superiority becomes even more pronounced when operating with 1000 demodulators (1000p). Beyond this threshold, however, a transition from the *driver* FHS to the *li-fan* FHS has the potential to yield better network throughput.

As illustrated in Fig. 4.9 for the case using CR2, the *earlydd* mechanism consistently enhances the decoding capacity for both the *li-fan* and *driver* FHS families. The improvement is particularly significant when utilizing 100 demodulators (100p), but it tapers off as the channel nears saturation. The benefits are less pronounced when employing 1000 demodulators (1000p), illustrated in Fig. 4.11.

A comparative evaluation of the *li-fan* and *driver* families reveals a considerable advantage for the *li-fan* family. This superiority is especially evident in the 1000p setup, where the decoding capacity of the *li-fan* family surpasses that of the *driver* family by a remarkable 170%. While the *driver* family does exhibit marginally superior performance under lighter network loads, the disparity at higher loads suggests that the *li-fan* family is the best choice when CR2 is in use.

Thèse accessible à l'adresse : https://theses.insa-lyon.fr/publication/2026ISAL0011/these.pdf © [D. Maldonado Muñoz], [2026], INSA Lyon, tous droits réservés

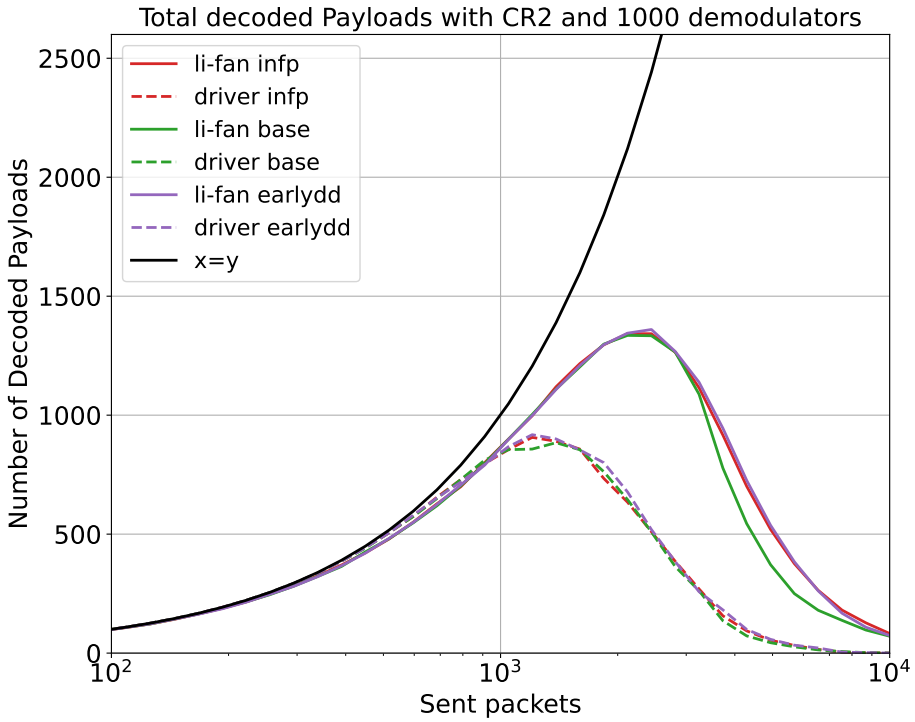


Figure 4.11: Total decoded payload comparison with 1000 demodulators for CR2/3.

4.4.4 Packet versus Payload Analysis

This section compares packet decoding and payload decoding. While the latter was the primary focus of the preceding section, the emphasis here shifts to packet decoding. Packet decoding implies that at least one header replica is received in addition to a successful payload decode.

For the context of this analysis, both the *Early Drop* and *Early Decode* mechanisms remain activated. Our metric of interest is the total decoded data compared to the total data sent in kilobytes. This approach offers a balanced comparison between CR1/3 and CR2/3. Notably, despite requiring the same number of hops, CR1/3 encodes less data than CR2/3. Thus, this metric facilitates an unbiased assessment of their performance relative to the data throughput they deliver.

100 Processor Analysis

The distinction between packet and payload decoding is brought to the fore in Figures 4.12 and 4.14. The *li-fan* and *driver* FHS families are portrayed with different color codes: orange and green for *li-fan*, and blue and purple for *driver*. A further distinction is made between CR1 (depicted in shades of orange and blue in Fig. 4.12) and CR2 (represented in shades of green and purple in 4.14). Dashed lines signify packet (*pckt*) decoding, while solid lines represent payload (*pyld*) decoding.

The observation from the figure confirms the intuitive expectation: the rate of packet decoding, which requires both a successful payload and at least one header replica, is invariably lower than the payload-only decoding. This is depicted by the consistently higher solid lines (*pyld*) compared to their dashed counterparts (*pckt*) across the graph.

Thèse accessible à l'adresse : https://theses.insa-lyon.fr/publication/2026ISAL0011/these.pdf © [D. Maldonado Muñoz], [2026], INSA Lyon, tous droits réservés

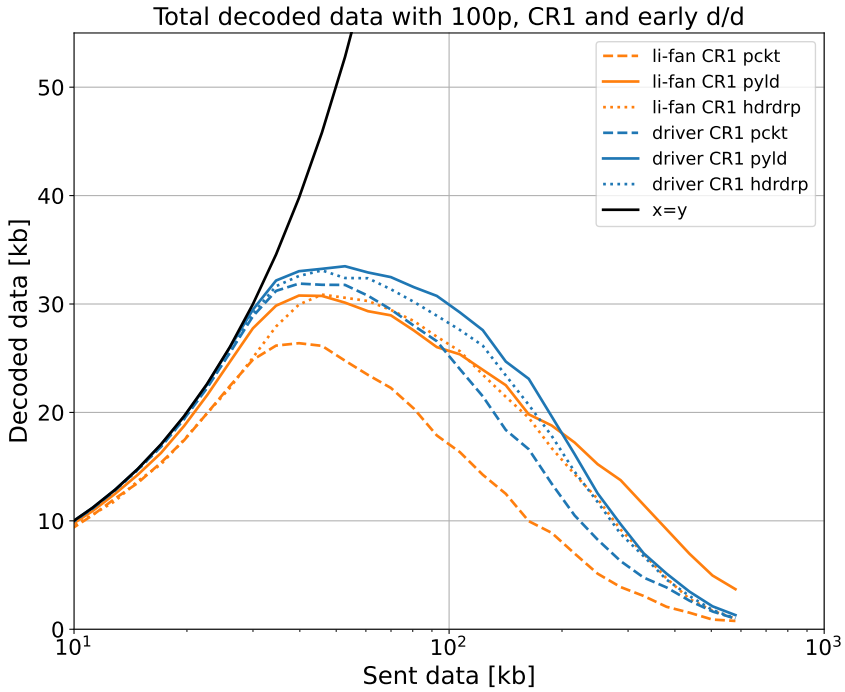


Figure 4.12: Total decoded data volume with 100 demodulators, CR1/3, employing Early-Drop and Early-Decode mechanisms.

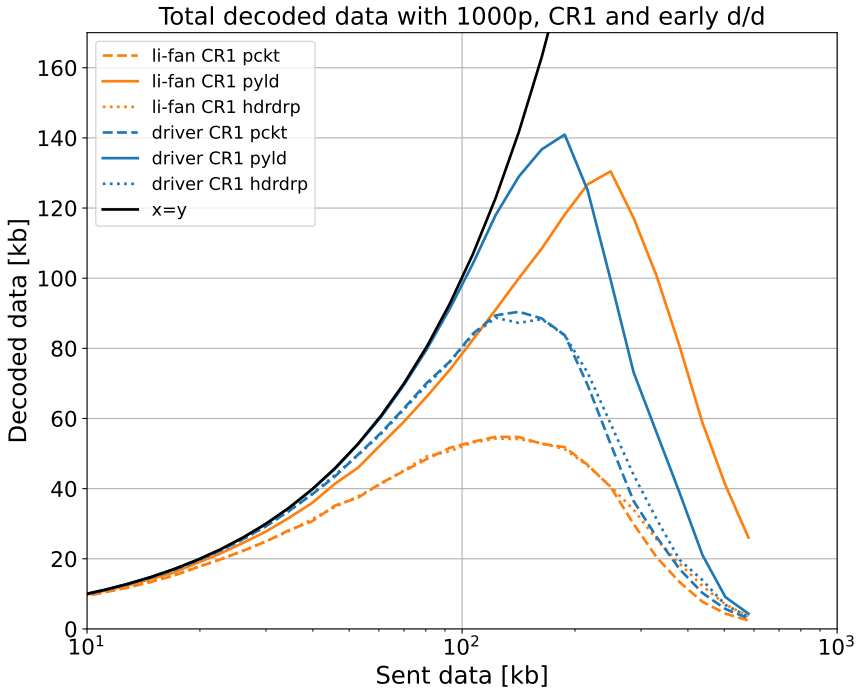


Figure 4.13: Total decoded data volume with 1000 demodulators, CR1/3, employing Early-Drop and Early-Decode mechanisms.

Thèse accessible à l'adresse : https://theses.insa-lyon.fr/publication/2026ISAL0011/these.pdf © [D. Maldonado Muñoz], [2026], INSA Lyon, tous droits réservés

When considering CR1, this decrease in the packet decoding performance relative to payload decoding also manifests in the competitive dynamics between the *li-fan* and *driver* families. Here, the *li-fan* family fails to outperform the *driver* family across the entirety of the depicted range.

Turning our attention to CR2, a similar trend unfolds. Although *li-fan* had previously displayed a higher efficiency, this distinction diminishes when pitted against *driver* in the context of packet decoding. The relative performance advantage of *li-fan* observed in the payload-only decoding scenario wanes, cementing the assertion that the header replica decoding requirement poses a challenge to both families, altering their relative efficiencies. For a dense network, *li-fan* with CR2 achieves the best performance.

1000 Processor Analysis

With the enhanced processing capacity depicted in Figure 4.13, we observe distinct trends compared to the prior analysis with 100p.

The increased processing capability does not shield the *li-fan* family from the added complexity of *pckt* decoding, as the family remains noticeably more affected than when only considering *pyld* decoding. For CR1, the performance gap between the two families is quite pronounced. The *driver* family outpaces the *li-fan* by a substantial margin, decoding up to 60% more data. This demonstrates the *driver*'s efficiency and highlights the challenges *li-fan* encounters when packet decoding is in play, even with enhanced processing capability.

For CR2, in Figure 4.15, the dynamics between the two families become more intricate. The *driver* family retains dominance over a broader range of transmissions before *li-fan* takes the lead. This extension of the *driver*'s dominant zone underscores the impact of packet decoding on the *li-fan*'s performance, even in the context of CR2.

Taking a step back to compare the broader impact of the coding rates, it is evident that CR2 offers superior throughput compared to CR1. This is particularly true when the available OCW channels are kept constant for both coding rates. The data, therefore, lends itself to the idea that, in terms of raw throughput and irrespective of the FHS family in question, CR2 presents a more efficient encoding choice. Again, for a dense network, *li-fan* with CR2 achieves the best performance.

4.4.5 Header Drop Analysis

Incorporating the *Early Header Drop* mechanism brings about a significant shift in the dynamics of the decoding process, casting a spotlight on the vital role headers play in LR-FHSS networks.

In Figures 4.12 and 4.14, which detail the outcomes with 100p, a noteworthy observation is the proximity of the *hdrdrp* (*Early Header Drop* activated) curves to the *pyld* (payload decode with *Early Header Drop* off) curves. This indicates that when relieved from payloads whose headers were not successfully received, the demodulators can maintain a decoding rate almost as efficiently as if headers were non-essential. This suggests that in more constrained processing environments, the *Early Header Drop* mechanism assists in focusing resources on more probable decoding successes.

However, the dynamics change as the processing power is ramped up in Figures 4.13 and 4.15. Here, the *hdrdrp* curves converge with the *pckt* curves. The vast gap between the performance of the *hdrdrp* and *pyld* signifies missed decoding opportunities. The divergence between these curves indicates that with more processing resources, there is substantial potential for successfully decoding

Thèse accessible à l'adresse : https://theses.insa-lyon.fr/publication/2026ISAL0011/these.pdf © [D. Maldonado Muñoz], [2026], INSA Lyon, tous droits réservés

payloads even when missing headers. This observation underscores the limitation of being overly reliant on headers in LR-FHSS systems.

Given the contrast observed between the *hdrdrp* and *pyld* results in the 1000p scenario, the findings hint at the prospective advantages of a headerless decoding mechanisms [35]. If LR-FHSS networks were to develop a reliable method of decoding payloads without needing headers, it could substantially amplify the effective throughput and overall performance. With its apparent untapped potential, this direction warrants further research and could radically change LR-FHSS network methodologies.

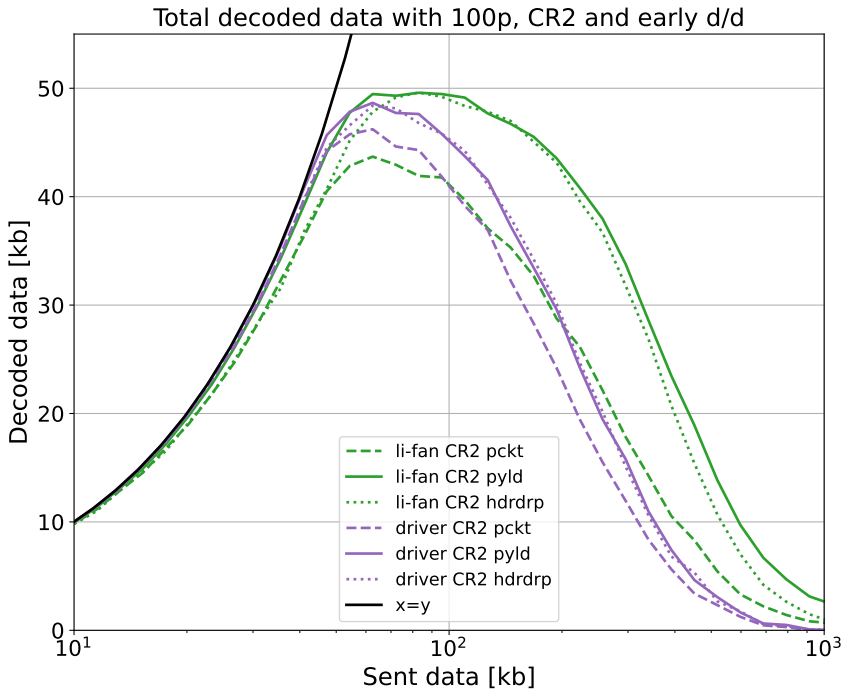


Figure 4.14: Total decoded data volume with 100 demodulators, CR2/3, employing Early-Drop and Early-Decode mechanisms.

4.4.6 Header Tolerance Analysis

This section offers an extended perspective on decoding dynamics by introducing a “collision tolerance" for the header to model its more robust modulation properly. In Fig. 4.16 for the 100p scenario, the inclusion of the *Header Tolerance* (*hdrtol*) displays the immediate benefits of the flexibility offered by this model. While both FHS families witness an improvement, the *li-fan* family reaps a more pronounced uptick in decoding performance. For CR2, even though the *driver* family starts with a performance edge over *li-fan*, this dominance is short-lived. Beyond the 60 Kb transmission threshold, *li-fan* surges ahead with its decoding capacity, outperforming the *driver* by as much as doubling it. Similarly, in the CR1 scenario, the earlier observations from Fig. 4.8 come to mind, where *li-fan* eventually surpasses the *driver* in decoding performance after a specific transmission volume.

Scaling the processing power to 1000p, as represented in Fig. 4.17, the benefits of the *Header Tolerance* model become even more conspicuous. The resilience against header collisions boosts the decoding capacities for both families, but once again, the *li-fan* stands out. The CR2 results reiterate the shift in dominance, with *li-fan* pulling far ahead of the *driver* family, especially after a

Thèse accessible à l'adresse : https://theses.insa-lyon.fr/publication/2026ISAL0011/these.pdf © [D. Maldonado Muñoz], [2026], INSA Lyon, tous droits réservés

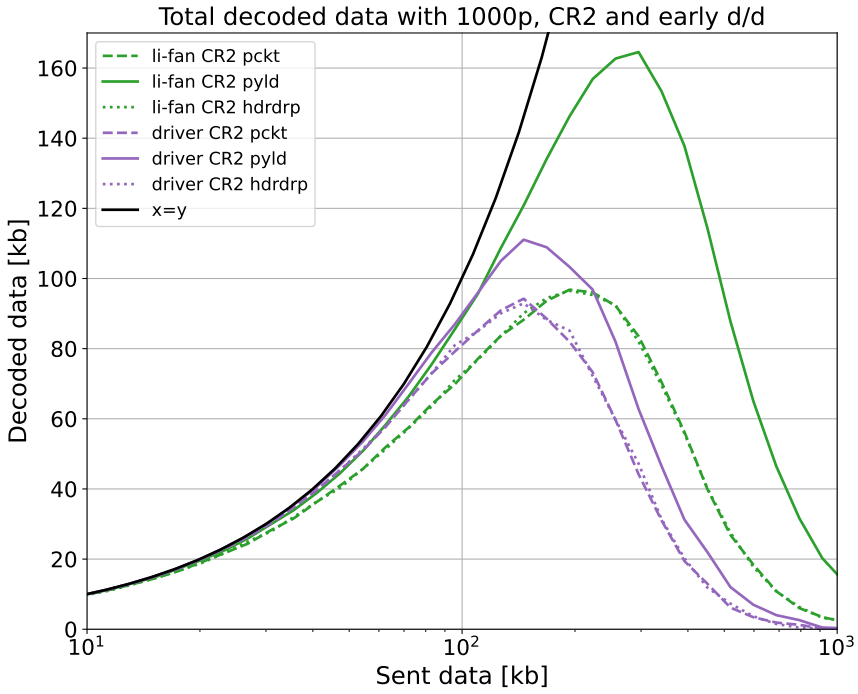


Figure 4.15: Total decoded data volume with 1000 demodulators, CR2/3, employing Early-Drop and Early-Decode mechanisms.

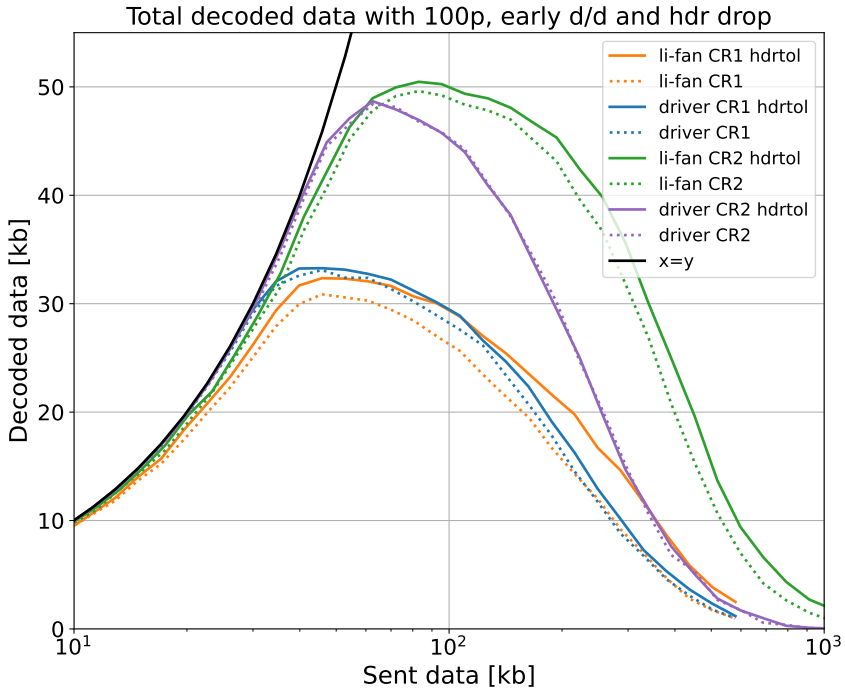


Figure 4.16: Total decoded data volume with 100 demodulators employing Early-Drop, Early-Decode, Header Drop, and Header Tolerance of 4 time slots.

Thèse accessible à l'adresse : https://theses.insa-lyon.fr/publication/2026ISAL0011/these.pdf © [D. Maldonado Muñoz], [2026], INSA Lyon, tous droits réservés

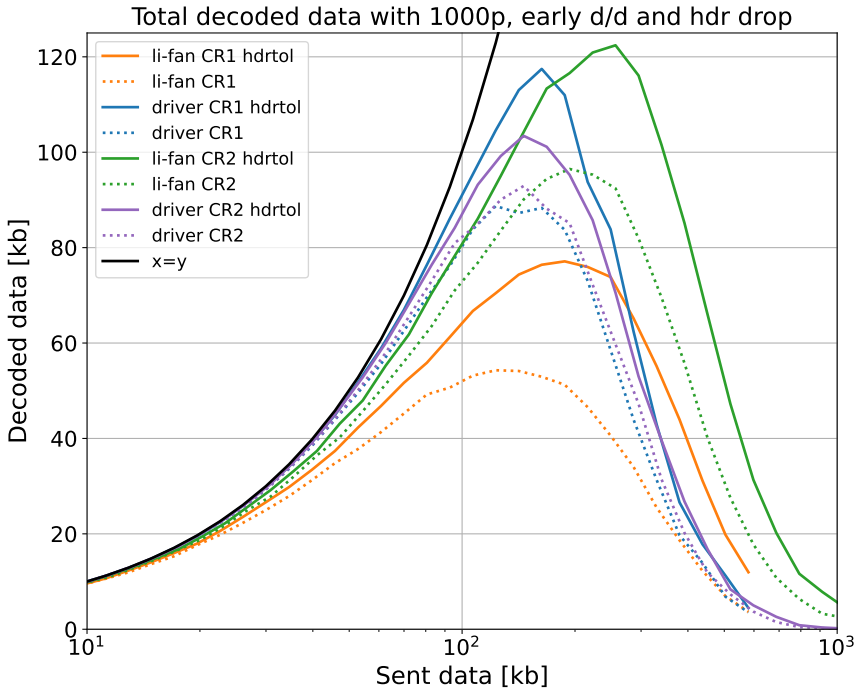


Figure 4.17: Total decoded data volume with 1000 demodulators employing Early-Drop, Early-Decode, Header Drop, and Header Tolerance of 4 time slots.

specific transmission volume. The differential reaches a staggering 100%, highlighting the merits of the *li-fan* family in this specific scenario. The CR1 results echo a similar outcome, marking an apparent comeback for *li-fan* over *driver* with increasing transmission counts.

This analysis accentuates the importance of adaptability in network protocols and how slight adjustments, such as allowing for some collision tolerance in headers, can have outsized impacts on performance metrics. It underscores the potential of optimizing network parameters to adapt to specific requirements, thus enhancing overall network efficiency.

Finally, Table 4.5 presents a comprehensive summary of the most effective FHS families for each variant of LR-FHSS discussed in this study relative to different scales of node counts. The findings strongly suggest that the strategic integration of sequence design and resource allocation methods explored in this research pushes LR-FHSS to its scalability limits. Consequently, LR-FHSS stands out as a highly viable solution for managing the extensive IoT connectivity demands posed by the evolving direct-to-satellite IoT paradigm.

4.5 Conclusion

The emerging integration of IoT with LEO satellites necessitates the evolution of robust, efficient, and scalable communication protocols. Our in-depth exploration into LR-FHSS modulation, mainly focusing on the design of FHS and efficient demodulator allocation strategies, has highlighted the significant promise of Wide-Gap sequences for massive LEO satellite IoT communications.

Our primary findings and contributions are summarized as follows:

Thèse accessible à l'adresse : https://theses.insa-lyon.fr/publication/2026ISAL0011/these.pdf © [D. Maldonado Muñoz], [2026], INSA Lyon, tous droits réservés

Table 4.5: Optimal FHS family selection for different LR-FHSS configurations

100 Decoding Processors				
Node Count	Data Volume CR1 in Kb	CR1	Data Volume CR2 in Kb	CR2
0 - 500	0 - 29	*driver*	0 - 61	*driver*
500 - 1725	29 - 100	*driver*	61 - 209	*li-fan*
1725 +	100 +	*li-fan*	209 +	*li-fan*
1k Decoding Processors				
Node Count	Data Volume CR1 in Kb	CR1	Data Volume CR2 in Kb	CR2
0 - 1240	0 - 72	*driver*	0 - 150	*driver*
1240 - 6550	72 - 380	*driver*	150 - 793	*li-fan*
6550 +	380 +	*li-fan*	793 +	*li-fan*

Actual sequences used by LR-FHSS devices We have highlighted in Section 4.2 how the frequency hopping sequences of LR-FHSS are constructed in real LR-FHSS devices. This knowledge can help the community improve the sequence construction in the future.

Wide-Gap Sequence Design The research highlights the superior performance of the *li-fan* FHS sequence family over conventional sequences within LR-FHSS contexts, notably in setups involving advanced demodulators.

Demodulator Allocation Strategies The introduction of “Early-Decode" and “Early-Drop" strategies represents a transformative approach to optimizing decoding resources for LR-FHSS gateways.

Some guidelines for future work to further enhance the scalability of the LR-FHSS network include the possibility of decoding LR-FHSS payloads without the header information. Also, future work will extend this study with refined channel models incorporating additional physical-layer effects.

Thèse accessible à l'adresse : https://theses.insa-lyon.fr/publication/2026ISAL0011/these.pdf © [D. Maldonado Muñoz], [2026], INSA Lyon, tous droits réservés

Thèse accessible à l'adresse : https://theses.insa-lyon.fr/publication/2026ISAL0011/these.pdf © [D. Maldonado Muñoz], [2026], INSA Lyon, tous droits réservés

Chapter 5

Robustness

This chapter presents a comprehensive enhanced LR-FHSS receiver model designed to address the challenges of headerless frame recovery in space-terrestrial IoT networks. Each component of the receiver architecture is described in detail throughout the following subsections, with particular emphasis on adaptations for satellite communication environments.

5.1 Background on LR-FHSS Scalability

Considering the large fields of view of LEO satellites, packet collision is a much more challenging issue in space DtS-IoT than in terrestrial networks. Even though LR-FHSS enhanced the scalability of legacy LoRaWAN concerning terrestrial networks, pushing scalability limits further as needed in DtS-IoT remains an open challenge not addressed by the recent publications listed in the section above. Indeed, the state-of-the-art specifically focused on LR-FHSS scalability is limited. As discussed below, researchers focused mainly on reducing collisions by optimizing the frequency hopping sequence (FHS) and recovering LR-FHSS frames despite losing all header replicas.

Optimizing the FHS. The FHS is a crucial element that impacts the scalability of LR-FHSS, as it fundamentally determines how many fragments from different LR-FHSS frames overlap. The relationship between the possible FHSs and the extraction rate of colliding frames encompasses the intricate interplay between LR-FHSS's error correction mechanisms and the mandatory frequency shifts dictated by grid definitions. However, to our knowledge, limited research exists on the design of appropriate FHS techniques for LR-FHSS. One example is the research on the Wide-Gap FHS (WGFHS) family addressed in [2]. Also, Zhang et al. proposed a dynamic frequency hopping method that accounts for the changing SNR values of the sub-channels [83]. Wang et al., on the other hand, proposed a frequency hopping design that incorporates segment-level coding in a high-order Galois field with erasure detection to enhance immunity against clustered errors [84].

Recovering headerless frames. Recent research has demonstrated that header collision is the primary cause of frame loss in congested LR-FHSS channels. This collision results in the loss of header replicas, rendering it impossible to successfully decode the subsequent payload fragments. The header fragility problem has been highlighted as the primary limitation in LR-FHSS scalability in several works [85, 86, 35]. One identified reason is the inefficiency of repetition codes, prompting Knop et al. to propose combining header replicas from multiple packets sent by the same user [87]. Still, when all header replicas are lost, none of these approaches tries to recover the frames. Recent work in [35] proposed a Mixed Integer Linear Programming (MILP) formulation and a

Thèse accessible à l'adresse : https://theses.insa-lyon.fr/publication/2026ISAL0011/these.pdf © [D. Maldonado Muñoz], [2026], INSA Lyon, tous droits réservés

heuristic approach to optimize the allocation of FHS in the dictionary to a series of payload fragments lacking an associated LR-FHSS header. However, this approach has several limitations, including the omission of Doppler effects—a significant issue in space and satellite communications—and the assumption that all headers are absent in the receiver decoding matrix, whereas, in practice, a combination of successful and lost headers is present.

We propose a definitive approach to headerless LR-FHSS decoding that addresses the limitations above. To demonstrate the practical applicability of our proposal, we present an architecture for a headerless-capable LR-FHSS receiver, building on the existing transceiver designs proposed by the community [88, 89]. To properly frame our contribution, the following subsections describe the details of LR-FHSS modulation, the challenges imposed by the highly dynamic space-terrestrial channel, and the associated headerless LR-FHSS decoding techniques.

5.2 System Model

5.2.1 Signal and Channel Model for LEO Orbits

In this chapter, two related propagation models are used: i) a *power-centric* model, used to understand the behaviour of the collision from an interference perspective, and ii) a *collision-centric* model, which is a simplification of the power-centric model and is mainly used to offload more complex analysis when deemed unnecessary. We focus on a single OCW for both models to simplify the approach without losing generality. Since OCWs do not overlap, extending this model to multiple OCWs is straightforward, as it involves instantiating separate models for every OCW channel.

Power-Centric Model

The Gaussian Minimum Shift Keying (GMSK) modulation transmits LR-FHSS packets. Since decoding is not the focus of this work, we can simplify our physical layer model by abstaining from the actual transmission of information and focusing on the power of the transmitted signals. GMSK is a constant-amplitude modulation so that we can estimate the signal power per symbol as the square of the modulus of the complex-valued symbol. This power estimation is done for both headers and fragments in their time-frequency representation, with the power equally distributed over the OBW sub-channel.

We assume no shadowing or small-scale fading in the channel model, as in [35]. Therefore, the power received by the LEO satellite from the i-th end-device P_i is computed as

$$P_i = P_{\mathrm{t}} \cdot G_{\mathrm{r}} \cdot G_{\mathrm{t}} \cdot \mathrm{Pl}(d_i, f_{\mathrm{c}}), \tag{5.1}$$

where P_{t}, G_{r} and G_{t} are the transmission power, the receiver antenna gain, and the transmitter antenna gain for the i-th device, respectively. $\mathrm{Pl}(d_i, f_{\mathrm{c}})$ is the free space path loss computed from the Friis formula, which depends on d_i the distance from the i-th end-device to the satellite and f_{c} the carrier frequency. Since all end-devices are considered the same P_{t}, G_{r} and G_{t} are the same for all devices, hence the lack of the i index. For simplicity, we do not consider propagation losses in the atmosphere due to absorption. Finally, at the satellite receiver, we consider noise equal to the noise floor per specifications available in the Application Note documentation from Semtech [90].

Thèse accessible à l'adresse : https://theses.insa-lyon.fr/publication/2026ISAL0011/these.pdf © [D. Maldonado Muñoz], [2026], INSA Lyon, tous droits réservés

Collision-Centric Model

In this simplified model, we consider three possible outcomes: i) no signal, ii) a single signal, and iii) collided signals. While simulations always know incoming signals, real-world scenarios are more complex and require robust collision detection mechanisms to differentiate between single and collided signals. In [89], the authors propose several interference management techniques, proving their effectiveness in determining whether each symbol from a fragment is either collided or successfully received without interference. Our collision-centric model assumes these techniques are valid and operates under the assumption that all signals are above the noise level.

5.2.2 Interference, Collision, and Capture Effect

For power-centric and collision-centric models, headers and fragments interfere when they overlap in time and frequency (i.e., fall onto overlapping OBWs). Throughout this work, the term *collision* is used to designate all headers and fragments that interfere and cannot be decoded as a consequence.

In actual transmissions, interfering signals can experience the capture effect, in which headers and fragments that fully or partially overlap in time and frequency with a favourable power ratio might allow for perfect decoding of the higher-powered one. Here, we consider the worst-case scenario in which, if the overlap is present, collision ensues regardless of the overlap extent or power ratio between the interfered signals. It should be noted that while channel sensing can detect collisions, we consider that under our assumptions, the recovery of collided fragments is impossible; hence, the capture effect is not considered in this work. Considering the capture effect and advanced collision determination and avoidance techniques such as the ones presented in [89], it would be possible to decode even more fragments and thus further increase the throughput.

Based on the received power and given the constant envelope of the GMSK used for the LR-FHSS transmissions, SINR-based collision detection techniques can be used to determine if a given header or fragment is collided or not, such as the ones proposed by Temim et al. [89]. Our proposed model assumes such techniques are implemented and can be used to rule out collisions at the symbol level.

5.2.3 Doppler Effect Model

Doppler effect significantly influences satellite communications by introducing frequency shifts as satellites move relative to ground stations and end devices. These shifts can distort signals, degrade signal-to-noise ratio, and cause synchronization errors. Doppler compensation techniques are employed to mitigate these effects, adjusting transmitted frequencies dynamically. In the context of DtS-IoT, specifically when considering satellites in the LEO orbit, Doppler shifts are considerable due to the high orbital velocities (e.g., in the order of 7 km/s in LEO) concerning the relatively static end devices on the ground.

To reason about Doppler, let H be the satellite altitude, R the radius of the earth, g the acceleration of gravity on the surface, c the speed of light in vacuum, f_c the carrier frequency, v the satellite's velocity. Let also $x = 1 + H/R$. The Doppler frequency shift f_d is given by

$$f_d = \frac{f_c}{c}\sqrt{\frac{gR}{x}} \cdot \frac{\sin(\phi)}{\sqrt{x^2 - 2 \cdot x \cdot \cos(\phi) + 1}}, \tag{5.2}$$

Thèse accessible à l'adresse : https://theses.insa-lyon.fr/publication/2026ISAL0011/these.pdf © [D. Maldonado Muñoz], [2026], INSA Lyon, tous droits réservés

discussed in detail in [91], where

$$\phi = t\sqrt{\frac{g}{Rx^3}}. \tag{5.3}$$

Figure 2.2 shows the Doppler shift seen from the satellite as it passes over the a region with IoT devices. The Doppler shift is -20 kHz when the satellite approaches from the horizon (at t= -400), reaches 0 kHz when the satellite is directly above the region (at t=0), and then increases again until 20 kHz as it moves away from the devices (at t= 400). This behavior has been observed in several studies, including by Ali et al. [92]. The Doppler rate is defined as the variation of the Doppler shift over time and is illustrated in Figure 2.2. The peak Doppler rate is when the satellite is beyond $t = 0$ (zenithal position) and when the Doppler shift is 0.

Doppler in LR-FHSS with LEO

According to Semtech, LR-FHSS is specifically designed to tolerate frequency offset (directly related to Doppler shift) and frequency drift (directly related to Doppler rate) to cope with the Doppler effect observed in LEO satellite communications. To assess this claim, we simulated a 200 kHz receiver bandwidth, with end-devices sending LR-FHSS frames within an OCW with a bandwidth of 137 kHz (more detail on the simulation environment is provided in Section IV) in the LEO scenario. The minimum SNR is 10 dB. The resulting time-frequency spectrogram is presented in Figure 5.1. The received signal power is computed as given by Eq 5.1.

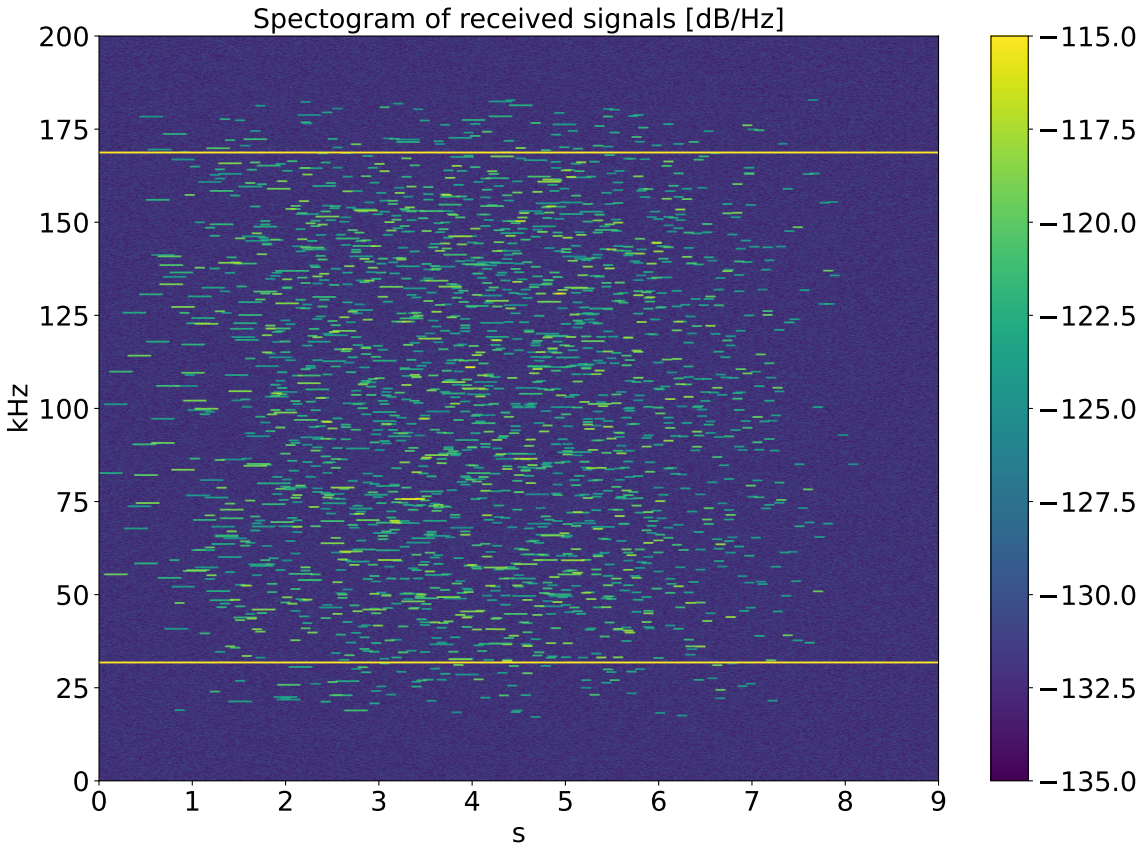
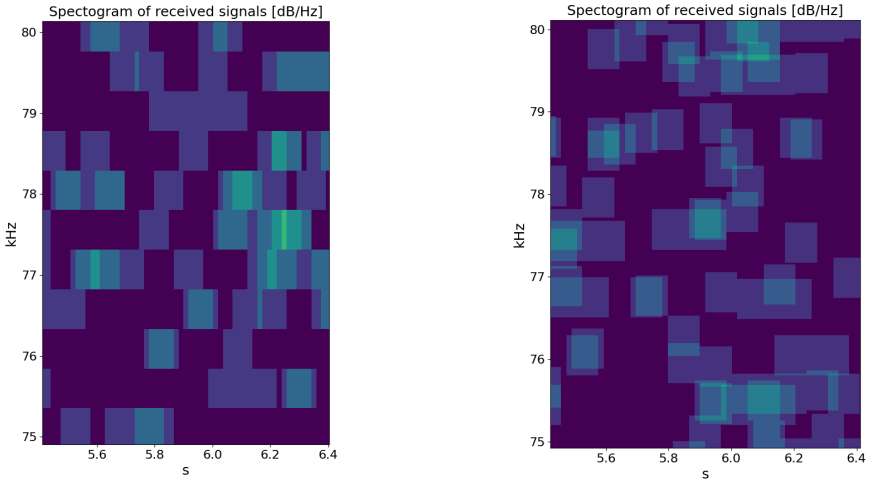


Figure 5.1: Spectrogram of 100 received LR-FHSS transmissions.

Due to the Doppler shift, we can observe how some frames fall outside the originally transmitted 137 MHz band (indicated with yellow horizontal lines). Our simulation validates that a larger receiver

Thèse accessible à l'adresse : https://theses.insa-lyon.fr/publication/2026ISAL0011/these.pdf © [D. Maldonado Muñoz], [2026], INSA Lyon, tous droits réservés



(a) Terrestrial (no Doppler shift)

(b) DtS-IoT (with Doppler shift)

Figure 5.2: Comparison of received LR-FHSS frames, terrestrial vs. DtS-IoT scenarios.

window of 200 MHz makes LR-FHSS tolerant to the Frequency Shift in DtS IoT scenarios. The Frequency Offset tolerance in LR-FHSS is 31.65 kHz (as reported by Semtech in Table 9 from [34] and presented in Table 2.2.6). The same work indicates that for LR-FHSS, a frequency drift of up to 100 Hz/s does not cause observable performance degradation, and a frequency drift of up to 300 Hz/s causes performance degradation of up to 1.5 dB [34]. By observing Figure 2.2 and assuming that Semtech's report is accurate, the Doppler simulation results show no degradation should be observed in LR-FHSS before t=-80 and after t=80, where the Doppler Rate is under 100 Hz/s. However, a performance degradation of up to 1.5 dB may only occur around $t = 0$ when the satellite passes just over the device on the ground.

Figure 5.2 shows a closer look at the spectrogram of received frames without Doppler shift (on the left) and with Doppler shift (on the right). The spectrogram on the left could represent a typical terrestrial network with a static gateway. However, the spectrogram on the right represents what would happen in a typical DtS-IoT with a fast-moving LEO satellite when the Doppler effect is significant. Note that without the Doppler effect (on the left), the received frames are all aligned in terms of OBW (left axis), while with the Doppler effect (on the right), they are misaligned, with non-existent OBW boundaries. It is important to note that the Power-Centric model is used to compute Figures 5.1 and 5.2. However, the Collision-Centric model is used to introduce the LR-FHSS receiver architecture in the next section.

5.2.4 Practical Perspective of System Model Assumptions

The following assumptions are incorporated into the proposed System Model to simplify the analysis and implementation in resource-constrained onboard computers while preserving the critical characteristics of LEO satellite signal propagation. These assumptions were carefully selected to ensure the model remains practical and applicable in real-world scenarios, particularly for DtS-IoT networks.

1. **No Small-Scale Fading:** In line with previous works on satellite IoT communications, the model assumes no small-scale fading or shadowing effects in the channel. While this assumption simplifies the propagation environment, it remains reasonable, as small-scale fading has a limited impact in the relatively open-space environment between ground terminals and LEO satellites.

Thèse accessible à l'adresse : https://theses.insa-lyon.fr/publication/2026ISAL0011/these.pdf © [D. Maldonado Muñoz], [2026], INSA Lyon, tous droits réservés

2. **No Atmospheric Losses:** Atmospheric propagation losses due to absorption are not considered in this model. This assumption is a valid approximation for the frequencies used in LR-FHSS, as absorption is minimal at these ranges. Therefore, the focus on free-space path loss does not significantly impact the model's accuracy.

3. **Collision Handling Assumptions:** The collision-centric model assumes robust collision detection mechanisms, which are practical and feasible based on current research in interference management techniques. These methods, as proposed in [89], are grounded in real-world implementations.

4. **Doppler Effects:** Unlike previous works that overlook Doppler shift, our model explicitly accounts for Doppler effects, which are significant in LEO satellite communications due to the high orbital velocities.

5. **Simplified Fragment Collisions:** The assumption that collisions occur when fragments overlap in time and frequency is grounded in practical satellite communication conditions. Although we assume no recovery of collided fragments, this reflects the worst-case scenario.

5.3 Enhanced LR-FHSS Receiver Architecture

This section contains the details of our proposed Enhanced LR-FHSS Receiver model, describing each module in detail in the following subsections.

5.3.1 Headerless Frame Decoding

A significant cause for losing LR-FHSS frames is the collision of headers, as shown by Fraire et al. [35]. The authors proposed a mechanism enabling the decoding of headerless frames based on a greedy approach. However, the authors did not account for satellite communications' specific characteristics, such as Doppler effect, and based their model on strict assumptions. The proposed Greedy Headerless Decoding heuristic, listed in Algorithm 3, processes each time slot t sequentially. For each of the 384 known sequences, it checks if matrix M contains a transmission starting at time slot t with sequence s. If such a transmission exists, (s, t, P) is added to $\hat{T}$, where P is the length of the sequence s. This greedy heuristic has a time complexity of $\mathcal{O}(T \cdot S \cdot P)$ when the entire matrix M is known in advance, as the primary operation involves three nested loops: the first loop (line 2) runs T times, the second loop (line 3) runs S times, and the third loop (line 5) runs P times. Indeed, the principal operation of line 6 is performed within three nested `for` loops.

5.3.2 Enhanced LR-FHSS Receiver Architecture

To retrieve lost payloads from LR-FHSS frames, we propose here an enhanced LR-FHSS receiver with the above-mentioned Greedy Headerless Decoding heuristic at its core. We improved this heuristic by taking into account the specific characteristics of satellite communications and relaxing several of their model assumptions, as we present next. The diagram in Figure 5.3 represents a generic LR-FHSS gateway (shaded block) receiving frames from end-devices. The diagram depicts the end-to-end communication process with the following steps:

Thèse accessible à l'adresse : https://theses.insa-lyon.fr/publication/2026ISAL0011/these.pdf © [D. Maldonado Muñoz], [2026], INSA Lyon, tous droits réservés

Algorithm 3: Greedy Headerless Decoding Heuristic (adapted from [35]).

Input: T, S, P and M

$\hat{T} \leftarrow \{\}$;
for $t \in [1; T]$ **do**
  for $s \in S$ **do**
    $found \leftarrow true$;
    for $p \in [1; P]$ **do**
      if $M[t + p - 1][s[p - 1]] \neq 1$ **then**
        $found \leftarrow false$;
      end
    end
    if $found = true$ **then**
      $\hat{T} \leftarrow \hat{T} \cup \{(s, t, P)\}$;
    end
  end
  return $\hat{T}$
end

1. The end-devices transmit N LR-FHSS frames with a single Coding Rate and variable payload length (the number of payload fragments being within the range $[P_{min}, P_{max}]$) over a given time. The set of transmissions is represented by $\mathcal{T}_N$.

2. The gateway module opens a reception window of bandwidth BW during a given time window. The data is sampled in F frequency slots and T time slots, and the resulting matrix $\mathcal{M}_N$ is stored in the buffer [89]. Matrix $\mathcal{M}_N$ contains all the received LR-FHSS packets.

3. The *Header Pre-Decoder* module identifies the set of transmissions whose header is successfully received, i.e., at least one replica can be decoded, denoted as $\mathcal{T}_S$.

4. The *FHS Locator* module then infers an approximation of the set of transmissions whose header part is unsuccessfully received, *i.e.*, all headers are collided, denoted as $\hat{\mathcal{T}}_C$. Note that it is difficult to know $\mathcal{T}_C$ exactly, as the header information is missing, and thus the gateway has no information on the FHS used for the fragments.

5. Finally, the *Payload Decoder* module receives as input the original sampled matrix $\mathcal{M}_N$, the transmission set $\mathcal{T}_S$ and the uncertain collision set $\hat{\mathcal{T}}_C$, and performs the payload decoding process.

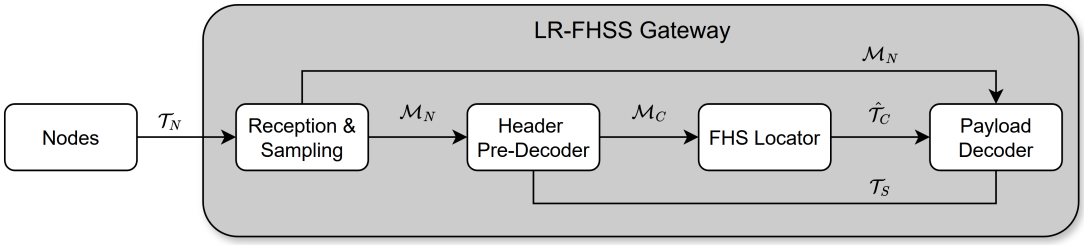


Figure 5.3: LR-FHSS gateway architecture incorporating the Enhanced receiver model.

In the following subsections, we detail the proposed implementation of each enhanced LR-FHSS receiver module.

Thèse accessible à l'adresse : https://theses.insa-lyon.fr/publication/2026ISAL0011/these.pdf © [D. Maldonado Muñoz], [2026], INSA Lyon, tous droits réservés

Reception and Sampling

The Reception and Sampling block is based on the classic LR-FHSS receiver. Jung et al. presented a detailed transceiver model for LR-FHSS-based DtS-IoT scenarios [88]. The received signals are sampled from this block in the matrix M_N.

Header Pre-Decoder

The Header Pre-Decoder module has two objectives. The first objective is to retrieve successfully received replicas from $\mathcal{M}_N$, similar to the traditional LR-FHSS decoder. The set of transmissions whose header was decoded, regardless of the payload status, is represented by $\mathcal{T}_S$. The second objective is to construct a secondary matrix $\mathcal{M}_S$ from $\mathcal{T}_S$, incorporating Doppler shift adjustments as in the original matrix. As the header was decoded, the FHS is known, and the frequency shift can be determined. Then, $\mathcal{M}_S$ can be subtracted from the original $\mathcal{M}_N$ following the next steps:

1. Pre-processing of $\mathcal{M}_N$: matrix $\mathcal{M}_N$ is filtered according to the status of each time slot, either idle (represented by the value 0, meaning no signal or noise), successful (represented by the value 1, meaning a single signal is present) or collided (represented by the value 2, meaning 2 or more colliding signals). This filtering process is simulated based on the number of signals per time slot. In a realistic implementation (i.e., not simulated), collision determination techniques for LR-FHSS receivers should be used for the filtering process, as the ones presented in [89].
2. Matrix $\mathcal{M}_S$ containing $\mathcal{T}_S$ is filtered following the same time slot status convention described before.
3. The difference matrix $\mathcal{M}_C = \mathcal{M}_N \ominus \mathcal{M}_S$ is computed based on the following rules: 1) $2 \ominus 0 = 2 \ominus 1 = 2 \ominus 2 = 2$, since the number of colliding signals is unknown, 2) $1 \ominus 1 = 0$, the only signal present was identified; 3) $1 \ominus 0 = 1$; and 4) $0 \ominus 0 = 0$.
4. Finally, matrix $\mathcal{M}_C$ is made binary, i.e., values equal to 2 become 1. This is done because the FHS Locator receives a binary matrix as input.

As a result of this process, the difference matrix $\mathcal{M}_C$ contains only the sequences with lost headers $\mathcal{T}_C$.

FHS Locator

The FHS Locator module infers the set of transmissions $\mathcal{T}_C$ whose headers failed to be recovered, aiming to locate each sequence in time and frequency. The inference technique is based on the Greedy Headerless Decoding Heuristic introduced in Section 5.3.1.

The Doppler effect in terrestrial scenarios with no mobility is negligible, thus, Algorithm 3 is suitable for the FHS Locator module.

On the other hand, Doppler shifts need to be considered in satellite scenarios. It is known from Figure 2.2 that the range in which a header or fragment will be shifted is between -20 kHz and 20 kHz. Dividing this by the size of the frequency slots allows us to determine the maximum and minimum shifts in frequency slots. Let $\mathcal{D}$ be the set of possible shifts in the frequency domain. Then, Algorithm 3 is updated to search also in frequency.

Thèse accessible à l'adresse : https://theses.insa-lyon.fr/publication/2026ISAL0011/these.pdf © [D. Maldonado Muñoz], [2026], INSA Lyon, tous droits réservés

Algorithm 4: Proposed Doppler-compensated Greedy Headerless Decoding Heuristic.

Input: T, S, D, P and $\mathcal{M}_N$

```
1  T_C ← {};
2  for t ∈ [1;T] do
3      for s ∈ S do
4          for d ∈ D do
5              found ← true;
6              for p ∈ [1;P] do
7                  if find(M_N, t, s, p, d) ≠ 1 then
8                      found ← false;
9                  end
10             end
11             if found = true then
12                 T_C ← T_C ∪ {(s, t, P)};
13             end
14         end
15     end
16     return T_C
17 end
```

The modified version for satellite scenarios is presented in Algorithm 4. The main differences with the heuristic presented in Algorithm 3 are underlined (lines 4 and 7). Algorithm 4 has a time complexity of $\mathcal{O}(T \cdot S \cdot P \cdot |\mathcal{D}|)$, a major modification being the additional `for` loop for scanning in the frequency domain. The second major modification is validating the presence of a fragment in line 6 in Algorithm 3. The improved model considers granularity in time and granularity in frequency. Let T_{frg} be the size of a fragment in time slots, T_{hdr} the size of a header in time slots, and F_{obw} the size of an OBW channel in frequency slots. The function `find` verifies the presence of a fragment or header in $\mathcal{M}_N$. The algorithm can determine between headers and fragments from p. Assuming the Coding Rate is known, the number of header replicas H_r is known, and then the frequency channel $s[p]$ corresponds to a header if $p \leq H_r$. Then, the function `find` function will verify if the block of size (T_{hdr}, F_{obw}) is present in $\mathcal{M}_N$ for each header and then it will verify if the block of size (T_{frg}, F_{obw}) is present in $\mathcal{M}_N$ for each fragment.

Payload Decoder

The Payload Decoder module is based on the traditional LR-FHSS decoder but with two different approaches. In addition to the data matrix $\mathcal{M}_N$ stored in the buffer memory, the module receives the set of transmissions with decoded headers $\mathcal{T}_S$ and an estimated set of transmissions with lost headers $\hat{\mathcal{T}}_C$. Therefore, information on the location of the payload fragments is available, and the remaining task is to retrieve the payload fragments from $\mathcal{M}_N$. The Payload Decoder can achieve this using two possible approaches.

Classic decoding The first decoding strategy is to retrieve the payloads associated with $\mathcal{T}_S$ only. This is the same as the original LR-FHSS decoder mechanism.

Thèse accessible à l'adresse : https://theses.insa-lyon.fr/publication/2026ISAL0011/these.pdf © [D. Maldonado Muñoz], [2026], INSA Lyon, tous droits réservés

Exhaustive decoding The second decoding strategy retrieves payloads associated with $\hat{\mathcal{T}}_C$. The proposed decoder design tries to decode with both coding rates CR1 and CR2, successfully retrieving every new payload fragment until the packet is decoded.

5.4 Evaluation

We conducted extensive computer simulations under a series of assumptions to validate the proposed Enhanced Decoder architecture. The main objective is to quantitatively determine the advantages of implementing the Enhanced LR-FHSS receiver to improve the overall throughput in any LR-FHSS network, terrestrial or space. The results presented in this section are based on the Collision-Centric model presented in Section 5.2.1.

The remainder of this section is organized as follows. First, the simulation environment and simulation parameters are presented. Then, the metrics used for evaluation are described. Lastly, the results are presented and analysed based on the modules of the Enhanced LR-FHSS Receiver.

5.4.1 Environment

The simulation environment comprises a specific simulator adapted to space and terrestrial LR-FHSS scenarios with realistic parameters and assumptions.

Simulator Our LR-FHSS network simulator is implemented in Python and available online [82]. Its main objective is to study collisions based on an abstraction of the physical layer. We represent each header and fragment as a squared signal in time-frequency dimensions. This approximation originates from the constant envelope signal transmitted by an LR-FHSS end device and its ultra-narrow band communication while considering a non-selective channel for each signal.

Scenarios The simulated LR-FHSS network comprises a single gateway receiving LR-FHSS transmissions from a population of end devices. The network module collects all frames, constructs a time-frequency matrix, accounting for Doppler effects, and delivers it to the gateway. The gateway then executes the decoding process. We consider two scenarios: space (satellite) and terrestrial. In the space scenario, the gateway is located on board the LEO satellite and the end devices are fixed on the ground, as in the DtS-IoT scenario shown in Figure 1.2. At the moment of transmission, each end device is located under the satellite's footprint, with a maximum distance of $D = 1500$ km. The gateway is static and located on the ground in the terrestrial scenario. This represents a generic terrestrial scenario without mobility and hence no Doppler shift. We opted not to specify further details, such as urban or rural environments, because this study focuses on the core mechanisms of headerless frame recovery and not on the specific propagation conditions of various terrestrial scenarios. This approach allows us to isolate the behaviour of LR-FHSS in a simplified setting, laying the groundwork for future studies that could examine more complex, location-specific conditions.

Parameters The simulation parameters are listed in Table 5.1. The number of transmissions varies between 10 and 1000 during the reception window. We use the parameters described by the LoRa Regional Parameters for the European Region [30]. Each end device chooses a random number of fragments to send at a random time, both values being uniformly distributed. An LR-FHSS fragment

Thèse accessible à l'adresse : https://theses.insa-lyon.fr/publication/2026ISAL0011/these.pdf © [D. Maldonado Muñoz], [2026], INSA Lyon, tous droits réservés

Table 5.1: Simulation Parameters

Carrier frequency f_c	868.1 MHz
OCW actual Bandwidth f^a_{ocw}	136.7 kHz
OCW RX Bandwidth f^r_{ocw}	200 kHz
OBW Bandwidth f_{obw}	488.28125 Hz
FHS set size S	384 sequences
Minimum Payload length P_{min}	8 fragments
Maximum Payload length P_{max}	31 fragments
Simulation time T	500 time slots
Fragment Time t_{frg}	102.4 ms
Header Time t_{hdr}	233.472 ms
Fragment Size T_{frg}	6 time slots
Header Size T_{hdr}	14 time slots
OBW Size F_{obw}	25 frequency slots
Coding Rate CR	CR1
Satellite altitude H	600 km
Maximum End-Device to Satellite Distance D	1500 km
End-device Antenna Gain G_t	2.5 dBi
Gateway Antenna Gain G_r	22.6 dBi
End-device Transmission Power P_t	14 dBm
Minimum SNR	10 dB
Time slot duration t_{frg}/T_{frg}	17 ms
Frequency slot size f_{obw}/F_{obw}	20 Hz

is equivalent to T_{frg} time slots, which results in a time slot of $t_{frg}/T_{frg} \approx 17$ ms, and each LR-FHSS header is equivalent to T_{hdr} time slots. Each OBW channel is subdivided into F_{obw} frequency slots, which results in a frequency slot of $f_{obw}/F_{obw} \approx 20$ Hz.

In our power-centric model, we assume that devices maintain line-of-sight communication with the satellite and that the receiver on the satellite has sufficient link budget to receive transmissions under these conditions successfully. All end devices use the same coding rate CR and transmission power P_t. All transmissions start and end during the simulation time T. This ensures that all frames are complete inside the sampled matrix $\mathcal{M}_N$.

The selection of the frequency slot size reflects a trade-off between model accuracy and computational complexity. From Figure 5.2, the maximum Doppler shift between fragments is approximately 25 Hz, based on a maximum Doppler Rate of 250 Hz/s. However, the Doppler shift between two consecutive fragments can be much smaller, meaning finer frequency slots would be necessary to capture the precise impact of the Doppler Rate during the transmission of an LR-FHSS packet. Although a frequency slot of 20 Hz does not fully capture the finer details of the Doppler Rate, the Doppler shift is still consistently present, and its behavior can be reliably predicted based on the satellite's altitude.

5.4.2 Metrics

Transmission Outcome The main metric we care to analyze is quantifying the possible LR-FHSS transmission outcomes. These are classified as follows:

n_1: Successfully decoded header and payload.

n_2: Successfully decoded header but collided payload.

Thèse accessible à l'adresse : https://theses.insa-lyon.fr/publication/2026ISAL0011/these.pdf © [D. Maldonado Muñoz], [2026], INSA Lyon, tous droits réservés

n_3: Collided header but retrievable payload.

n_4: Collided header and collided payload.

For a total number of transmissions $N = n_1 + n_2 + n_3 + n_4$, the number of transmissions for each outcome is noted as n_1, n_2, n_3 and n_4, respectively. Thus, the number of transmissions whose header is successfully decoded is represented by $S = n_1 + n_2$ while the number of transmissions whose header resulted in a collision is represented by $C = n_3 + n_4$. The usual decoding process of a traditional LR-FHSS receiver allows us to decode n_1 frames among S. We aim to quantify $n_1 + n_3$, which indicates the effectively decodable frames within N.

Channel Occupancy The channel occupancy measures the average usage of a large frequency band. The channel occupancy is calculated as the average usage of each OBW over a specific time window. We focus on an extended 200 kHz OCW reception window instead of the 137 kHz OCW transmission window to account for the spread due to the Doppler shift. The channel occupancy is calculated as in Eq. 5.4:

Channel occupancy is formally defined according to Equation 5.4:

$$\mathrm{occ}(M_N) = \mathrm{avg}(\mathrm{bin}(\mathcal{M}_N)), \tag{5.4}$$

where $\mathrm{bin}(\mathcal{M}_N)$ is the binarized version of the $\mathcal{M}_N$ matrix and $\mathrm{avg}()$ calculates the mean over the whole matrix.

F1 Score The F1 score is a metric commonly used in classification tasks. It combines both precision and recall into a single value, providing a balance between these two metrics. It is calculated as the harmonic mean, with equal weight, of precision and recall as follows:

$$F_1 = \frac{2 \times precision \times recall}{precision + recall}. \tag{5.5}$$

The precision measures the accuracy of optimistic predictions (true positives out of all predicted positives) as given by Eq. 5.6. In contrast, the recall identifies all relevant instances (true positives out of all actual positives) as given by Eq. 5.7. The F1 score ranges from 0 to 1, where 1 indicates perfect precision and recall, and 0 indicates poor performance. Specifically, precision and recall are defined as follows:

$$precision = \frac{tp}{tp + fp}, \tag{5.6}$$

$$recall = \frac{tp}{tp + fn}, \tag{5.7}$$

where tp are the true positives, fp are the false positives and fn are the false negatives.

Thèse accessible à l'adresse : https://theses.insa-lyon.fr/publication/2026ISAL0011/these.pdf © [D. Maldonado Muñoz], [2026], INSA Lyon, tous droits réservés

5.5 Results Analysis

5.5.1 Transmission Outcome

Figure 5.4 shows the statistics of the LR-FHSS transmission outcome for each space and terrestrial scenario. A traditional LR-FHSS receiver can only decode the frames with successful header and payload receptions. This is plotted in the blue curve labeled `decoded hdr & pld (n1)`. The green curve, labeled as `decodable pld (n3)`, represents the frames whose payload could have been retrieved by the legacy LR-FHSS receiver but are dropped due to missing header parts. The yellow curve, labeled as `decoded hdr (n2)`, represents the frames whose header part was successfully decoded but the payload decoding was unsuccessful due to collisions. Lastly, the red curve, labeled as `collided hdr & pld (n4)`, are the frames whose header and payload parts are collided.

Space Scenario The proposed enhanced LR-FHSS receiver can decode both frames and thus nearly double the decoding rate depending on how saturated the channel is. Results in Figure 5.4 show that the peak amount of decoded packets for the space scenario is 90 for 150 transmissions. Suppose the FHS Locator has a 100% success rate in finding all headerless packets. In that case, the decodable payloads may be added to the decoded packet, and the peak amount of the decoded packet would be 140, for a total of 200 transmissions. This represents an increase in the decoding rate of up to 50% in the space scenario.

Terrestrial Scenario On the other hand, the results for the terrestrial case in Figure 5.4 show that the peak number of decoded packets is 140, for a total of 250 transmissions. If the FHS Locator has a 100 % success rate, then the decodable payloads peak for a total decoded packets of 230 for 300 transmissions. This also represents a 50% increase in the terrestrial case.

Scenario Comparison It should be noted that up to 60 % more frames can be decoded in the terrestrial scenario compared to the space scenario. This difference is attributed to the higher collision probability in the space scenario, where the high absolute Doppler shift increases the likelihood of frame collisions. While the variation of the frequency shift within a single LR-FHSS packet is negligible, the cumulative effect of the Doppler shift across multiple packets significantly impacts collision rates in the space scenario.

5.5.2 FHS Locator

Figure 5.5 shows the results of the Locator modules implementing the Exhaustive FHS search Algorithm 4 in terms of true positives tp, false positives fp and false negatives fn.

The figure presents space and terrestrial simulations. Note that the fluctuations observed in the plots are a product of the inherent randomness in the simulations, with ten iterations per data point. Despite this variability, the overall trends are consistent, providing reliable insights into performance.

Space Scenario The estimation of C is given by $\hat{C} = tp + fp$. The $\hat{C}$ estimation almost matches C up to 800 transmissions in the space use case. This is due to the low false positive and false negative rates. The explanation is that the additional frequency shift dimension makes LR-FHSS transmissions

Thèse accessible à l'adresse : https://theses.insa-lyon.fr/publication/2026ISAL0011/these.pdf © [D. Maldonado Muñoz], [2026], INSA Lyon, tous droits réservés

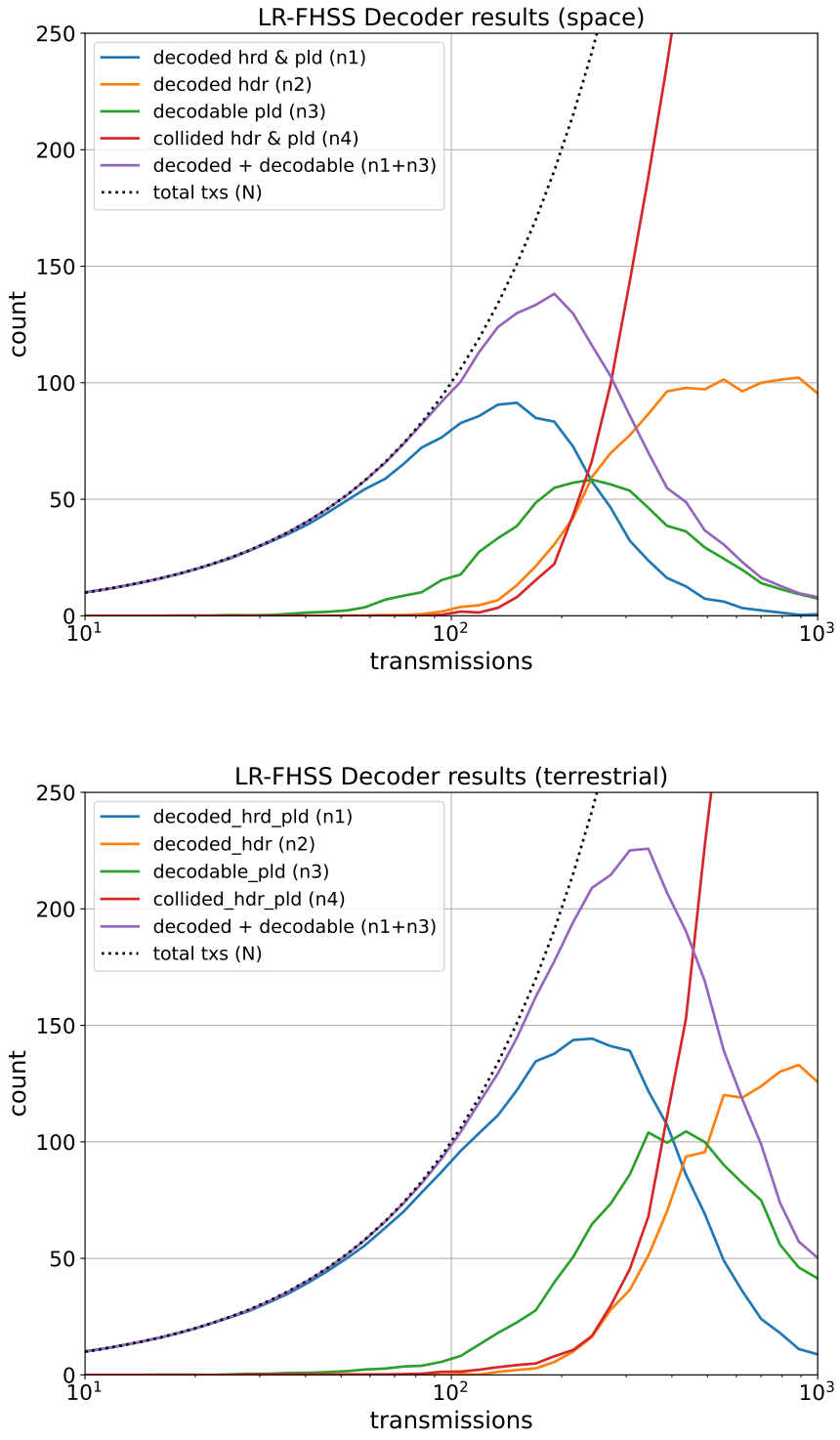


Figure 5.4: LR-FHSS Decoder transmission outcome statistics for satellite (top) and terrestrial (bottom) deployment scenarios.

Thèse accessible à l'adresse : https://theses.insa-lyon.fr/publication/2026ISAL0011/these.pdf © [D. Maldonado Muñoz], [2026], INSA Lyon, tous droits réservés

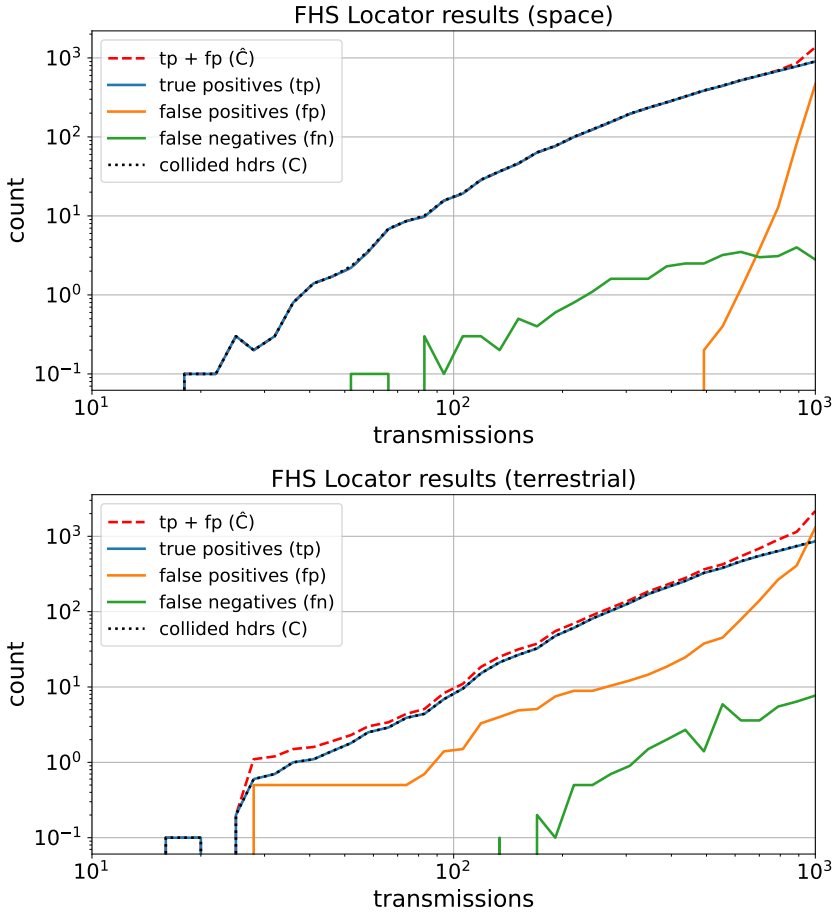


Figure 5.5: FHS Locator classification performance for satellite (top) and terrestrial (bottom) deployment scenarios.

unique. Even if two transmissions choose the same sequence and transmit simultaneously, it is still improbable that they would be generated by nearby end devices, thus having a similar Doppler Shift. However, as mentioned, the higher dimensionality increases the algorithm complexity and, thus, the search time.

Terrestrial Scenario In the terrestrial case, a slight increase in the false positive rate can be noted while the false negative rate remains low. Overall, the estimation $\hat{C} = tp + fp$ always contains some false positives in the terrestrial scenario. However, the FHS Locator search algorithm for the terrestrial scenario is faster to execute due to the lower complexity. Attempting to decode false positives hinders the enhanced receiver's overall performance of the decoding process. Thus, the FHS Locator should not be applied in cases where the false positive rate is too high concerning the target C.

Scenario Comparison The results prove the proposed approach's effectiveness in finding nearly all sequences with high tp and low fn and fp rates. However, in the terrestrial case, the inability to differentiate frames using the Doppler reading causes a steep increase in false positives. This suggests that the space scenario allows our headerless decoding scheme to provide its best decoding gain. This is crucial as the space scenario poses the largest scalability challenges. We can also notice that in both scenarios, there are no collisions for small end-device populations (up to 20 end-devices). The difference matrix $\mathcal{M}_C$, computed as explained in 5.3.2, is then empty. In this case, the FHS Locator algorithm is not executed, and this module has no output data. Therefore, some

Thèse accessible à l'adresse : https://theses.insa-lyon.fr/publication/2026ISAL0011/these.pdf © [D. Maldonado Muñoz], [2026], INSA Lyon, tous droits réservés

blank spaces can be seen at the beginning of the plots showing results from this module.

5.5.3 F1 Score

The classification performance is better appreciated with the F1 score. Figure 5.6 shows the F1 score metric for the space scenario on top and the terrestrial scenario on the bottom. Note that the F1 score is introduced to evaluate the classification accuracy of our enhanced receiver's headerless decoding mechanism. It serves as a benchmark for assessing the receiver's ability to correctly identify and decode frames, laying the foundation for future comparisons with alternative headless recovery mechanisms.

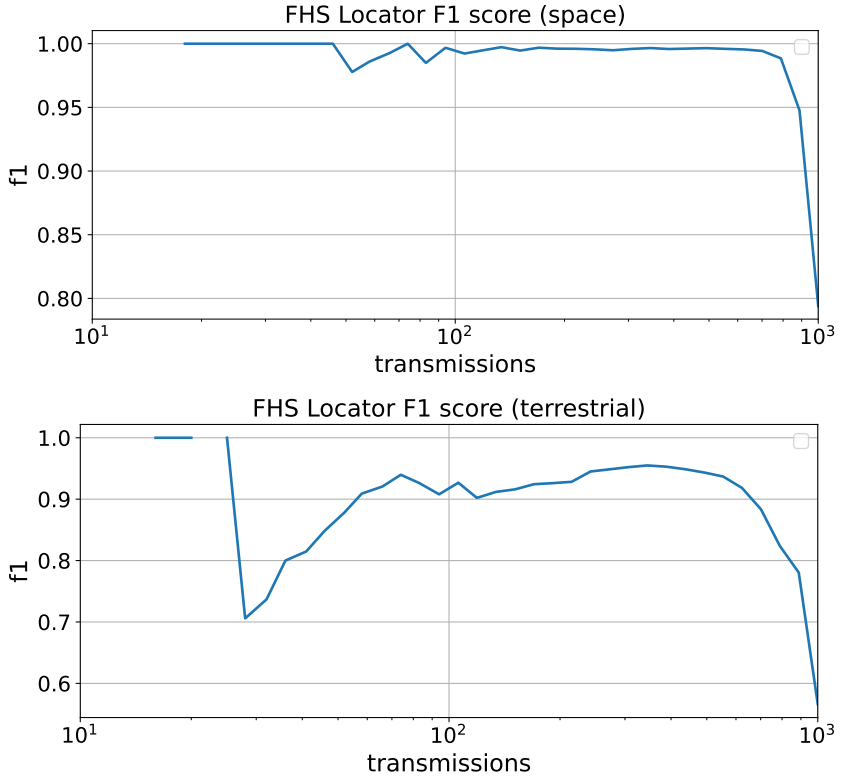


Figure 5.6: FHS Locator F1 score classification performance for satellite (top) and terrestrial (bottom) deployment scenarios.

Space Scenario For the space scenario, the F1 score remains close to 1 when the number of transmissions is below 800 transmissions, indicating a near-perfect classifier, and decreases after. This is verified when comparing the F1 score curve with the false positive rate from figure 5.5 (top).

Terrestrial Scenario On the other hand, the F1 score for the terrestrial scenario is lower, a direct consequence of the lower performance of the FHS Locator module. Moreover, the F1 score decreases exponentially after 600 transmissions. This can also be verified when comparing with the false positive rate from figure 5.5 (bottom). The sudden drop of the F1 score at 30 transmissions can be explained by false positives, as seen in the false positive rate from figure 5.5 (bottom).

Thèse accessible à l'adresse : https://theses.insa-lyon.fr/publication/2026ISAL0011/these.pdf © [D. Maldonado Muñoz], [2026], INSA Lyon, tous droits réservés

Scenario Comparison The comparison of both scenarios shows how the extra variable of the frequency shift helps the FHS locator rule out false positives. Hence, the FHS Locator module for the space scenario performs better.

5.5.4 Channel Occupancy

We propose to evaluate the channel occupancy, as described in Section 5.4.2, to determine how the enhanced receiver fairs compared to the legacy receiver regarding the estimation of the number of headerless frames $\hat{C}$.

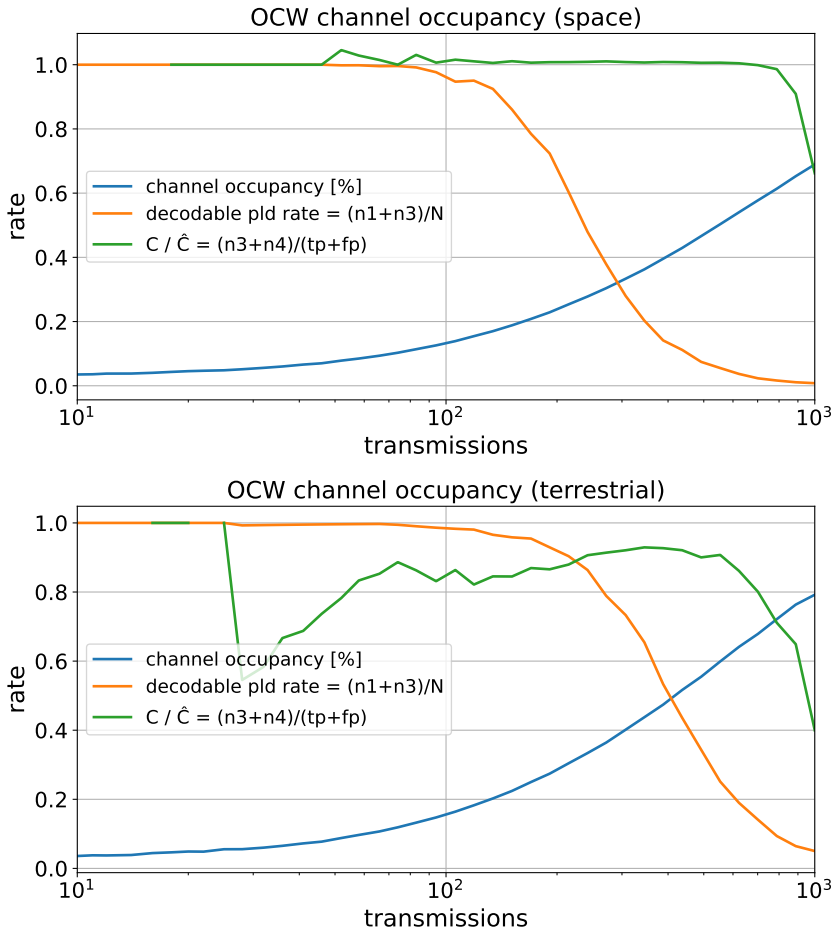


Figure 5.7: Channel occupancy characteristics for satellite (top) and terrestrial (bottom) deployment scenarios.

Space Scenario On the top side of Figure 5.7, we show the measured channel occupancy rate compared with the retrievable payload rate $(n_1+n_3)/N$ and the collided header estimation ratio $C/\hat{C}$. The ratio $C/\hat{C}$ is close to one until around 800 transmissions, at which point the retrievable payload rate is around 2%, and the channel occupancy is around 60%. Setting a threshold for considering the results given by the FHS Locator may also help improve the enhanced receiver's efficiency when the extra decoded payload does not justify executing the whole process. This threshold largely depends on the platform computing capabilities and the data value according to the application of the LR-FHSS network. Moreover, the receive window sampled into M_S is just a fraction of the coverage time for LEO satellite support, which can be around 10 minutes, depending on the elevation angle. Since the FHS locator functionality is limited to short reception windows, multiple snapshots would be retrieved

Thèse accessible à l'adresse : https://theses.insa-lyon.fr/publication/2026ISAL0011/these.pdf © [D. Maldonado Muñoz], [2026], INSA Lyon, tous droits réservés

over all the available OCW channels for a complete satellite pass. The small sub-estimation of C seen between 50 and 80 transmissions is explained by the false positives as seen in the false positives curve from Figure 5.5 (top).

Terrestrial Scenario On the bottom of Figure 5.7, it is observed how the estimation of the number of headerless packets $\hat{C}$ deviates from the target C due to the higher false positive rate. Nevertheless, the estimation remains accurate to about 80% for most end device populations before the channel becomes saturated at around 500 end devices.

Scenario Comparison The pessimistic collision model produces more collision in the terrestrial scenario. This can be noted when comparing the retrievable payload rate for both cases. The estimation $\hat{C}$ of the real amount of headerless packets is closer to its target C for the space scenario.

The results presented in this section strongly support the implementation of the proposed Enhanced LR-FHSS decoder, which would increase the frame decoding rate in any scenario, including terrestrial and space LR-FHSS networks.

5.6 Conclusion

This chapter introduces a novel Enhanced LR-FHSS Decoder architecture for recovering headerless frames, significantly improving the performance of space-terrestrial integrated IoT networks. Our extensive simulations demonstrate that the enhanced decoder can increase the packet delivery ratio by up to 50% in both terrestrial and satellite scenarios. This improvement is crucial for DtS-IoT networks, where high collision rates often lead to substantial data loss.

Key results and observations include:

- Doppler Effect Consideration: By incorporating Doppler compensation techniques, our enhanced decoder effectively profits from the frequency shifts inherent in LEO satellite communications to ensure a more reliable frame recovery.
- FHS Locator Accuracy: The proposed FHS Locator module accurately identifies headerless frames, maintaining a near-perfect F1 score in low to moderate transmission densities.
- Scalability: The enhanced decoder proves particularly beneficial in high-density and highly dynamic satellite IoT scenarios, where traditional LR-FHSS receivers struggle.
- Realistic Channel Modeling: By simulating realistic space-terrestrial communication environments, including variable payload sizes and partial header losses, we validated the robustness and adaptability of our enhanced decoder under practical conditions.

These advancements lay a solid foundation for the next generation of scalable and efficient space-terrestrial integrated IoT networks based in LR-FHSS, promising substantial improvements in communication reliability and network performance.

Further research will explore advanced collision determination techniques and adaptive decoding strategies to maximize the potential of LR-FHSS networks. Additionally, we plan to investigate

Thèse accessible à l'adresse : https://theses.insa-lyon.fr/publication/2026ISAL0011/these.pdf © [D. Maldonado Muñoz], [2026], INSA Lyon, tous droits réservés

collaborative headerless decoding among multiple receiving gateways, each perceiving a different Doppler profile.

As a next step, we aim to explore the possibility of conducting experiments with LR-FHSS frames, either from ground-based testbeds or from real satellites, as opportunities arise, to further validate the Enhanced LR-FHSS Receiver with real-world data, though access to such resources remains a significant challenge.

Thèse accessible à l'adresse : https://theses.insa-lyon.fr/publication/2026ISAL0011/these.pdf © [D. Maldonado Muñoz], [2026], INSA Lyon, tous droits réservés

Thèse accessible à l'adresse : https://theses.insa-lyon.fr/publication/2026ISAL0011/these.pdf © [D. Maldonado Muñoz], [2026], INSA Lyon, tous droits réservés

Chapter 6

Coordination

Along with LR-FHSS, another key enabler of efficient DtS operation is the accurate prediction of satellite visibility at the device. Ephemeris-based prediction (e.g., SGP4), combined with relaxed update periodicity and adaptive guard-time policies, has been shown to enable reliable timing and battery savings, as validated on real CubeSat links [93, 94]. When orbital data is unavailable, Doppler-only inference from downlink beacons can reconstruct orbital parameters with sufficient accuracy to recover pass times [95]. As illustrated in Fig. 6.1, these approaches allow LoRa/LR-FHSS devices to anticipate elevation-dependent link conditions, enabling informed resource allocation under DtS intermittency.

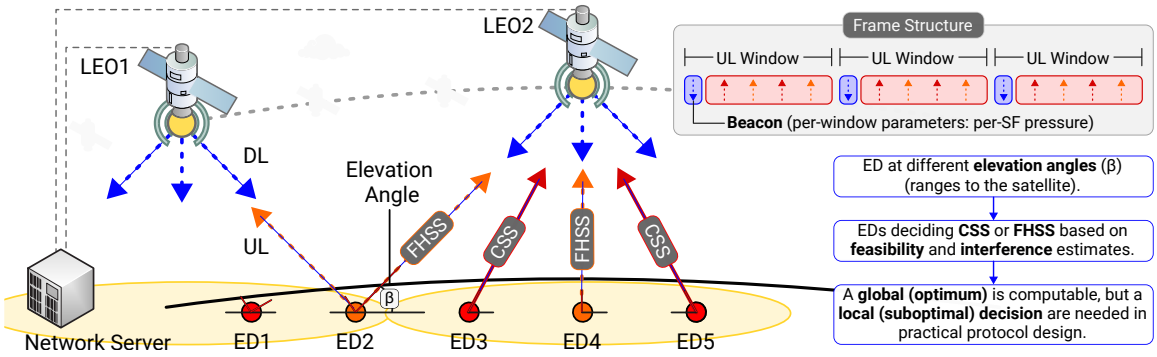


Figure 6.1: System model for the DtS-IoT scenario. LEO satellites broadcast LoRa downlink beacons at the beginning of each UL window, providing per-SF interference indicators. End-devices (ED1–ED5) at different elevation angles select either LoRa CSS or LR-FHSS for uplink transmission based on feasibility and load estimates. While a global optimum exists, each device must make a local, suboptimal decision compatible with practical DtS-IoT constraints.

In this work, we address the scalability limitations of DtS-IoT networks by jointly exploiting LoRa and LR-FHSS, and by designing practical, low-signaling wireless access schemes that remain feasible for constrained devices. Our approach integrates visibility-aware per-device feasibility (derived from link budget and Doppler constraints) and lightweight interference awareness informed by the satellite, compared with optimal allocation models that serve as theoretical performance envelopes. Using a LEO multi-satellite scenario over continental France—chosen, without loss of generality, as a representative large-scale DtS-IoT region—we provide the first detailed comparison between joint LoRa/LR-FHSS strategies and their optimal scheduling baselines.

Thèse accessible à l'adresse : https://theses.insa-lyon.fr/publication/2026ISAL0011/these.pdf © [D. Maldonado Muñoz], [2026], INSA Lyon, tous droits réservés

6.1 Transmission Control Models

6.1.1 LoRa success probability based control

The probability that no portion of the packet transmitted with SF m by the generic node is interfered with, P_{S}, was studied in [96] and given as,

$$P_{\mathrm{S}}(m) = e^{-4vLt_m\lambda}, \tag{6.1}$$

where L is the deployment area size, t_m is the frame duration which depends on SF m, v is the satellite speed and λ is the device density. This equation can be inverted to obtain the maximum number of interfering devices, such that a given threshold for the minimum desired success probability $P_{\min}$ is ensured. Consider a fixed deployment region with surface area A, then $\lambda = \frac{N}{A}$, where N is the number of interfering devices. Then, the maximum number of interfering devices under $P_{\min}$ is given by,

$$N_{\max}(P_{\min}, m) = \frac{-A \cdot \ln(P_{\min})}{4vLt_m}. \tag{6.2}$$

6.1.2 ALOHA maximum throughput based control

The throughput of the pure ALOHA protocol is given by $S = G \cdot e^{-2G}$, where G represents the average number of transmission attempts per frame time. The maximum throughput is achieved when $G = 0.5$. Channel load G can be expressed as $G = \frac{t_m N}{T}$, where T is the uplink window size, t_m is the frame duration which depends on SF m, and N is the number of competing devices. Thus, to maximize throughput, the optimal number of competing devices $\bar{N_m}$ is given by,

$$\bar{N}_m = \frac{T}{2t_m}. \tag{6.3}$$

6.1.3 Coding Rate allocation for LR-FHSS

An intelligent yet simple approach to deciding which Coding Rate (CR) to use for LR-FHSS is to allocate CR2/3 to devices closer to the satellite. Based on the capture effect, there is a higher probability of decoding a header/fragment suffering from a collision if its Signal-to-Interference Ratio (SIR) is higher than a given threshold ψ. Semtech has not explicitly disclosed the exact value of ψ, while some research works on LR-FHSS assume $\psi = 6$ dB [77, 97].

The CR allocation strategy proposed in this work is to use CR1/3 for devices farther from the satellite, while devices closer to the satellite shall use CR2/3. The coverage region is determined by the minimum elevation angle $\alpha_{\min}$. This region is divided into two regions of equal surface area, each containing approximately the same number of devices. The elevation angle β corresponds to the dividing angle between $\alpha_{\min}$ and 90.

We define $\mathcal{C} = \{\text{CR1/3}, \text{CR2/3}\}$ as the set of available CR for LR-FHSS. Then, we define the β-allocation strategy for choosing CRs based on the β angle, while the selection of the Occupied

Thèse accessible à l'adresse : https://theses.insa-lyon.fr/publication/2026ISAL0011/these.pdf © [D. Maldonado Muñoz], [2026], INSA Lyon, tous droits réservés

Channel Width (OCW) frequency channel for LR-FHSS is random.

6.2 Optimal LoRa Allocation Models

6.2.1 On the δ variable calculation

Link budget, Doppler Shift, and Rate are critical to both LoRa and LR-FHSS. Satellite orbits can be projected in time, and, assuming fixed ground-based devices, link conditions can be predicted. We define the $\delta_{n,m,t}$ binary variable, which indicates whether a transmission from device n using SF m can be successfully received by the satellite at time t, given Link Budget and Doppler Effect limitations. Calculating δ for long periods and large networks is computationally intensive and should be done on the ground at the network server. We use this variable to simplify the optimal allocation models defined in this section.

We also define, for convenience, $m = 6$ as the LR-FHSS availability, given that both CRs have the same Link Budget and Doppler Effect. Semtech reports that LR-FHSS has a similar Link Budget to SF12 [31].

For the joint distribution strategies defined in Section 6.3, we assume each device is capable of obtaining its own calculation of the δ variable by some of the lightweight orbit prediction methods proposed in the state-of-the-art [93, 94, 95]. The details of the orbit predictions methods fall outside of the scope of this thesis.

This section presents our first contribution: a centralized LoRa optimal allocation method that will serve as a performance upper bound by computing the maximum achievable performance in the DtS uplink. We formulate two complementary models: a full 2-D time–frequency strip packing problem, and a tractable sequential 1-D variant, that assume perfect global knowledge of all devices, their admissible transmission slots, and the complete interference structure. These models serve as theoretical optimums that no real distributed protocol can surpass, and as reference schedules against which the practical MAC schemes of Section 6.3 are evaluated.

6.2.2 2D Strip packing Model

The 2D strip packing model treats the resource allocation problem as a bin-packing optimization, allocating time and frequency resources simultaneously. Our model draws inspiration from the two-dimensional formulation introduced in [98]. The motivation for using this model is based on CSS modulation. A LoRa frame can be represented by a rectangle in the time-frequency dimension, where the bandwidth is fixed, and channels are assumed to be adjacent and non-overlapping. On the other hand, the time-on-air (ToA) corresponds to the size in the time dimension.

The inputs of the problem are as follows:

- N is the number of devices and $\mathcal{N}$ is the set of devices.
- $M = 6$ is the number of SFs, where $\mathcal{M} = \{0, 1, 2, 3, 4, 5\}$ is the set of available SFs. We use a convenient re-indexing for the mathematical model, where 0 corresponds to SF7 and so on.
- T and F are the total number of time slots and frequency channels, respectively, where

Thèse accessible à l'adresse : https://theses.insa-lyon.fr/publication/2026ISAL0011/these.pdf © [D. Maldonado Muñoz], [2026], INSA Lyon, tous droits réservés

$\mathcal{T} = \{0, 1, \ldots, T-1\}$ is the set of time slots, and $\mathcal{F} = \{0, 1, \ldots, F-1\}$ is the set of available LoRa frequency channels.

- $\mathcal{I} = \{0, 1, \ldots, MN-1\}$ is the set of all possible MN frames, representing all SFs for all devices. Each frame $i_{n,m} = n + mN$ corresponds to a LoRa transmission from device n using SF m. Hence, the first N items correspond to an SF7 transmission from each device, the next N to an SF8 transmission, and so on until SF12. Hereafter, $i_{n,m}$ is simply noted as i.
- w_i is the ToA of frame i in terms of time slots.
- $B_i = 1$ is the bandwidth of frame i.
- d_i is the value of frame $i \in \mathcal{I}$. The value of a frame is defined as its total payload bytes.

The binary variables of the optimization problem are $x_{i,t,f} \in \{0, 1\}$, which indicate whether frame i is placed at point $(t, f) \in \mathcal{T} \times \mathcal{F}$. It is considered that a frame i is placed at (t, f) if transmission starts at time slot t on channel f.

To simplify the derivation of the problem constraints, we introduce the following definitions:

- Variable $\delta_{i,t} \in \{0, 1\}$ indicates if frame i can be placed at (t, f), for any $f \in \mathcal{F}$, considering link budget and Doppler constraints.
- Set $\xi_{t,f,m} = \{(i, a, b) \mid i \in \mathcal{I}, (t, f) \in \mathcal{T} \times \mathcal{F}, a \leq t \leq a + t_i \wedge b = f \wedge \lfloor \frac{i}{N} \rfloor = m\}$ that contains all possible frames and positions such that, if frame i is placed at (a, b), it covers point (t, f), and also if $\lfloor \frac{i}{N} \rfloor = m$, meaning it considers only items with the same SF m. It is assumed that a frame i covers a point (t, f) when it is placed at a position (a, b) such that $(t, f) \in [a, a + t_i] \times [b]$.
- Set $\psi_{t,f} = \bigcup_{m \in \mathcal{M}} \xi_{t,f,m}$ that contains all possible items and positions such that, if the frame is placed in this position, it covers point (t, f), regardless of the SF.
- Set $\phi_t = \bigcup_{f \in \mathcal{F}} \psi_{t,f}$ that contains all possible items and positions such that, if the frame is placed in this position, it covers the point (t, f), for any f.

Given the variables and inputs, the objective of Problem (P-2D) is to maximize the sum of values and relationships between items that are packed in the bin, which can be formulated as,

$$\text{maximize} \quad \sum_{i \in \mathcal{I}} \sum_{t,f \in \mathcal{T} \times \mathcal{F}} x_{i,t,f} d_i \tag{P-2D}$$

$$\text{subject to} \quad \sum_{m \in \mathcal{M}} \sum_{t,f \in \mathcal{T} \times \mathcal{F}} x_{i_{n,m},t,f} \leq 1, \quad \forall n \in \mathcal{N} \tag{6.4}$$

$$\sum_{(i,a,b) \in \psi_{t,f}} x_{i,a,b} \leq M, \quad \forall t, f \in \mathcal{T} \times \mathcal{F} \tag{6.5}$$

$$\sum_{(i,a,b) \in \xi_{t,f,m}} x_{i,a,b} \leq 1, \quad \forall t, f \in \mathcal{T} \times \mathcal{F}, m \in \mathcal{M} \tag{6.6}$$

$$\sum_{(i,a,b) \in \phi_t} x_{i,a,b} \leq D, \quad \forall t \in \mathcal{T} \tag{6.7}$$

$$x_{i,t,f} \leq \delta_{i,t}, \quad \forall t, f \in \mathcal{T} \times \mathcal{F}, i \in \mathcal{I} \tag{6.8}$$

Thèse accessible à l'adresse : https://theses.insa-lyon.fr/publication/2026ISAL0011/these.pdf © [D. Maldonado Muñoz], [2026], INSA Lyon, tous droits réservés

Constraint (6.4) imposes that a device can only transmit once during this time window $\mathcal{T}$, regardless of the SF. Constraint (6.5) allows up to M concurrent transmissions, reflecting the quasi-SF orthogonality, while constraint (6.6) restricts concurrent transmissions with the same SF. Constraint (6.7) reflects the simultaneous reception limit for LoRa gateways, with up to D incoming concurrent transmissions. Typical values for D are 8 or 16 [39].

Lastly, constraint (6.8) represents the Link Budget and Doppler constraints by means of variable $\delta_{i,t}$.

6.2.3 1D Packing Model with Sequential Channel Allocation

Recognizing the computational complexity of the 2D model, a simplified 1D approach is proposed that allocates resources sequentially across multiple frequency channels. This model reduces complexity while maintaining near-optimal performance by intelligently ordering channels.

The 1D model recycles the definitions of the 2D model presented in Section 6.2.2. The optimization variables of this simplified problem become $y_{i,t} \in \{0, 1\}$, indicating whether frame i is placed at $t \in \mathcal{T}$.

Given the variables and inputs, the objective of Problem (P-1D) is now to maximize the sum of values and relationships between frames that are packed in the bin, expressed as,

$$\text{maximize} \quad \sum_{i\in\mathcal{I}}\sum_{t\in\mathcal{T}} y_{i,t}d_i \tag{P-1D}$$

$$\text{subject to} \quad \sum_{m\in\mathcal{M}}\sum_{t\in\mathcal{T}} y_{i_{n,m},t} \leq 1, \quad \forall n \tag{6.9}$$

$$\sum_{(i,a)\in\psi_t} y_{i,a} \leq M, \quad \forall t \tag{6.10}$$

$$\sum_{(i,a)\in\xi_{t,m}} y_{i,a} \leq 1, \quad \forall t, \forall m \tag{6.11}$$

$$\Psi_t + \sum_{(i,a)\in\psi_t} y_{i,a} \leq D, \quad \forall t \tag{6.12}$$

$$y_{i,t} \leq \delta_{i,t}, \quad \forall t, \forall i \tag{6.13}$$

Similarly to the 2D case, constraints are simplified by omitting the frequency dimension. The variable $\delta_{i,t}$ remains the same, and the other constraints are redefined as follows,

- Set $\xi_{t,m} = \{(i, a) \mid i \in I, a \in \mathcal{T}, a \leq t \leq a + t_i \wedge \lfloor \frac{i}{N} \rfloor = m\}$ is equivalent to $\xi_{t,f,m}$.
- Set $\psi_t = \bigcup_{m\in\mathcal{M}} \xi_{t,m}$ is equivalent to $\psi_{t,f}$.
- Array $\Psi_t \in \mathbb{N}^T$ represents the number of transmissions occurring at any $t \in \mathcal{T}$. It starts with all zero values and is updated each time the 1D problem is solved to constrain the number of simultaneous transmissions across all available channels.

Constraints (6.9)-(6.13) are similar to their original counterparts (6.4)-(6.8), except that they only concern the time slot dimension, instead of both the time slot and frequency channel dimensions as

Thèse accessible à l'adresse : https://theses.insa-lyon.fr/publication/2026ISAL0011/these.pdf © [D. Maldonado Muñoz], [2026], INSA Lyon, tous droits réservés

in Problem (P-2D). It is worth noting that the demodulator limitation constraint is still enforced through Eq. (6.12).

The multiple-channel schedule x is obtained by solving the 1D model for each channel f while updating the model variables δ and Ψ at each iteration over channels. Variable δ is used to avoid the allocation of previously allocated frames. If a frame j was allocated, this is $y_{j,t} = 1$ for any $t \in \mathcal{T}$, then $\delta_{j,t} = 0, \forall t \in \mathcal{T}$. Variable Ψ is updated by considering each schedule such that $y_{i,t} = 1$.

6.3 Distributed Joint LoRa/LR-FHSS Protocols

This section introduces our second contribution: a family of distributed joint LoRa/LR-FHSS MAC protocols that operate without centralized coordination and rely solely on local device computation and a lightweight beacon broadcast by the satellite. In contrast to the optimized method of Section 6.2, these schemes do not attempt complete scheduling; instead, they exploit visibility-derived feasibility, probabilistic load control, and the joint use of LoRa and LR-FHSS to approximate near-optimal performance under realistic DtS constraints. These protocols are compliant with LoRaWAN Class A and B and are evaluated against the centralized bound in Section 6.4.

6.3.1 Extending LoRaWAN Class A

There is currently no algorithm for choosing between LoRa and LR-FHSS. We initially consider a 50/50 split between LoRA and LR-FHSS. Moreover, finding the parameters for LoRa (SF) or LR-FHSS (CR) is not trivial, as the Adaptive Data Rate (ADR) cannot be used in our scenario with fast-moving satellites. We consider a case where the parameters are chosen randomly. We define then the *Joint-Class A* allocation strategy. The transmission time slot is selected uniformly at random, as well as a uniform random frequency channel f LoRa and/or a random OCW f_{ocw} for LR-FHSS. When using LoRa, a random SF m is selected uniformly from all available SFs. For LR-FHSS, a random CR c is selected. The result of the allocation process is a tuple (n, m, t, f), where n is the device ID, m (c) is the SF (CR) for LoRa (LR-FHSS), t is the transmission time, and f (f_{ocw}) is the frequency channel.

6.3.2 Proposed Satellite-Aware MAC

This category of MAC protocols assumes that devices can track the satellite's position. Namely, each device is assumed to be capable of calculating its visibility window and channel condition, thus, having its own calculation of the δ variable discussed in Section 6.2.1.

For each device n, we define:

- $\mathcal{M}_{\text{avail}} = \{m \mid \exists\, t \text{ such that } \delta_{n,m,t} > 0\}$, the set of available SFs at any time.
- $\mathcal{T}_m = \{t \mid \delta_{n,m,t} = 1\}$, the set of available time slots for $m \in \{0, 1, 2, 3, 4, 5\}$.
- $\bar{m} = \min\{m \mid \exists\, t \text{ such that } \delta_{n,m,t} > 0\}$, the lowest SF achieved.

Thèse accessible à l'adresse : https://theses.insa-lyon.fr/publication/2026ISAL0011/these.pdf © [D. Maldonado Muñoz], [2026], INSA Lyon, tous droits réservés

Algorithm 5: Joint Class A Valid-SF

Data: δ
Result: List of allocated transmissions txs
Initialize $txs \leftarrow [\,]$;
for *each device* n **do**
  $\epsilon \sim \mathcal{U}(0,1)$;
  if $\epsilon < 0.5 \wedge \mathcal{M}_{\text{avail}} \neq \emptyset$ **then** `// use LoRa`
    $m \leftarrow$ Uniform($\mathcal{M}_{\text{avail}}$);
    $t \leftarrow$ Uniform($\mathcal{T}_m$);
    $f \leftarrow$ Uniform($\mathcal{F}$);
    Add (n, m, t, f) to txs;
  else `// use LR-FHSS`
    $c \leftarrow \beta$-allocation($\mathcal{C}$);
    $t \leftarrow$ Uniform($\mathcal{T}_6$);
    $f_{\text{ocw}} \leftarrow$ Uniform($\mathcal{OCW}$);
    Add $(n, c, t, f_{\text{ocw}})$ to txs;
  end
end
return txs

Joint Class A Valid-SF

An immediate upgrade to the *Joint Class A* is to use an SF known to be supported. Alg. 5 describes this improved protocol. This strategy is named *Joint-Class A Valid-SF*. The key difference with the *Joint-Class A* is that the SF is selected from $\mathcal{M}_{\text{avail}}$, and the transmission time from $\mathcal{T}_m$ in the case of using LoRa. If using LR-FHSS, the CR is selected following the β-allocation, discussed in Section 6.1.3, and the transmission time is chosen from $\mathcal{T}_6$ ($m = 6$ is defined as LR-FHSS). From here on, we define Uniform(X) as the random selection of an item from set X.

ALOHA maximum throughput strategy

We define a new strategy named *ALOHA Best-SF* based on the maximum theoretical throughput for the ALOHA protocol. A simple yet effective strategy is to allow only $\bar{N}$ devices to use LoRa with a selected SF m, as in Eq. (6.3). By default, each device selects the lowest SF it can achieve, $\bar{m}$. Then, each device decides whether to allocate a LoRa transmission using SF $\bar{m}$ based on the total network size N, such that on average only $\bar{N}_{\bar{m}}$ devices use LoRa. If the device fails to obtain the LoRa allocation, it will schedule an LR-FHSS transmission with a random CR. The *ALOHA Best-SF* is described in Alg. 6.

6.3.3 Proposed Satellite & Interference Aware MAC

Periodic beacons can be used to inform devices of the satellite's presence in LoRaWAN Class B. A more general protocol that uses uplink windows with a defined duration can leverage this beacon to transmit valuable data to devices. For each uplink window, it is possible to calculate the number of devices C_m attempting to use SF m, for each $m \in \mathcal{M}$, assuming devices will always attempt to use the lowest SF available. We refer to C_m as the competitors for SF m. This information can be

Thèse accessible à l'adresse : https://theses.insa-lyon.fr/publication/2026ISAL0011/these.pdf © [D. Maldonado Muñoz], [2026], INSA Lyon, tous droits réservés

Algorithm 6: ALOHA Best-SF

Data: δ, N
Result: List of allocated transmissions txs

Initialize $txs \leftarrow [\,]$;
for *each device* n **do**
  $\bar{m} = \min\{m \mid \exists\, t \text{ such that } \delta_{n,m,t} > 0\}$;
  if $\bar{m} \notin \mathcal{M} \bigcup \mathcal{C}$ **then**
    continue `// Skip unsupported device`
  end
  $P_{\mathrm{TX}} \leftarrow \mathsf{min}\big(1, \bar{N}_m/N\big)$;
  $\epsilon \sim \mathcal{U}(0,1)$;
  if $\bar{m} \in \mathcal{M} \wedge \epsilon < P_{\mathrm{TX}}$ **then**
    $t \leftarrow \mathsf{Uniform}(\mathcal{T}_{\bar{m}})$;
    $f \leftarrow \mathsf{Uniform}(\mathcal{F})$;
    Add $(n, \bar{m}, t, f)$ to txs;
  else `// use LR-FHSS`
    $c \leftarrow \beta$-$\mathsf{allocation}(\mathcal{C})$;
    $t \leftarrow \mathsf{Uniform}(\mathcal{T}_6)$;
    $f_{\mathrm{ocw}} \leftarrow \mathsf{Uniform}(\mathcal{OCW})$;
    Add $(n, c, t, f_{\mathrm{ocw}})$ to txs;
  end
end
return txs

calculated on board if the satellite has sufficient computational resources, or on the network server and uploaded to the satellite at a previous phase.

Success Best-SF

This strategy is based on the success probability function presented in Eq. (6.1). Given a threshold $P_{\min}$ representing the minimum desired success probability, the maximum number of transmissions $N_{\max}$ can be obtained. Then, an allocation strategy is designed so that, on average, there are $N_{\max}$ LoRa frames. The number of competitors for each SF is packed within the beacon and broadcast by the satellite at the beginning of the uplink window.

It is calculated as follows:

$$C_m = \sum_{n=1}^{N} \left\lceil \max_{t \in T} \delta_{n,m,t} \right\rceil . \tag{6.14}$$

The *Success Best-SF* strategy is almost identical to the *ALOHA Best-SF* strategy defined in Alg. 6. The key difference is the transmission control threshold P_{TX} now based on the success probability function as follows:

$$P_{\mathrm{TX}} = N_{\max}(P_{\min}, \bar{m})/C_{\bar{m}} \tag{6.15}$$

Thèse accessible à l'adresse : https://theses.insa-lyon.fr/publication/2026ISAL0011/these.pdf © [D. Maldonado Muñoz], [2026], INSA Lyon, tous droits réservés

Success-based sequential SF allocation

An alternative to the previous method is to assign the SF sequentially. Instead of using LR-FHSS after a failed LoRa allocation with the lowest SF $\bar{m}$, the device will attempt to allocate a LoRa frame with SF $\bar{m}+1$. The process is repeated until reaching SF12 ($m=5$). If LoRa allocation fails again, LR-FHSS will be used. This sequential approach will increase the number of competitors for higher SFs. Thus, we define the cumulative number of expected competitors $C_m^{\text{cum}} = \sum_{i=0}^{m} C_i$, where C_i is the number of competitors using SF i. The *Success Seq-SF* strategy is described in Alg. 7.

Algorithm 7: Success Seq-SF

Data: δ, $P_{\min}$, C_m
Result: List of allocated transmissions txs

Initialize $txs \leftarrow [\,]$;
for *each device* n **do**
  if $\bar{m} \notin \mathcal{M} \bigcup \mathcal{C}$ **then**
    continue `// Skip unsupported device`
  end
  $usedLoRa \leftarrow false$;
  while $\bar{m} \leq 5 \wedge$ *not* $used_LoRa$ **do**
    $P_{\text{TX}} \leftarrow N_{\max}(P_{\min}, \bar{m}) / C_{\bar{m}}^{\text{cum}}$;
    $\epsilon \sim \mathcal{U}(0,1)$;
    if $\epsilon < P_{\text{TX}}$ **then**
      if $\mathcal{T}_{\bar{m}} \neq \emptyset$ **then**
        $t \leftarrow$ Uniform$(\mathcal{T}_{\bar{m}})$;
        $f \leftarrow$ Uniform$(\mathcal{F})$;
        Append (n, m, t, f) to txs;
        $usedLoRa \leftarrow true$;
      end
    end
    $\bar{m} \leftarrow \bar{m} + 1$ `// Try next SF`
  end
  if *not* $usedLoRa$ **then** `// use LR-FHSS`
    $c \leftarrow \beta$-allocation$(\mathcal{C})$;
    $t \leftarrow$ Uniform$(\mathcal{T}_6)$;
    $f_{\text{ocw}} \leftarrow$ Uniform$(\mathcal{OCW})$;
    Append $(n, c, t, f_{\text{ocw}})$ to txs;
  end
end
return txs

ALOHA Load control with Sequential SF

A possible improvement to the *ALOHA Best-SF* is to use the number of competitors informed in the beacon for the uplink period, rather than the total network size. The transmission control probability can then be calculated using the cumulative number of competitors. The *ALOHA Seq-SF* strategy is very similar to the *Success Seq-SF* strategy described in Alg. 7. The key difference is P_{TX}, calculated as follows:

Thèse accessible à l'adresse : https://theses.insa-lyon.fr/publication/2026ISAL0011/these.pdf © [D. Maldonado Muñoz], [2026], INSA Lyon, tous droits réservés

$$P_{\mathrm{TX}}(\bar{m}) = \min\left(1, \bar{N}_{\bar{m}}/C_{\bar{m}}^{\mathrm{cum}}\right). \tag{6.16}$$

6.3.4 Summary of methods

In addition to the Joint Allocation strategies presented in this section, we also extend the optimal allocation models for LoRa allocation only to follow a joint allocation approach. We define the *Opt2D* and *Opt1D* strategies. In a nutshell, after the optimization calculation is performed, the remaining frames that could not be allocated using LoRa modulation will be allocated with LR-FHSS following the same β-allocation as the other strategies presented in this section.

The following Table 6.1 presents a summary of the presented methods in this section.

Table 6.1: Comparison of resource allocation methods.

Allocation method	**Satellite aware**	**Inter-ference aware**	**Modulation selection**	**SF allocation**	**CR allocation**	**Time allocation**
1) Joint-Class A	No	No	50/50	Random SF	β threshold	Random at anytime
2) Joint-Class A Valid-SF	Yes	No	50/50	Random over valid SFs	β threshold	Random at valid time
3) ALOHA Best-SF	Yes	No	LoRa first	Best SF with Load control based on network size	β threshold	Random at valid time
4) ALOHA Seq-SF	Yes	Yes	LoRa first	Sequential SF with Load control based on competitors	β threshold	Random at valid time
5) Success Best-SF	Yes	Yes	LoRa first	Best SF with Success probability threshold	β threshold	Random at valid time
6) Success Seq-SF	Yes	Yes	LoRa first	Sequential with Success probability threshold	β threshold	Random at valid time
7) Opt1D	Yes	Yes	LoRa first	Optimal	β threshold	Optimal

6.4 Results and Analysis

This section evaluates the proposed methods in a realistic DtS-IoT scenario with six LEO satellites and ground-based devices. We first quantify the theoretical limits of LoRa using the centralized optimal allocation upper bound, and then assess the performance of all distributed joint LoRa/LR-FHSS MAC protocols under identical visibility, Doppler, and load conditions. Results are reported for both single-window and complete multi-window passes, enabling a detailed comparison of centralized optimality, distributed feasibility, and pure LR-FHSS operation.

6.4.1 Simulation Scenario and Parameters

The study scenario consists of six satellites from the Starlink constellation. The satellites' ID numbers are 2413, 2396, 3449, 4616, 4629, and 5003 [1]. This allows us to study a theoretical scenario in which

[1]TLE data is obtained from Celestrak.

Thèse accessible à l'adresse : https://theses.insa-lyon.fr/publication/2026ISAL0011/these.pdf © [D. Maldonado Muñoz], [2026], INSA Lyon, tous droits réservés

Table 6.2: Simulation Parameters

Parameter	Description	Value
N_S	Number of satellites	6
H	Satellite altitude	550 km
N	Devices on ground	300
P_t	Transmission power (Device)	14 dBm
G_t	TX gain (Device)	0 dB
G_r	RX gain (Satellite)	3 dB
C_f	Carrier Frequency	868 MHz
d	Packet payload	20 bytes
B_{css}	LoRa Bandwidth	125 kHz
B_{ocw}	LR-FHSS OCW Bandwidth	200 KHz
ψ	LR-FHSS SIR threshold	6 dB
$\alpha_{\min}$	Minimum elevation angle	$18°$
β	CR allocation angle	$32.6°$
D	Maximum concurrent LoRa frames	8
P	TX Power consumption @ 14 dB	92.4 mW

multiple satellites cover the same region. The satellites do not necessarily support IoT, and they were chosen so that their paths cross over the deployment region. The region is defined as Continental France, spanning approximately 1000 km north to south and 900 km west to east at its widest point, making it a reasonably large area for dense IoT deployment. We consider up to N devices deployed over the region.

Satellite ground track calculations are performed using the Skyfield library [99], which implements the SGP4 orbital propagator, with TLE data downloaded periodically to maintain accuracy. All scenarios account for both Doppler Shift and Doppler Rate effects. The Doppler Shift primarily affects communication at the lowest elevation angles, where the link distance is maximum. At the same time, the Doppler Rate causes packet losses at high elevation angles when the satellite is closer to the device. These effects impose constraints on the selection of SFs and limit transmission opportunities during satellite passes. The simulation parameters are summarized in Table 6.2.

The following assumptions are considered:

- Devices are stationary and distributed according to a Poisson point process.
- Each device can only transmit one frame per uplink window.
- The channel model is the FSPL Model presented in Section 5.2.1.
- Perfect SF orthogonality is assumed. A LoRa collision occurs only if two or more signals with the same SF overlap in time and frequency.
- Separate non-interfering channels for LoRa and for LR-FHSS frames.
- A single LoRa channel and another separate single LR-FHSS channel.

The maximum received power obtained at maximum elevation angle is -131 dB while the LR-FHSS sensitivity is -137 dB. Only when a device transmits from the edge of the coverage region at the minimum elevation angle, α_{min}, and another device transmits directly below the satellite will the SIR for the latter be 6 dB, assuming time-frequency collision and no other interfering transmissions. Since this case is improbable, the CR allocation strategy that benefits from the capture effect of LR-FHSS header/fragmentation is ineffective in this scenario.

Thèse accessible à l'adresse : https://theses.insa-lyon.fr/publication/2026ISAL0011/these.pdf © [D. Maldonado Muñoz], [2026], INSA Lyon, tous droits réservés

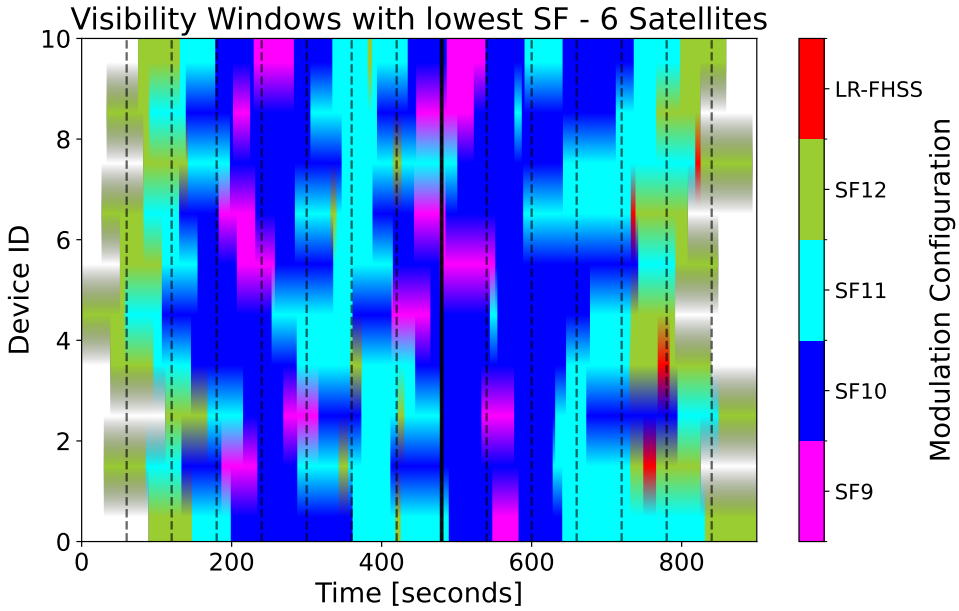


Figure 6.2: Lowest admissible SF vs time across a 15-min pass (6 satellites). Vertical dashed lines mark a 1-minute UL window. Vertical solid line at $t = 480$ marks the 9th UL window.

Fig. 6.2 shows the evolution of the lowest SF that some selected devices can achieve during the lap, with each UL window delimited by vertical black dashed lines. We consider a beacon time of 2.12 seconds, having then 97.88 seconds for uplink transmissions. The total satellite pass lasts 15 minutes, from 2025-10-20 16:15:00 until 16:30:00 of the same day. The lowest SF achieved goes down up to SF9 when the satellites pass directly over the deployment region. The maximum Doppler Shift observed is $\pm$20 kHz, while the maximum Doppler Rate is of 300 Hz/s. Given the bandwidth B_{css} for LoRa and the Doppler limits from Table 2.2.6, only SF12 is expected to fail due to Doppler Rate limitation. This can be observed in cases when SF12 is the only available SF given the link budget but it fails due to Doppler Rate, shown in red. Only LR-FHSS is available at that moment.

6.4.2 Performance of Joint LoRa/LR-FHSS MAC Protocols

This subsection evaluates the distributed joint LoRa/LR-FHSS MAC protocols introduced in Section 6.3 using a single short 15-second uplink window during peak visibility, when most devices support the lowest SF during the satellite pass. We consider the 9th UL window shown in Fig. 6.2. This window represents a challenging but favorable operating point where most devices can transmit at their lowest feasible SF, hence achieving the highest data rate. A strategy using only LoRa frames is excluded due to its well-known scalability limits in DtS settings, while LR-FHSS serves as the reference, here named pure LR-FHSS (no LoRa frames). The analysis contrasts each distributed method against LR-FHSS, and against the centralized *Opt1D* method to quantify both practical performance and remaining headroom. During this window, most devices have the best link and can achieve the lowest SF at some point, either SF9 or SF10.

Figure 6.3 reports the Packet Delivery Ratio (PDR) vs the traffic load measured in packets per second, comparing joint methods with the pure LR-FHSS reference (black dashed).

Joint-Class A performs the worst due to fast LoRa collisions and under-utilized LR-FHSS. *Joint-Class A Valid-SF* strategy performs slightly better with around 5% better PDR.

Thèse accessible à l'adresse : https://theses.insa-lyon.fr/publication/2026ISAL0011/these.pdf © [D. Maldonado Muñoz], [2026], INSA Lyon, tous droits réservés

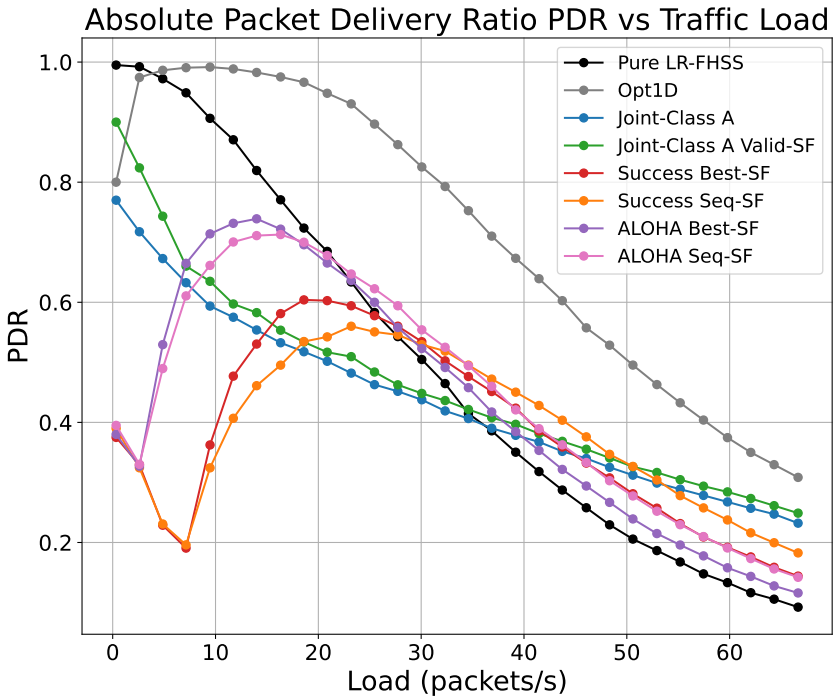


Figure 6.3: Absolute PDR vs. traffic load. Joint LoRa+LR-FHSS vs. pure LR-FHSS.

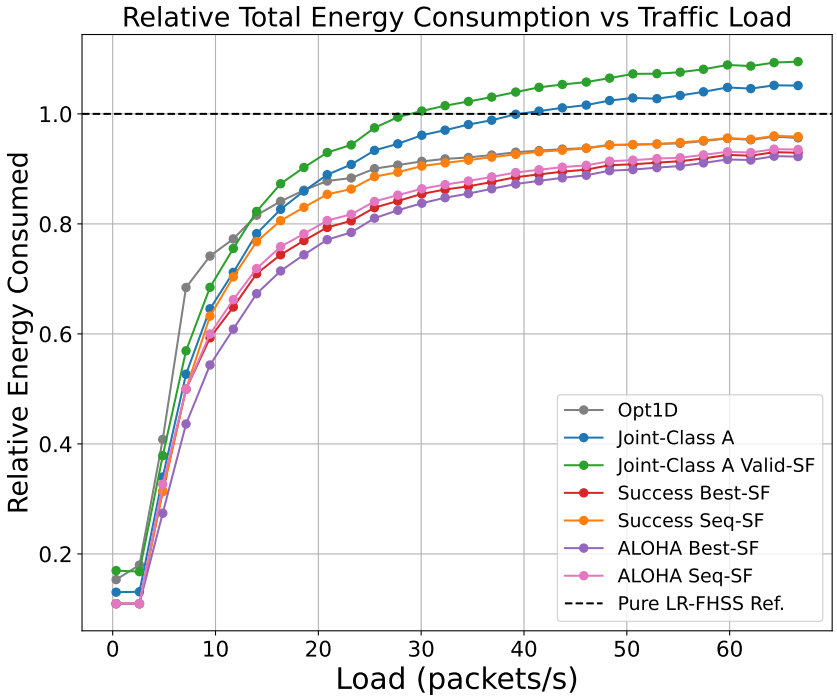


Figure 6.4: Relative energy (to pure LR-FHSS) vs. traffic load. Values < 1 favor joint access.

The *ALOHA Best-SF* and *ALOHA Seq-SF* strategies cross the LR-FHSS baseline at 22 pkt/sec, while the *Success Best-SF* and *Success Seq-SF* strategies do so at around 25 pkt/sec. All these strategies maintain a higher PDR up to the load limit. The *Opt1D* optimal strategy keeps an average

Thèse accessible à l'adresse : https://theses.insa-lyon.fr/publication/2026ISAL0011/these.pdf © [D. Maldonado Muñoz], [2026], INSA Lyon, tous droits réservés

PDR of around 30% advantage by allocating as many collision-free LoRa transmissions as the constraints allow.

Figure 6.4 shows relative consumed energy vs LR-FHSS: joint strategies are more energy efficient than pure LR-FHSS given the longer time-on-air for the latter. However, *Joint-Class A* and *Joint-Class A Valid-SF* strategies consume more energy after 30 and 40 pkt/sec, respectively. *ALOHA Best-SF* is the most energy efficient strategy, while *Success Best-SF* and *ALOHA Seq-SF* follow closely. Both *ALOHA* strategies overcome pure LR-FHSS at around 22 pkt/sec while spending only 80% of the energy it does.

It is important to note that these results represent the most beneficial scenario for the joint strategies, as most devices achieve their best link and thus lowest SF (i.e., SF9 and SF10) during the considered uplink window. For other uplink windows with worse link conditions that support only higher SFs, such as SF11 and SF12, the joint strategies will perform worse than the pure LR-FHSS strategy. However, joint strategies will also benefit when having more available LoRa channels.

We also obtained metrics on the complexity of *Opt1D* and *Opt2D* measured in execution time. We observe that *Opt2D* is almost 2 orders of magnitude more complex in terms of computation time than *Opt1D* while achieving similiar performance in PDR and throughput. We decide to focus the subsequent analysis on comparing with the *Opt1D* strategy.

6.4.3 Tuning the Success-Probability Threshold

Success Best-SF and *Success Seq-SF* strategies rely on a tunable probability threshold, $P_{\min}$, that controls how aggressively devices access the LoRa channel. This subsection studies the impact of $P_{\min}$ over a complete multi-window satellite pass, revealing the trade-off between increased reliability (higher PDR) and reduced unique throughput. By examining cumulative receptions and running PDR across several minutes of visibility, we identify suitable operating points and justify the choice of $P_{\min} = 0.6$ for subsequent comparisons.

We consider a complete 15-minute pass with UL windows of 1 minute, 300 packets per window, each with a 20-byte payload. Figures 6.5–6.6 quantify the effect of the success-based probability threshold $P_{\min}$ for the *Success Seq-SF* strategy compared with the optimal *Opt1D* strategy.

First, we notice that the total receptions for the *Opt1D* exceed the transmitted packets, which is explained by the coverage of multiple satellites.

Higher $P_{\min}$ reduces collisions by reducing the transmission probability, and thus it improves the cumulative PDR (Fig. 6.6). This comes with the cost of fewer unique receptions (Fig. 6.5), exposing a clear throughput–reliability trade-off. For subsequent comparisons, we fix $P_{\min} = 0.6$ as a balanced choice.

6.4.4 Time-Evolving Performance Across Multiple UL Windows

While single-window results capture peak visibility behavior, DtS-IoT performance varies significantly throughout a complete satellite pass. This subsection provides a per-window breakdown of throughput and PDR across the whole sequence of UL windows, highlighting how elevation-dependent feasibility, load distribution, and MAC decisions interact over time. A beacon signal starts each UL window. The comparison across all distributed schemes and the centralized *Opt1D* method clarifies which

Thèse accessible à l'adresse : https://theses.insa-lyon.fr/publication/2026ISAL0011/these.pdf © [D. Maldonado Muñoz], [2026], INSA Lyon, tous droits réservés

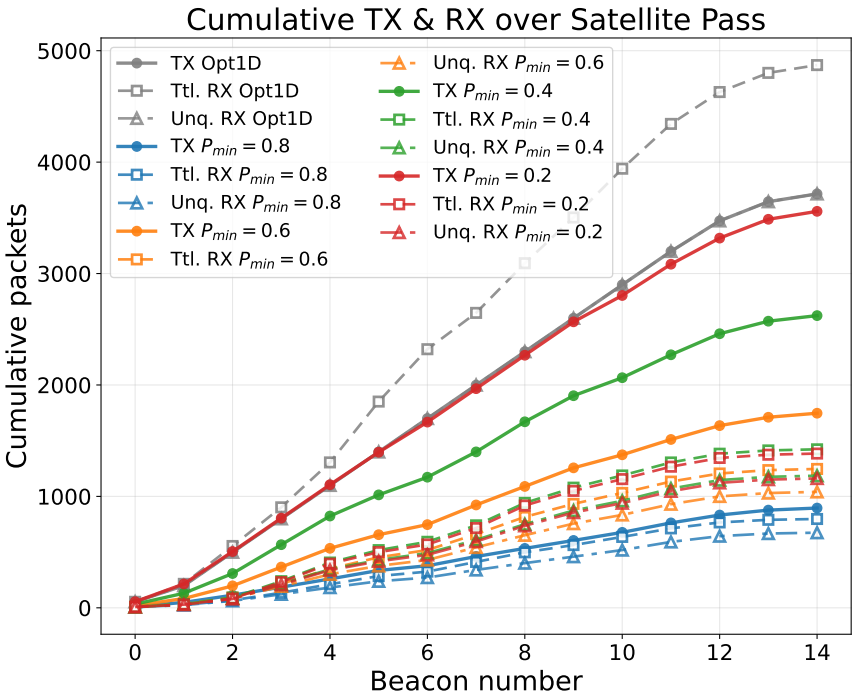


Figure 6.5: Cumulative TX/RX across the pass. *Success Seq-SF* with $P_{\min} \in \{0.2, 0.4, 0.6, 0.8\}$ and *Opt1D*. Solid-circle: unique RX; Dashed-square: total RX; Dash-dot-triangle: unique RX

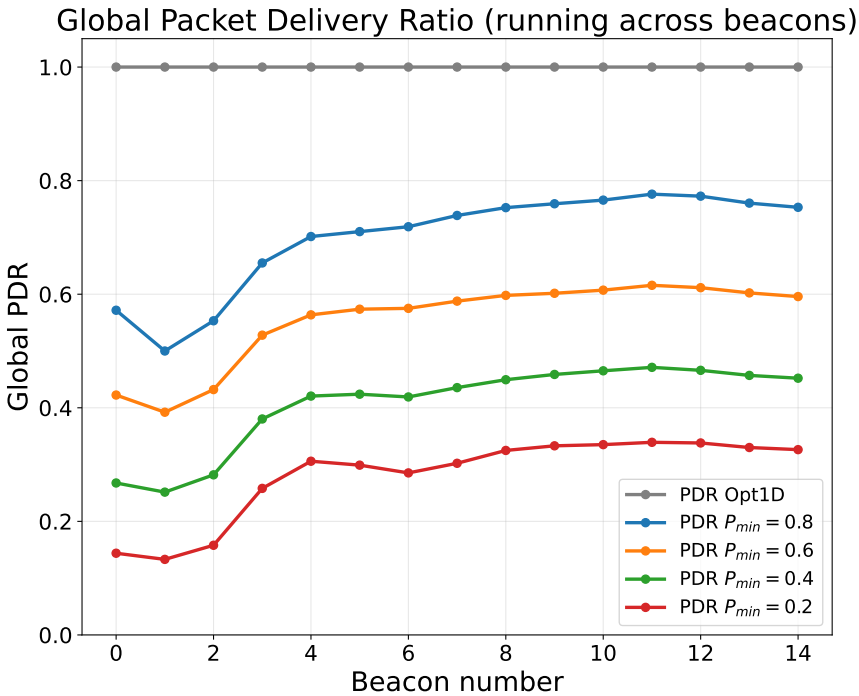


Figure 6.6: Running global normalized PDR across windows. *Success Seq-SF* with varying $P_{\min} \in \{0.2, 0.4, 0.6, 0.8\}$ and *Opt1D*.

Thèse accessible à l'adresse : https://theses.insa-lyon.fr/publication/2026ISAL0011/these.pdf © [D. Maldonado Muñoz], [2026], INSA Lyon, tous droits réservés

strategies capture mid-pass opportunities and which maintain reliable operation near the visibility edges.

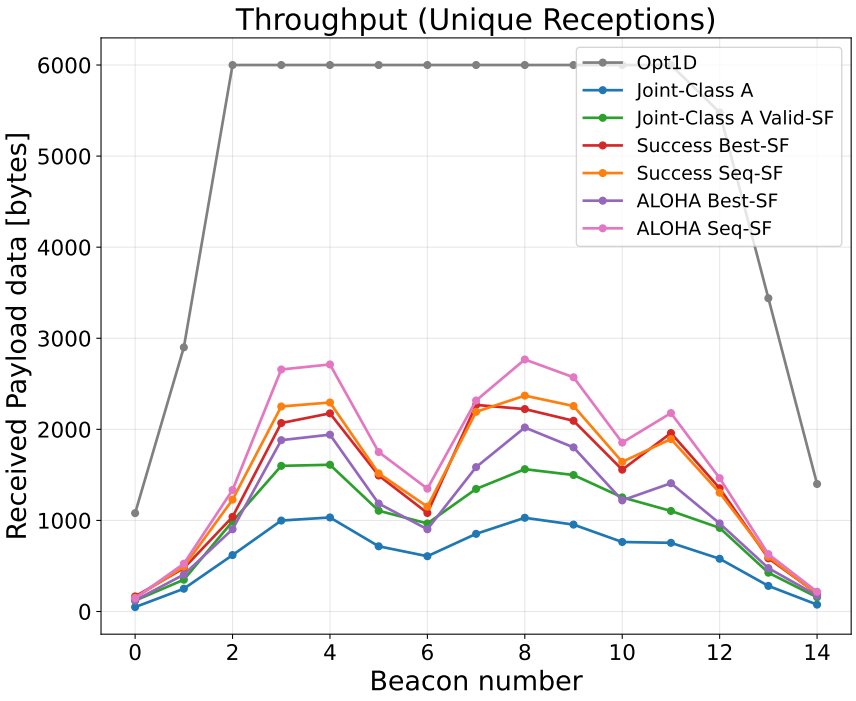


Figure 6.7: Per-window throughput (unique payload bytes). Joint methods vs *Opt1D*.

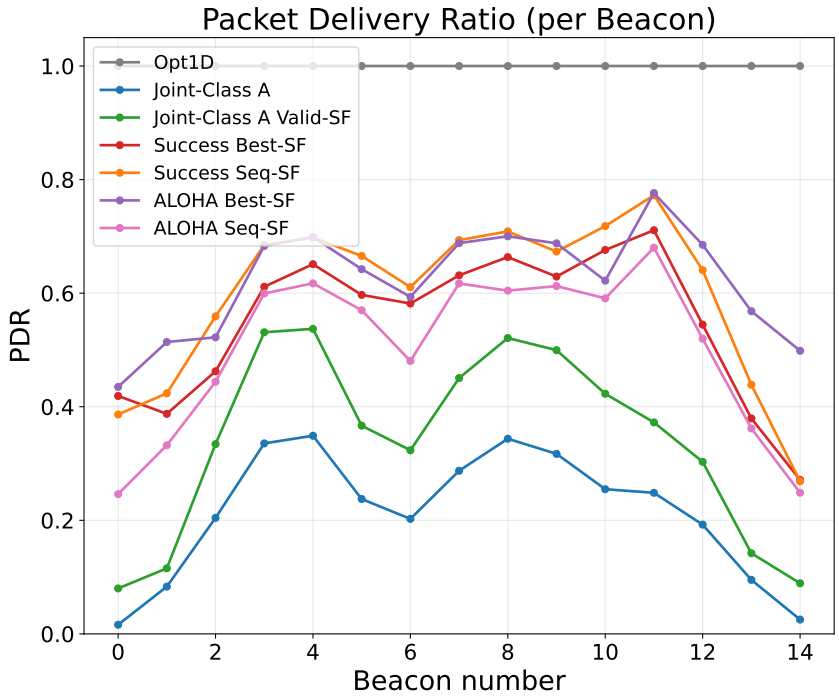


Figure 6.8: Per-window PDR (over sent packets). Joint methods vs *Opt1D*.

Figures 6.7–6.8 break down per-beacon (time-evolving) behavior. The *ALOHA Seq-SF* strategy

Thèse accessible à l'adresse : https://theses.insa-lyon.fr/publication/2026ISAL0011/these.pdf © [D. Maldonado Muñoz], [2026], INSA Lyon, tous droits réservés

yields the largest unique receptions overall (Fig. 6.7), while the *Success Seq-SF* strategy attains the best per-window PDR envelope (Fig. 6.8). We observe again the trade-off between throughput and reliability, as *ALOHA Best-SF* strategy is also the least performing Joint strategy in terms of PDR, excluding the *Joint-Class A* and *Joint-Class A Valid-SF* strategies. However, in this case, the *Success Seq-SF* also achieves high throughput, second only to the *ALOHA Seq-SF* strategy. We also observe how superior the *Joint-Class A Valid-SF* is compared with the *Joint-Class A*, even if both use a random 50/50 split between LoRa allocation and LR-FHSS allocation. This highlights the importance of making orbit-estimation-informed allocation decisions.

As expected, the *Opt1D* strategy traces the idealized upper bound; it assumes perfect global knowledge and coordination and is not meant for direct deployment but to quantify the headroom of practical schemes. It can successfully allocate and receive all generated packets, a total of 6000 bytes, for the best visibility UL windows, as Fig. 6.7 shows. On the edges of the constellation pass, during beacons 0, 1, 13, and 14, there is limited coverage with low throughput.

6.5 Conclusion

In this chapter, we investigated joint LoRa and LR-FHSS resource allocation strategies for DtS-IoT uplinks. We first formulated a centralized optimal allocation, which assumes perfect global knowledge and provides strict upper bounds on achievable throughput. We then designed a family of distributed joint LoRa/LR-FHSS MAC protocols that rely only on local visibility supported by periodic beacons.

Our results in a 6-satellite DtS scenario show that joint access becomes beneficial once the load exceeds 22 pkt/sec, while only spending 80% of the energy compared to a pure LR-FHSS strategy. Success-probability-based and ALOHA load-control strategies, with their Best-SF and Seq-SF variants, demonstrate a clear improvement over the extended Class A baselines, *Joint-Class A* and *Joint-Class A Valid-SF*. We highlight the benefits of orbit, and network size and number of competitors per SF-informed decisions for joint allocation strategies.

Future work includes extending the models to multi-gateway or multi-beam satellites, incorporating more detailed channel and interference models, and validating the proposed MAC schemes in hardware testbeds. Another direction is to couple joint LoRa/LR-FHSS access with adaptive coding and traffic shaping, and to study cross-layer integration with higher-layer scheduling and routing.

Thèse accessible à l'adresse : https://theses.insa-lyon.fr/publication/2026ISAL0011/these.pdf © [D. Maldonado Muñoz], [2026], INSA Lyon, tous droits réservés

Thèse accessible à l'adresse : https://theses.insa-lyon.fr/publication/2026ISAL0011/these.pdf © [D. Maldonado Muñoz], [2026], INSA Lyon, tous droits réservés

Chapter 7

Conclusions

7.1 Summary of main contributions

This thesis addressed the scalability and reliability challenges of Direct-to-Satellite IoT (DtS-IoT) by proposing new mechanisms at the MAC, link and physical layers for LoRa and LR-FHSS over LEO satellites and constellations. Across the chapters, the work moved from single-satellite network-size estimation, through constellation-aware extensions and advanced LR-FHSS receivers, up to joint LoRa/LR-FHSS resource allocation, providing state-of-the-art methods for massive DtS-IoT deployments.

Chapter 3 introduced L-OCI, the first LoRa/LoRaWAN-compatible realization of the Optimistic Collision Information (OCI) estimator, and showed via FLoRaSat simulations that accurate network size estimates can be obtained with low energy cost for up to roughly 500 nodes using carefully selected LoRa parameters. The study further showed that L-OCI is robust to parameter variations and that feeding its estimates into Slotted Aloha Game (SAG) enables near-optimal throughput while smoothing the impact of estimation errors, thus turning network-size information into a practical MAC design primitive for DtS-IoT. These results constitute the first end-to-end evaluation of OCI embedded in a realistic LoRa-based DtS-IoT stack thanks to the FLoRaSat simulator.

Building on this, L-OCI was further adapted to realistic LEO constellations through CL-OCI, explicitly accounting for ground-track shifts and partial footprint overlaps between satellites. By grouping nodes and aggregating per-satellite estimates with overlap-aware weighting, CL-OCI doubles the estimable network size beyond the single-satellite limit and yields up to a seven-fold reduction in energy wasted in collided transmissions compared to the original L-OCI, while maintaining estimation errors compatible with MAC protocols such as SA-GAME. This chapter shows that network-size estimation can remain lightweight yet effective even in discontinuous, multi-satellite DtS-IoT constellations.

At the LR-FHSS physical layer, Chapter 4 analysed the Frequency Hopping Sequence (FHS)-generation mechanisms implemented in LR-FHSS devices, revealed their m-sequence roots, and proposed novel FHS families based on Wide-Gap constructions together with demodulator allocation strategies (Early-Decode and Early-Drop). Simulations showed that suitable Li–Fan-based Wide-Gap FHS reduce collision rates compared to the driver FHS, and that the proposed demodulator strategies can increase the number of successfully decoded LR-FHSS frames by up to about 50% in certain loads, especially when demodulator resources are scarce. This provides the first joint treatment of LR-FHSS sequence design and demodulator allocation for scalability in DtS-IoT networks.

Thèse accessible à l'adresse : https://theses.insa-lyon.fr/publication/2026ISAL0011/these.pdf © [D. Maldonado Muñoz], [2026], INSA Lyon, tous droits réservés

Chapter 5 then addressed one of the main bottlenecks of LR-FHSS scalability, namely header fragility, by introducing an enhanced LR-FHSS receiver capable of recovering headerless frames under realistic Doppler conditions. The work models a DtS-IoT channel with realistic Doppler effect. It adapts a greedy headerless-decoding heuristic to account for time–frequency shifts, and embeds it in a receiver architecture that combines conventional header-based decoding with exhaustive recovery of payloads whose headers are lost. Results show that the enhanced receiver can increase the number of decoded frames by up to roughly 50% in both satellite and terrestrial LR-FHSS scenarios at medium loads, with particularly strong gains in DtS-IoT where Doppler diversity helps distinguish hopping patterns.

Finally, Chapter 6 investigated joint LoRa/LR-FHSS resource allocation in DtS-IoT, formulating centralized optimal LoRa schedulers as 1D and 2D strip-packing problems and designing practical distributed MAC schemes that combine visibility-aware feasibility, beacon-based interference indicators and modulation selection between LoRa and LR-FHSS. In a realistic six-satellite LEO scenario, the proposed joint schemes surpass pure LR-FHSS once the load exceeds approximately 22 packets per second, achieving up to roughly 10–15 percentage-point throughput gains near the 50% delivery point while consuming only about 80% of the energy of a LR-FHSS-only strategy at high load. The analysis also quantifies the gap to the centralized upper bound and shows that lightweight, beacon-fed policies can operate close to near-optimal sequential allocation while remaining implementable on constrained devices.

7.2 Global discussion

Taken together, the chapters demonstrate a coherent progression from MAC-layer awareness (through L-OCI and CL-OCI) to LR-FHSS physical-layer enhancements and, finally, to cross-layer joint access schemes that orchestrate LoRa and LR-FHSS in DtS-IoT networks. Network-size estimation provides the satellite or network server with congestion indicators, advanced LR-FHSS receivers and sequences improve the robustness and decoding capacity under that congestion, and the joint LoRa/LR-FHSS MAC exploits both to select transmission modes and parameters in a visibility- and interference-aware way.

This integration advances the state of the art in DtS-IoT beyond isolated feasibility studies by showing how realistic orbital dynamics, Doppler effects, demodulator limits and beacon-based control can all be jointly exploited to improve scalability without abandoning low-cost, LoRa-compatible technology. In particular, the thesis supplies (i) the first LoRa-compatible OCI implementation and its constellation extension, (ii) the first detailed analysis and redesign of LR-FHSS hopping sequences and demodulator policies under massive access, (iii) a practical headerless LR-FHSS decoding architecture for space–terrestrial networks, and (iv) the first comparative evaluation of joint LoRa/LR-FHSS access against optimal baselines in realistic multi-satellite DtS-IoT scenarios.

7.3 Future work

Several lines of research emerge naturally from the contributions of this thesis. For network-size estimation, L-OCI and CL-OCI can be extended by training over richer parameter spaces (e.g., additional spreading-factor and bandwidth combinations, different beacon periods), and by incorporating multi-plane constellations and inter-satellite links, as already envisaged for future CL-OCI developments. A promising direction is to couple CL-OCI estimates with constellation-level MAC

Thèse accessible à l'adresse : https://theses.insa-lyon.fr/publication/2026ISAL0011/these.pdf © [D. Maldonado Muñoz], [2026], INSA Lyon, tous droits réservés

and routing schemes that exploit per-plane load information, rather than using the estimates only to drive single-link access control.

On the LR-FHSS side, the Wide-Gap-based FHS families and Early-Decode/Early-Drop strategies could be re-evaluated under more detailed physical-layer models including fading, atmospheric losses and explicit capture effect, complementing the free-space abstractions used so far. It would also be valuable to integrate headerless decoding strategies into a unified receiver that jointly optimizes when to abandon hopeless frames, when to attempt headerless recovery, and how to allocate demodulators across LR-FHSS and LoRa.

The enhanced LR-FHSS receiver opens additional perspectives around complexity reduction, smarter search in the time–frequency plane, and collaborative decoding across multiple satellites or gateways that observe different Doppler signatures of the same frames. Validating the approach using hardware testbeds or in-orbit experiments would be a crucial step, as would combining realistic capture-aware decoding with the pessimistic collision models used to date to bound the achievable gains.

For joint LoRa/LR-FHSS resource allocation, the optimal models could be extended to multi-beam satellites, multi-gateway or feeder-link scenarios, and to additional channels and regional configurations, following the future directions suggested in the original study. On the distributed side, there is room to explore tighter cross-layer integration with traffic shaping, adaptive coding and higher-layer scheduling, as well as to study operation under heterogeneous application QoS targets, potentially building on success-probability-based thresholds and load-control ideas already outlined in the joint-access work.

Finally, a broader research direction is to connect the estimation, PHY and MAC mechanisms developed here into a fully integrated DtS-IoT architecture, where CL-OCI-style estimators inform not only MAC but also routing, satellite activation patterns and orbit design, and where LR-FHSS sequence/receiver choices and LoRa/LR-FHSS mode selection are jointly optimized under mission-level energy and cost constraints. Such an end-to-end perspective would help translate the building blocks provided by this thesis into deployable designs for sustainable, efficient and scalable DtS-IoT networks.

Thèse accessible à l'adresse : https://theses.insa-lyon.fr/publication/2026ISAL0011/these.pdf © [D. Maldonado Muñoz], [2026], INSA Lyon, tous droits réservés

Thèse accessible à l'adresse : https://theses.insa-lyon.fr/publication/2026ISAL0011/these.pdf © [D. Maldonado Muñoz], [2026], INSA Lyon, tous droits réservés

Publications by the Author

[1] P. Ilabaca, D. Maldonado, J. A. Fraire, S. Montejo-Sánchez, and S. Céspedes, "Network size estimation in dts-iot: A lorawan approach for satellite constellations," in ICC 2025-IEEE International Conference on Communications. IEEE, 2025, pp. 5506–5511.

[2] D. Maldonado, M. Kaneko, J. A. Fraire, A. Guitton, O. Iova, and H. Rivano, "Enhancing lr-fhss scalability through advanced sequence design and demodulator allocation," IEEE Transactions on Green Communications and Networking, 2025.

[3] D. Maldonado, L. S. Cardoso, J. A. Fraire, A. Guitton, O. Iova, M. Kaneko, and H. Rivano, "Enhanced lr-fhss receiver for headerless frame recovery in space–terrestrial integrated iot networks," Computer Networks, vol. 257, p. 111018, 2025.

[4] S. I. Montoya, D. Maldonado, J. A. Fraire, and S. Céspedes, "On the role of delay tolerant networks and contact graph routing in direct-to-satellite iot," in 2024 IEEE 10th International Conference on Space Mission Challenges for Information Technology (SMC-IT). IEEE, 2024, pp. 151–160.

[5] D. Maldonado, J. A. Fraire, P. Ilabaca, H. Rivano, and S. Céspedes, "Network size estimation for lora-based direct-to-satellite iot," in 2023 IEEE Cognitive Communications for Aerospace Applications Workshop (CCAAW). IEEE, 2023, pp. 1–6.

Thèse accessible à l'adresse : https://theses.insa-lyon.fr/publication/2026ISAL0011/these.pdf © [D. Maldonado Muñoz], [2026], INSA Lyon, tous droits réservés

Thèse accessible à l'adresse : https://theses.insa-lyon.fr/publication/2026ISAL0011/these.pdf © [D. Maldonado Muñoz], [2026], INSA Lyon, tous droits réservés

References

[6] J. A. Fraire, O. Iova, and F. Valois, “Space-terrestrial integrated internet of things: Challenges and opportunities,” IEEE Communications Magazine, vol. 60, no. 12, pp. 64–70, 2022.

[7] M. De Sanctis, E. Cianca, G. Araniti, I. Bisio, and R. Prasad, “Satellite communications supporting Internet of remote Things,” IEEE Internet of Things J., vol. 3, no. 1, pp. 113–123, 2015.

[8] IoT Analytics, “Satellite IoT market report 2025–2030,” IoT Analytics GmbH, Market Report, Jun. 2025. [Online]. Available: https://iot-analytics.com/product/satellite-iot-market-report-2025-2030/

[9] J. A. Fraire, S. Céspedes, and N. Accettura, “Direct-to-satellite IoT-a survey of the state of the art and future research perspectives: Backhauling the IoT through LEO satellites,” in ADHOC-NOW 2019, Proceedings 18. Springer, 2019, pp. 241–258.

[10] J. A. Fraire, S. Henn, F. Dovis, R. Garello, and G. Taricco, “Sparse Satellite Constellation Design for LoRa-based Direct-to-Satellite Internet of Things,” in GLOBECOM 2020-2020 IEEE Global Communications Conference. IEEE, 2020, pp. 1–6.

[11] J. Zhang, Y. Cai, C. Xue, Z. Xue, and H. Cai, “Leo mega constellations: review of development, impact, surveillance, and governance,” Space: Science & Technology, 2022.

[12] F. Gu, J. Niu, L. Jiang, X. Liu, and M. Atiquzzaman, “Survey of the low power wide area network technologies,” Journal of Network and Computer Applications, vol. 149, p. 102459, 2020.

[13] C. Vincent, B. J. Mcconnell, V. Ridoux, and M. A. Fedak, “Assessment of Argos Location Accuracy from Satellite Tags Deployed on Captive Gray Seals,” Marine Mammal Science, vol. 18, no. 1, pp. 156–166, 2002.

[14] R. Patmasari, I. Wijayanto, R. Deanto, Y. Gautama, and H. Vidyaningtyas, “Design and Realization of Automatic Packet Reporting System (APRS) for Sending Telemetry Data in Nano Satellite Communication System,” Journal of Measurements, Electronics, Communications, and Systems, vol. 4, no. 1, pp. 1–7, 2018.

[15] J. Carson-Jackson, “Satellite AIS – Developing Technology or Existing Capability?” Journal of Navigation, vol. 65, no. 2, p. 303–321, 2012.

[16] K. Werner, J. Bredemeyer, and T. Delovski, “ADS-B Over Satellite: Global Air Traffic Surveillance from Space,” in 2014 Tyrrhenian International Workshop on Digital Communications-Enhanced Surveillance of Aircraft and Vehicles (TIWDC/ESAV). IEEE, 2014, pp. 47–52.

[17] LoRa Alliance Technical Committee, “TS001-1.0.4 LoRaWAN L2 1.0.4 Specification,” LoRa Alliance, Technical Specification, Oct. 2020, version 1.0.4. [Online]. Available: https://resources.lora-alliance.org/technical-specifications/ts001-1-0-4-lorawan-l2-1-0-4-specification

Thèse accessible à l'adresse : https://theses.insa-lyon.fr/publication/2026ISAL0011/these.pdf © [D. Maldonado Muñoz], [2026], INSA Lyon, tous droits réservés

[18] “Cubesat design specification,” https://static1.squarespace.com/static/5418c831e4b0fa4ecac1bacd/t/5f24997b6deea10cc52bb016/1596234122437/CDS+REV14+2020-07-31+DRAFT.pdf, accessed: 2023-04-13.

[19] C. Gonzalez, C. Rojas, A. Becerra, J. Rojas, T. Opazo, and M. Diaz, “Lessons learned from building the first chilean nano-satellite: The suchai project,” 2018.

[20] N. Saeed, A. Elzanaty, H. Almorad, H. Dahrouj, T. Y. Al-Naffouri, and M.-S. Alouini, “Cubesat communications: Recent advances and future challenges,” IEEE Communications Surveys & Tutorials, vol. 22, no. 3, pp. 1839–1862, 2020.

[21] M. Chen, Y. Miao, Y. Hao, and K. Hwang, “Narrow band internet of things,” IEEE access, vol. 5, pp. 20 557–20 577, 2017.

[22] C. B. Mwakwata, H. Malik, M. Mahtab Alam, Y. Le Moullec, S. Parand, and S. Mumtaz, “Narrowband internet of things (nb-iot): From physical (phy) and media access control (mac) layers perspectives,” Sensors, vol. 19, no. 11, p. 2613, 2019.

[23] S. Cluzel, L. Franck, J. Radzik, S. Cazalens, M. Dervin, C. Baudoin, and D. Dragomirescu, “3gpp nb-iot coverage extension using leo satellites,” in 2018 IEEE 87th Vehicular Technology Conference (VTC Spring). IEEE, 2018, pp. 1–5.

[24] H. Chougrani, S. Kisseleff, W. A. Martins, and S. Chatzinotas, “Nb-iot random access for nonterrestrial networks: Preamble detection and uplink synchronization,” IEEE Internet of Things Journal, vol. 9, no. 16, pp. 14 913–14 927, 2021.

[25] European Telecommunications Standards Institute (ETSI), “Short range devices; low throughput networks (ltn); protocols for radio interface a; part 2: Ts-unb protocol,” ETSI, Technical Specification TS 103 357-2 V2.1.1, 2024. [Online]. Available: https://www.etsi.org/deliver/etsi_ts/103300_103399/10335702/02.01.01_60/ts_10335702v020101p.pdf

[26] J. Mrazek, S. Kisseleff, C. Rohde, J. Robert, J. Kneissl, and F. Leschka, “mioty superiority over both lora-versions in satellite-iot applications,” in IET Conference Proceedings CP903, vol. 2024, no. 31. IET, 2024, pp. 63–70.

[27] mioty alliance, “Join our alliance for innovative solutions,” https://mioty-alliance.com/alliance/, 2025, accessed: 2025-12-10.

[28] Semtech Corporation, “Lorawan protocol expands network capacity with new long range – frequency hopping spread spectrum technology,” https://blog.semtech.com/lorawan-protocol-expands-network-capacity-with-new-long-range-frequency-hopping-spread-spectrum-technology, 2021, accessed: 2025-12-10.

[29] ——, “AN1200.22: Lora modulation basics,” Semtech Corporation, Camarillo, CA, USA, Application Note AN1200.22, May 2015, revision 2. [Online]. Available: https://www.semtech.com/products/wireless-rf/lora-connect/sx1272

[30] LoRa Alliance Technical Committee, “RP002-1.0.5 LoRaWAN Regional Parameters,” LoRa Alliance, Technical Specification, Oct. 2025, version 1.0.5. [Online]. Available: https://resources.lora-alliance.org/technical-specifications/rp002-1-0-5-lorawan-regional-parameters

[31] Semtech, “An1200.64—lr-fhss system performance,” Online, accessed: Nov. 17, 2025. Also available via the LR1120 product page.

[32] G. Boquet, P. Tuset-Peiró, F. Adelantado, T. Watteyne, and X. Vilajosana, “LR-FHSS: Overview and performance analysis,” IEEE Communications Magazine, vol. 59, no. 3, pp. 30–36, 2021.

Thèse accessible à l'adresse : https://theses.insa-lyon.fr/publication/2026ISAL0011/these.pdf © [D. Maldonado Muñoz], [2026], INSA Lyon, tous droits réservés

[33] T. Turletti, “GMSK in a nutshell,” Telemedia Networks and Systems Group LCS, MIT-TR, 1996.

[34] Semtech, “Application Note: LR-FHSS System Performance,” Available at https://www.mouser.com/pdfDocs/AN1200-64_LR-FHSS_system_performance_V1_2.pdf (2023/04/17), pp. 1–28, February 2022.

[35] J. A. Fraire, A. Guitton, and O. Iova, “Recovering headerless frames in LR-FHSS,” arXiv preprint arXiv:2306.08360, 2023.

[36] LoRa Alliance, “About lora alliance®,” https://lora-alliance.org/about-lora-alliance/, 2025, accessed: 2025-12-10.

[37] N. Abramson, “The aloha system: Another alternative for computer communications,” in Proceedings of the November 17-19, 1970, fall joint computer conference, 1970, pp. 281–285.

[38] Semtech. An1200.80—lora® modem doppler immunity appnote. Online. [Online]. Available: https://www.semtech.com/products/wireless-rf/lora-edge/lr1120

[39] ——, “Lr1120—lora edge™ transceiver,” Online, accessed: Nov. 17, 2025. [Online]. Available: https://www.semtech.com/products/wireless-rf/lora-edge/lr1120

[40] P. Ilabaca Parra, S. Montejo-Sánchez, J. A. Fraire, R. D. Souza, and S. Céspedes, “Network size estimation for direct-to-satellite iot,” IEEE Internet of Things Journal, vol. 10, no. 7, pp. 6111–6125, 2022.

[41] A. Varga and R. Hornig, “An overview of the omnet++ simulation environment,” in 1st International ICST Conference on Simulation Tools and Techniques for Communications, Networks and Systems, 2010.

[42] J. A. Fraire, P. Madoery, M. A. Mesbah, O. Iova, and F. Valois, “Simulating lora-based direct-to-satellite iot networks with florasat,” in 2022 IEEE 23rd WoWMoM. IEEE, 2022, pp. 464–470.

[43] “Inet framework.” [Online]. Available: https://inet.omnetpp.org/

[44] M. Slabicki, G. Premsankar, and M. Di Francesco, “Adaptive configuration of lora networks for dense iot deployments,” in NOMS 2018-2018 IEEE/IFIP Network Operations and Management Symposium. IEEE, 2018, pp. 1–9.

[45] A. Valentine and G. Parisis, “Developing and experimenting with leo satellite constellations in omnet++,” arXiv:2109.12046, 2021.

[46] B. Niehoefer, S. Šubik, and C. Wietfeld, “The cni open source satellite simulator based on omnet++,” in Proc. of the 6th International ICST Conference on Simulation Tools and Techniques, 2013, pp. 314–321.

[47] A. Y. Choquenaira-Florez, R. Ohs, J. A. Fraire, and H. Rivano, “Florasat 2: Simulating cross-linked direct-to-satellite iot leo constellations,” in 2025 12th Advanced Satellite Multimedia Systems Conference and the 18th Signal Processing for Space Communications Workshop (ASMS/SPSC). IEEE, 2025, pp. 1–8.

[48] A. Y. Choquenaira-Florez, B. Coeugnet, R. Ohs, J. A. Fraire, H. Rivano, and I. A. L. la Doua, “Florasat 2: Simulating cross-linked direct-to-satellite iot leo constellations with joint access and routing evaluation,” 2025.

[49] J. Gerard, J. A. Fraire, R. Ortigueira, and S. Céspedes, “Dts-iot resource allocation analysis framework: Assessing dq and ress-iot,” in 2024 IEEE 10th World Forum on Internet of Things (WF-IoT). IEEE, 2024, pp. 672–677.

Thèse accessible à l'adresse : https://theses.insa-lyon.fr/publication/2026ISAL0011/these.pdf © [D. Maldonado Muñoz], [2026], INSA Lyon, tous droits réservés

[50] J. Gerard, J. A. Fraire, and S. Céspedes, “Unlocking dts-iot medium access through the massively scalable distributed queuing protocol,” in 2024 IEEE 10th World Forum on Internet of Things (WF-IoT). IEEE, 2024, pp. 840–845.

[51] M. A. Mojamed, “Beacon based uplink transmission for lorawan direct to satellite internet of things,” arXiv preprint arXiv:2409.20408, 2024.

[52] L. Tang, W. Zhang, Y. Tang, B. Xia, and Q. Chen, “Joint backoff algorithm based on information freshness and ne equilibrium in low earth orbit satellite iot scenarios,” IEEE Internet of Things Journal, 2025.

[53] V. Hartig, M. Bosk, N. Mohan, and P. Mendes, “Segment routing based on geographic checkpoints,” in Proceedings of the 2nd International Workshop on LEO Networking and Communication, 2024, pp. 25–30.

[54] G. L. Scapin, G. Alvarez, N. Quiroga, F. Collado, and J. A. Fraire, “Performance assessment of lorawan dts-iot networks: Operation modes and server placement,” in 2024 IEEE Biennial Congress of Argentina (ARGENCON). IEEE, 2024, pp. 1–8.

[55] J. Gerard and S. Céspedes, “Sailing the cosmic seas: Improving dependability in iot-based deep space exploration,” in 2024 6th International Conference on Communications, Signal Processing, and their Applications (ICCSPA). IEEE, 2024, pp. 1–3.

[56] W. Jiang, Y. Zhan, X. Xiao, and G. Sha, “Network simulators for satellite-terrestrial integrated networks: A survey,” IEEE Access, vol. 11, pp. 98 269–98 292, 2023.

[57] L. Chasserat, N. Accettura, and P. Berthou, “Lorasync: energy efficient synchronization for scalable lorawan,” Transactions on emerging telecommunications technologies, vol. 35, no. 2, p. e4940, 2024.

[58] ——, “Short: Achieving energy efficiency in dense lorawans through tdma,” in 2020 IEEE 21st International Symposium on" A World of Wireless, Mobile and Multimedia Networks"(WoWMoM). IEEE, 2020, pp. 26–29.

[59] C. Han, Y. Zhang, S. Bai, X. Sun, and X. Wang, “Novel method to calculate satellite visibility for an arbitrary sensor field,” Aerospace Science and Technology, vol. 112, p. 106668, 2021.

[60] Q. Zhang and H. Li, “Moea/d: A multiobjective evolutionary algorithm based on decomposition,” IEEE Transactions on evolutionary computation, vol. 11, no. 6, pp. 712–731, 2007.

[61] B. Zhao, G. Ren, and H. Zhang, “Slotted aloha game for medium access control in satellite networks,” in 2019 IEEE/CIC Int. Conference on Communications in China (ICCC). IEEE, 2019, pp. 518–522.

[62] SEMTECH, “Semtech sx1272/73 lora transceiver documentation,” 2019. [Online]. Available: https://www.semtech.com/products/wireless-rf/lora-connect/sx1272#documentation

[63] H. Chelle, M. Crosnier, V. Deslandes, R. Dhaouz, and A.-L. Beylot, “Modelling discontinuous leo satellite constellations: Impact on the machine-to-machine traffic and performance evaluation,” in 2016 8th Advanced Satellite Multimedia Systems Conference and the 14th Signal Processing for Space Communications Workshop (ASMS/SPSC). IEEE, 2016, pp. 1–7.

[64] S. Alnaqbi, D. Darfilal, and S. S. M. Swei, “Propulsion technologies for cubesats,” Aerospace, vol. 11, no. 7, p. 502, 2024.

[65] W.-C. Lu, L. Duan, and Y.-X. Cai, “De-tumbling control of a cubesat,” in 2018 IEEE International Conference on Advanced Manufacturing (ICAM). IEEE, 2018, pp. 298–301.

Thèse accessible à l'adresse : https://theses.insa-lyon.fr/publication/2026ISAL0011/these.pdf © [D. Maldonado Muñoz], [2026], INSA Lyon, tous droits réservés

[66] S. Herrería-Alonso, M. Rodríguez-Pérez, R. F. Rodríguez-Rubio, and F. Pérez-Fontán, "Improving uplink scalability of lora-based direct-to-satellite iot networks," IEEE Internet of Things Journal, vol. 11, no. 7, pp. 12 526–12 535, 2023.

[67] FOSSA. (2024) *Satellite IoT | FOSSA Systems*. [Accessed: 23 September 2024]. [Online]. Available: https://fossa.systems/iot-connectivity/

[68] F. A. Tondo, J. M. de Souza Sant'Ana, S. Montejo-Sánchez, O. L. A. López, S. Céspedes, and R. D. Souza, "Non-orthogonal multiple-access strategies for direct-to-satellite iot networks," IEEE Transactions on Aerospace and Electronic Systems, 2025.

[69] T. Deng, J. Zhu, and Z. Nie, "An adaptive mac protocol for sdcs system based on lora technology," in 2017 2nd International Conference on Automation, Mechanical Control and Computational Engineering (AMCCE 2017). Atlantis Press, 2017, pp. 825–830.

[70] A. Addaim, A. Kherras, and Z. Guennoun, "Enhanced mac protocol for designing a wireless sensor network based on a single leo picosatellite," International Journal of Sensor Networks, vol. 23, no. 3, pp. 143–154, 2017.

[71] Q. Li, Y. Lan, D. Lu, and J. Sun, "Research on improved s-mac energy conservation based on adaptive mechanism," in 2019 IEEE 19th International Conference on Communication Technology (ICCT). IEEE, 2019, pp. 962–966.

[72] D. Torrieri, Frequency-Hopping Systems. Cham: Springer International Publishing, 2018, pp. 155–212. [Online]. Available: https://doi.org/10.1007/978-3-319-70569-9_3

[73] D. Sarwate, "Reed-solomon codes and the design of sequences for spread-spectrum multiple-access communications," Reed-Solomon Codes and Their Applications, 1994.

[74] P. Li, C. Fan, Y. Yang, and Y. Wang, "New bounds on wide-gap frequency-hopping sequences," IEEE Communications Letters, vol. 23, no. 6, pp. 1050–1053, 2019.

[75] P. Li, C. Fan, S. Mesnager, Y. Yang, and Z. Zhou, "Constructions of optimal uniform wide-gap frequency-hopping sequences," IEEE Transactions on Information Theory, vol. 68, no. 1, pp. 692–700, 2021.

[76] Lora-net, "Sx126x driver: Driver for sx126x radio," https://github.com/Lora-net/sx126x_driver, 2025, version 2.5.0, BSD-3-Clause-Clear license.

[77] M. A. Ullah, K. Mikhaylov, and H. Alves, "Analysis and simulation of LoRaWAN LR-FHSS for direct-to-satellite scenario," IEEE Wireless Communications Letters, vol. 11, no. 3, pp. 548–552, 2021.

[78] M. Goresky and A. Klapper, Algebraic shift register sequences. Cambridge University Press, 2012.

[79] A. Lempel and H. Greenberger, "Families of sequences with optimal hamming-correlation properties," IEEE Transactions on Information Theory, vol. 20, no. 1, pp. 90–94, 1974.

[80] K. Vogelgesang, J. A. Fraire, and H. Hermanns, "Uplink transmission probability functions for LoRa-based direct-to-satellite IoT: A case study," in 2021 IEEE Global Communications Conference (GLOBECOM). IEEE, 2021, pp. 01–06.

[81] T. N. González, J. L. Salamanca, S. M. Sánchez, C. A. Meza, and S. Céspedes, "Analysis of channel models for LoRa-based direct-to-satellite IoT networks served by LEO nanosatellites," in 2021 IEEE International Conference on Communications Workshops (ICC Workshops). IEEE, 2021, pp. 1–6.

Thèse accessible à l'adresse : https://theses.insa-lyon.fr/publication/2026ISAL0011/these.pdf © [D. Maldonado Muñoz], [2026], INSA Lyon, tous droits réservés

[82] D. Maldonado, “Lr-fhss network simulation for collision analysis,” GitHub repository, 2025, accessed on March 17, 2025. [Online]. Available: https://github.com/diegomm6/lr-fhss_seq-families

[83] F. Zhang, F. Yu, X. Zheng, L. Liu, and H. Ma, “DFH: Improving the reliability of LR-FHSS via dynamic frequency hopping,” in 2023 IEEE 31st International Conference on Network Protocols (ICNP), 2023, pp. 1–12.

[84] D. Wang, A. Elzanaty, and M.-S. Alouini, “Coded Frequency Hopping for Direct-to-Satellite IoT Systems: Design and Analysis,” IEEE Internet of Things Journal, pp. 1–1, 2024.

[85] M. A. Ullah, K. Mikhaylov, and H. Alves, “Analysis and Simulation of LoRaWAN LR-FHSS for Direct-to-Satellite Scenario,” IEEE Wireless Communications Letters, vol. 11, no. 3, pp. 548–552, 2022.

[86] A. Maleki, H. H. Nguyen, E. Bedeer, and R. Barton, “Outage Probability Analysis of LR-FHSS and D2D-Aided LR-FHSS Protocols in Shadowed-Rice Fading Direct-to-Satellite IoT Networks,” IEEE Internet of Things Journal, vol. 11, no. 6, pp. 11 101–11 116, 2024.

[87] D. N. Knop, J. L. Rebelatto, and R. D. Souza, “LR-FHSS With Network-Coded Header Replication,” IEEE Transactions on Vehicular Technology, vol. 73, no. 6, pp. 9066–9070, 2024.

[88] S. Jung, S. Jeong, J. Kang, J. G. Ryu, and J. Kang, “Transceiver Design and Performance Analysis for LR-FHSS-Based Direct-to-Satellite IoT,” IEEE Communications Letters, vol. 27, no. 12, pp. 3310–3314, 2023.

[89] M. A. B. Temim, G. Ferré, and O. Seller, “An LR-FHSS Receiver for a Massive IoT Connectivity,” in 2023 IEEE 34th Annual International Symposium on Personal, Indoor and Mobile Radio Communications (PIMRC). IEEE, 2023, pp. 1–6.

[90] SEMTECH, “AN1200.22 LoRa™ Modulation Basics,” Available at https://semtech.my.salesforce.com/sfc/p/#E0000000JelG/a/2R0000001OJk/yDEcfAkD9qEz6oG3PJryoHKas3UMsMDa3TFqz1UQOkM (2023/04/17).

[91] M. A. Ullah, G. Pasolini, K. Mikhaylov, and H. Alves, “Understanding the Limits of LoRa Direct-to-Satellite: The Doppler Perspectives,” IEEE Open Journal of the Communications Society, 2023.

[92] I. Ali, N. Al-Dhahir, and J. E. Hershey, “Doppler Characterization for LEO Satellites,” IEEE transactions on communications, vol. 46, no. 3, pp. 309–313, 1998.

[93] G. Boquet, B. Martinez, F. Adelantado, J. Pages, J. A. Ruiz-de Azua, and X. Vilajosana, “Low-power satellite access time estimation for internet of things services over NTNs,” IEEE Internet of Things Journal, vol. 11, no. 2, pp. 3206–3216, 2023.

[94] R. Ortigueira, S. Montejo-Sánchez, S. Henn, J. A. Fraire, and S. Céspedes, “Satellite visibility prediction for constrained devices in direct-to-satellite iot systems,” IEEE Sensors Journal, 2024.

[95] I. S. M. Hashim and A. Al-Hourani, “Satellite visibility window estimation using doppler measurement for iot applications,” IEEE Communications Letters, vol. 27, no. 3, pp. 956–960, 2023.

[96] E. Testi and E. Paolini, “Packet collision probability of direct-to-satellite iot systems,” IEEE Internet of Things Journal, 2024.

[97] A. Maleki, H. H. Nguyen, E. Bedeer, and R. Barton, “Outage probability analysis of lr-fhss and d2d-aided lr-fhss protocols in shadowed-rice fading direct-to-satellite iot networks,” IEEE Internet of Things Journal, vol. 11, no. 6, pp. 11 101–11 116, 2023.

Thèse accessible à l'adresse : https://theses.insa-lyon.fr/publication/2026ISAL0011/these.pdf © [D. Maldonado Muñoz], [2026], INSA Lyon, tous droits réservés

[98] K. Rollmann, W. Cardoso, V. Lima, and F. Miyazawa, “Heuristic and Exact Algorithms for the 2D Knapsack Problem with Relations Between Items,” Institute of Computing, University of Campinas, Campinas, Brazil, Relat’orio T’ecnico IC-PFG-17-13, December 2017. [Online]. Available: https://www.ic.unicamp.br/~reltech/PFG/2017/PFG-17-13.pdf

[99] B. Rhodes, “Skyfield: High precision research-grade positions for planets and earth satellites generator,” Astrophysics Source Code Library, pp. ascl–1907, 2019.

Thèse accessible à l'adresse : https://theses.insa-lyon.fr/publication/2026ISAL0011/these.pdf © [D. Maldonado Muñoz], [2026], INSA Lyon, tous droits réservés

FOLIO ADMINISTRATIF

THESE DE L'INSA LYON, MEMBRE DE L'UNIVERSITE DE LYON

NOM : **MALDONADO MUÑOZ** DATE de SOUTENANCE : **25 février 2026**

Prénoms : **Diego Antonio**

TITRE : **Estimation, Scalability, Robustness, and Coordination Methods for Direct-to-Satellite IoT**

NATURE : **Doctorat** Numéro d'ordre : **2026ISAL0011**

École Doctorale : **InfoMaths**

Spécialité : **Informatique**

RÉSUMÉ :
L'Internet des objets direct vers satellite (Direct-to-Satellite Internet of Things, DtS-IoT) est apparu comme un paradigme prometteur pour connecter directement un grand nombre d'appareils terrestres à faible consommation d'énergie à des satellites en orbite terrestre basse (Low Earth Orbit, LEO). Si des avancées récentes, telles que la modulation Long Range - Frequency Hopping Spread Spectrum (LR-FHSS), ont amélioré le budget de liaison et l'efficacité spectrale par rapport à la modulation LoRa classique, les défis fondamentaux que sont l'estimation de la taille du réseau, l'évolutivité de la liaison montante et la robustesse en cas de congestion restent largement non résolus.
Cette thèse améliore la fiabilité et l'efficacité des systèmes DtS-IoT en relevant ces trois défis fondamentaux. Tout d'abord, nous introduisons de nouveaux mécanismes d'estimation de la taille du réseau pour les systèmes DtS-IoT basés sur LoRa, notamment les modèles améliorés LoRa-Optimistic Collision Information (L-OCI) et OCI tenant compte de la constellation (CL-OCI). Ces estimateurs fonctionnent dans des conditions fortement sujettes aux collisions et fournissent des informations précises sur la charge a priori du réseau, utiles à l'adaptation des mécanismes d'accès au medium (MAC). Deuxièmement, nous proposons un cadre unifié pour améliorer l'évolutivité de LR-FHSS, combinant de nouvelles perspectives sur la conception des séquences de saut de fréquence (Frequency Hopping Sequences, FHS) avec des stratégies d'allocation de démodulateurs telles que *Early-Drop* et *Early-Decode*. Nos résultats montrent des améliorations significatives du volume de données extractibles dans des conditions de forte densité d'objets connectés et de ressources limitées dans les passerelles. Troisièmement, nous concevons un récepteur LR-FHSS amélioré qui permet un décodage robuste des trames dont l'en-tête a été perdu à cause d'un effet Doppler important, en décalage et taux, et d'une forte congestion. En intégrant une reconstruction gloutonne sensible au Doppler et une logique d'alignement des fragments améliorée, le récepteur récupère les trames qui seraient autrement perdues en raison de la corruption de l'en-tête. Cela augmente le taux de réussite global du décodage sans que l'objet connecte ne dépense d'énergie supplémentaire. Quatrièmement, nous abordons la choix entre LoRa et LR-FHSS, pour les communications entre les objets et les satellites, en proposant des méthodes d'accès distribuées tirant parti de techniques légères de détermination de l'orbite des satellites et de balises périodiques. Nous démontrons que les méthodes d'accès conjointes LoRa/LR-FHSS peuvent améliorer l'efficacité énergétique tout en conservant les mêmes performances qu'une approche LR-FHSS seule.
Dans toutes nos contributions, nous combinons des modèles analytiques avec des simulations à grande échelle utilisant le simulateur FLoRaSat étendu et un simulateur FHS dédié. Les méthodologies et architectures qui en résultent fournissent des voies pratiques vers des déploiements DtS-IoT évolutifs, fiables et économes en énergie.

MOTS-CLÉS : **Direct-to-Satellite, Internet of Things, LoRa/LoRaWAN, LR-FHSS**

Laboratoires de recherche : **CITI, Inria, NII**

Directeurs de thèse : **Hervé RIVANO, Juan A. FRAIRE**

Président du Jury : **Beulot André-Luc**

Composition du Jury :

BEYLOT	**André-Luc**	Prof.	ENSEEIHT	Président
CAILLOUET	**Christelle**	Prof.	Université Côte d'Azur	Rapporteure
GUTIÉRREZ GAITÁN	**Miguel**	Prof.	UC Chile	Rapporteur
KARABULUT KURT	**Güneş**	Prof.	Polytechnique Montréal	Rapporteure
RIVANO	**Hervé**	Prof.	INSA Lyon / Inria	Directeur de thèse
FRAIRE	**Juan A.**	CR HDR	INSA Lyon / Inria	Co-directeur de thèse

Thèse accessible à l'adresse : https://theses.insa-lyon.fr/publication/2026ISAL0011/these.pdf © [D. Maldonado Muñoz], [2026], INSA Lyon, tous droits réservés